Directional Reconstruction in Liquid Scintillator Neutrino Detectors



Josephine Paton

Linacre College

University of Oxford

A thesis submitted for the degree of

Doctor of Philosophy

Trinity Term 2023

Abstract

Direction reconstruction can be used as a powerful background rejection tool in neutrino experiments, notably for the isolation of highly directional sources such as the Sun. While the high light-yield of scintillator detectors leads to precise energy resolution suitable for low energy studies, the light emission is isotropic with no directional information. However, directionality might be provided by Cherenkov light, if it could be sufficiently isolated from the overwhelming scintillation signal.

The SNO+ detector is a large multipurpose neutrino detector, housed 2 km underground at SNOLAB in Sudbury, Ontario. During commissioning, the target medium of the detector was gradually changed from ultra-pure water to liquid scintillator, creating an interface between the two materials. The concentration of the primary fluor (PPO) was gradually increased as the detector was filled. There were two stable periods of data acquisition during commissioning where the concentration of PPO was 0.6 g/L, lower than the intended target of 2.2 g/L. This lower concentration created a slower scintillation profile. As time-based separation of Cherenkov light had already been demonstrated in slow scintillators on a bench-top scale, these data sets were examined for directional information. This thesis presents the first demonstration of event-by-event direction reconstruction in a high-yield large-scale liquid scintillator detector using data from these periods, with a significance of $> 5.7\sigma$.

Future prospects of directionality in scintillator will benefit from multiple Cherenkov separation techniques. However, simulated studies of 0.6 g/L PPO in the solvent LAB show that significant improvements can be made only by using modern photon-detection capabilities, without reducing the detected light yield. By prioritising improvements to photon-sampling, the next generation of liquid scintillator neutrino detectors may be able to effectively reject directional backgrounds at low energies, improving the sensitivities of studies such as reactor anti-neutrinos, CNO solar neutrinos, and the search for neutrinoless double beta decay.

Acknowledgements

It would not have been possible for me to complete this work without the support of countless people along the way. So here are a series of thank yous to some of the people who kept me going.

To Steve Biller, for his wisdom and guidance across the last six years. His enthusiasm for the field was what brought me to the topic of neutrino experiments, and his support and encouragement were invaluable in overcoming the hurdles this thesis went through. I can't say that every moment was fun, but you were always able to remind me how to enjoy it again. Not only did you show me how to be a good physicist, but you helped me gain the confidence to call myself one.

To Jeff Tseng and Armin Reichold for their advice in all manner of topics, both relating to physics and just in general life. Whether in a group meeting or over coffee, your fresh pairs of eyes could often see through to whatever wood I was missing for the trees.

To the support staff in the particle physics department for more support than I could possibly write out here. An extra special acknowledgement must go to Kim and Sue, without whom I'm sure I would have drowned under forms years ago. Also to IT Support, I thank you and I apologise for the crimes I have committed against the queue system.

To the SNO+ office and the numerous students I have shared it with; Esther, Tereza, Iwan, Josh, Daniel, Rafael, Cal, Gulliver and Jasmine. You have all made the office a delightful place to come to (almost) every day. Special thanks have to go to Iwan for our lockdown walks (and rants) that played a large part in maintaining some semblance of my sanity in those isolated times, and Daniel for being a great write-up-buddy through long hours in the library, cut short when inevitably at least one of us had forgotten our laptop charger. Another thank you to the wonderful post-docs who supported me through different points in my PhD. From piecing together equipment in the aquarium with Ed, to Will helping me get RAT running for the millionth time. From Ana Sofia proofreading every page of this thesis, to Ben (a post-doc in spirit) letting me sit in your office and rant at midnight when I should have been writing. My deepest gratitudes go to you all.

To those in Sudbury who made those short two months forever memorable. Lorna and Charlie for being excellent flat mates. Cindy, Ben, Matt, Steph, Rachel, and all the SNOLAB crew for providing more than enough social life to make the winter months truly enjoyable. Through breakfasts at Eddie's, karaoke at

Little Montreal, and visits to the best Sudbury has to offer (by which I mean, Science North on Valentines Day), I've made some friends for life and my only regret is that I wasn't able to stay longer.

To those in Oxford, a town I have now called home for almost nine years. To Brigit for being my lockdown buddy, flatmate, and most importantly friend. Because of you I know way more about birds than I ever thought I would, and I hope you enjoyed learning about neutrinos in exchange. Your company and friendship has made the last few years so much more fun. To Claudine who always knew the exact right moment to suggest a vent over a glass of wine, whether that was about our work, our lives, or about the general lack of common sense in the world. To all the wonderful people of Linacre College who made it a real family. To the various members of the DisCam committee, with whom I found true solidarity and passion for making this University a better place for disabled students. To all the weird and wonderful members of the RPGSoc, who provided me with endless worlds to escape into when I needed a break from the realities of research and thesis writing. I have loved this University and this town for so long, and loved so many people in it, and I am going to miss it dearly.

Finally, to my family: my mum Sylvia, my dad Ken, and my brother James. Your unwavering and enthusiastic belief in me has always just been a phone call away. Whether it's driving a van to Oxford to help me move flat, helping me set up an ergonomic office space during a lockdown at home, or just letting me talk through whatever it is my brain is stuck on that day. I have been incredibly lucky to have the support and love you have given me, and I hope to live up to the pride you have always had in me.

Thank you all for everything. I couldn't have done it without you.

"Don't Panic."

- The Hitchhiker's Guide to the Galaxy, Douglas Adams

To any future SNO+ student who reads this.
I hope it contains the answers you're looking for.
If not, I wish you luck on docDB.

Statement of Authorship

This statement provides an outline of the author's contributions to and ownership of the work included in this thesis.

Chapter 1 provides a background understanding of neutrino physics, solar neutrino production, and neutrino detection using Cherenkov and scintillator detectors. This information provides a necessary theoretical basis for the work presented in this thesis. This chapter is comprised of information taken from publications and text books.

Chapter 2 includes work presented in the publication *Slow fluors for effective separation of Cherenkov light in liquid scintillators*. The author of this thesis is a co-author of the paper, along with Steven Biller and Edward Leming. The work included in this thesis involves the measurement of timing parameters of the slow fluors, and was conducted by the author collaboratively with Edward Leming. The author's contributions included the creation of the experimental equipment, acquisition of the data, and development of the analysis methods and computational framework. Additional information from the paper, including measurements of emission and absorption spectra, is referenced to draw conclusions about the feasibility of using the studied slow fluors in large scale neutrino detectors.

Chapter 3 provides a description of the SNO+ experiment. This information is based on publications, technical reports and internal documents, and is necessary to understand the analysis conducted in this thesis. The author contributed to the scintillator loading of the detector, as well as the maintenance of data flow for both MC production and data processing.

Chapter 4 contains the description of a method to reconstruct direction in scintillators, followed by the use of this method on data from the SNO+ experiment. This work was conducted by the author, including the development of the method, the testing of performance, the data selection and the final analysis. Support was supplied in data selection by members of the SNO+ collaboration, with inspiration taken from Ana Sofia Inacio's thesis in selecting high energy ^{8}B events.

Chapter 5 contains suggested methods for combining position and direction reconstruction. This work was led by the author, and was completed with support from Will Parker who contributed to testing the simultaneous direction-position reconstruction algorithm. This chapter also includes projections for direction reconstruction in a future detector with modern photon detection capabilities. This work was conducted by the author.

Contents

1 Introduction **1**

1.1 Neutrino Physics 4

1.1.1 Neutrino Oscillations 5

1.1.2 Neutrino Mass 7

1.1.3 Neutrinoless Double Beta Decay 9

1.1.4 Neutrino-Electron Elastic Scattering 12

1.2 Solar Neutrinos 15

1.2.1 The Proton-Proton Chain 16

1.2.2 The CNO Cycle 17

1.2.3 Solar Neutrino Energy Spectrum 18

1.3 Photon-Based Neutrino Detection 19

1.3.1 Cherenkov Detectors 20

1.3.2 Scintillator Detectors 23

1.3.3 Hybrid Detectors 27

1.3.3.1 Correlated and Integrated Directionality 27

1.3.3.2 Wavelength Separation and Dichroicons 29

1.3.3.3 Scintillation Suppression and Water-based Liquid Scintillator 32

1.3.3.4 Time Separation 34

2 Slow Fluors for Cherenkov Separation **36**

2.1 Method of Time Profile Measurement 37

2.1.1 Time Resolution Measurement 41

2.2 Analysis of Scintillator Time Profiles 42

2.3 Candidate Fluors 43

2.4 Results 46

2.5 Conclusions 52

3 The SNO+ Experiment **54**

3.1 The SNO+ Detector 55

3.1.1 Photomultiplier tubes 57

3.1.2 Data Readout and Acquisition 59

3.2 Experimental Phases of SNO+ 60

3.2.1 The Water Phase . . . 60
3.2.2 The Partial-Fill Phase . . . 61
3.2.3 The Full-Fill 0.6 g/L Phase . . . 63
3.2.4 The Scintillator Phase . . . 63
3.2.5 The Tellurium Phase . . . 64
3.3 Software and Simulation . . . 65
3.4 Event Reconstruction in SNO+ . . . 66
3.4.1 Position-Time Vertex . . . 66
3.4.2 Energy and NHit . . . 72

4 Reconstruction of Direction in Liquid Scintillator 75
4.1 Directionality Methods . . . 76
4.1.1 Probability Density Function . . . 77
4.1.2 Reconstruction of Direction . . . 84
4.2 Effects Limiting Direction Reconstruction . . . 87
4.2.1 Effect of Position Reconstruction . . . 87
4.2.2 Effect of Electron Multiple Scattering . . . 93
4.2.3 Summary of Limiting Effects . . . 97
4.3 Dataset . . . 98
4.3.1 Event Selection . . . 100
4.4 Application to Data, Analysis, and Results . . . 102
4.4.1 Neutrino-Electron Scattering . . . 102
4.4.2 Results in Data . . . 105
4.4.3 Analysis . . . 107
4.5 Conclusions . . . 109

5 Future Directions 111
5.1 Combined Direction-Position Reconstruction . . . 112
5.1.1 Simultaneous Direction-Position Reconstruction . . . 112
5.1.2 Flat Drive Correction . . . 124
5.2 Directionality using Improved Photodetection . . . 127
5.3 Comparison to Slow Scintillators . . . 132
5.4 Conclusions . . . 136

6 Conclusions 139

A Glossary 141

List of Figures

1.1 Diagram of the normal and inverted mass hierarchies. 8
1.2 Diagram of mass parabolas of isobaric nuclei, demonstrating the existence of double beta decay 10
1.3 Feynman diagrams of $2\nu\beta\beta$ and $0\nu\beta\beta$. 11
1.4 Energy signature of $0\nu\beta\beta$ as compared to the $2\nu\beta\beta$ spectrum. . . . 12
1.5 Feyman diagrams for $\nu - e$ ES 13
1.6 Energy spectrum of solar neutrinos. 19
1.7 Diagrams of Cherenkov radiation emission 21
1.8 Diagram of Cherenkov angle 21
1.9 Diagrams of the electron orbitals in a benzene ring. 24
1.10 Definition of angular information used in CID in the Borexino experiment. 28
1.11 Distribution of the first detected photons in α for Phase 1 of the Borexino experiment. 28
1.12 Comparison of scintillation and Cherenkov emission spectra 30
1.13 Schematic of a prototype dichroicon 31
1.14 Structure of a micelle 33

2.1 Diagrams of experimental set up for scintillator timing profile measurements 38
2.2 Photograph of experimental set up for scintillator timing profile measurements 39
2.3 Impulse Response Function 41
2.4 Time profile of the primary fluor acenaphthene 48
2.5 Time profiles of the primary fluor pyrene 49
2.6 Time profile of the primary fluor DPA 50
2.7 Time profile of the secondary fluor DPH 50

3.1 Drawing of the SNO+ detector. 55
3.2 Schematics of SNO+ PMT and concentrator. 57
3.3 R1408 PMT transit time distribution. 58
3.4 Efficiency of the R1408 PMT as a function of wavelength. 59

3.5 Photograph of the SNO+ detector demonstrating the LS-UPW interface. 61
3.6 Comparison of the tuned time profiles of 0.6 g/L and 2.2 g/L PPO scintillator cocktails. 64
3.7 Performance of position reconstruction in SNO+ 69
3.8 Performance of time reconstruction in SNO+. 71
3.9 NHit as a function of energy 72
3.10 NHit as a function of radius 74

4.1 Diagram of the photon angle θ_γ 77
4.2 Photon angle distributions for Cherenkov-only and Cherenkov-Scintillator scenarios 78
4.3 Comparison of t_{res} distributions for scintillation and Cherenkov light. 79
4.4 Time residual plots compared for events at the centre of the detector and throughout the detector volume. 80
4.5 2D PDF in t_{res} and $\cos(\theta_\gamma)$ using the MC truth position-time vertex. 82
4.6 2D PDF in t_{res} and $\cos(\theta_\gamma)$ using the reconstructed position-time vertex. 83
4.7 A comparison of photon hits with a calculated $t_{res} < 2$ ns in $\cos(\theta_\gamma)$ for the true and fitted vertices. 83
4.8 Results of direction reconstruction in simulation for different electron energies. 85
4.9 Diagram of drive 87
4.10 Drive of 6 MeV electrons 88
4.11 Drive as a function of energy and radius. 89
4.12 Comparison of drive with and without Cherenkov light 90
4.13 Diagram explaining how drive is caused by Cherenkov light 90
4.14 Effect of position mis-reconstruction on the reconstruction of direction 92
4.15 Diagram of θ_{msc}, the angle between the initial and average direction of travel of an electron 93
4.16 Distributions of $\cos(\theta_{msc})$ for electrons of different energies 94
4.17 Effect of electron multiple scattering on the effectiveness of reconstruction of direction 96
4.18 Comparison of direction reconstruction considering the effects of multiple scattering of electrons and biases in position reconstruction 98
4.19 Diagram of the relationship between the angles α, $\theta_{\nu\text{-}e}$ and θ_{sun} . . 102

4.20 Distribution of $\theta_{\nu\text{-}e}$ for simulated ^{8}B solar neutrinos. 104
4.21 $\theta_{\nu\text{-}e}$ distribution of simulate events that pass analysis cuts. 105
4.22 Results of direction reconstruction in SNO+ data. 106
4.23 Distribution of $-2\log\left(\frac{\mathcal{L}_0}{\mathcal{L}_1}\right)$ for randomly generated samples of 37 events. 108

5.1 Time projection of the PDF used for simultaneous direction-position reconstruction. 113
5.2 Visualisation of the adaptive grid algorithm 114
5.3 Results of the adaptive grid direction-position reconstruction for 6 MeV electrons, compared to three test cases. 118
5.4 Drive of 6 MeV electrons reconstructed using adaptive grid direction-position reconstruction. 119
5.5 LLH space of two events in drive and $\cos(\alpha)$ 121
5.6 Results of the adaptive grid direction-position reconstruction, separating events with a drive cut at 200 mm. 122
5.7 Results of simultaneous direction-position reconstruction on 10 MeV electrons. 123
5.8 Results of flat drive correction on drive and x-axis reconstruction. 126
5.9 Comparison of the timing and efficiency of the R5912 and R1408 PMTs. 127
5.10 Performance of position reconstruction using the R5912. 128
5.11 Drive as a function of energy using the R5912. 129
5.12 Comparison of direction reconstruction at different electron energies using the R5912 and R1408 PMTs. 130
5.13 Results of direction reconstruction for 1 MeV to 3 MeV electrons using the R5912. 131
5.14 Percentage of events with $\cos(\alpha) > 0.8$ for different electron energies using the both the R5912 and the R1408 PMTS. 131
5.15 Comparison of direction reconstruction in PPO to Acenaphthene with the addition of bis-MSB. 134
5.16 Comparison of direction reconstruction in PPO to Acenaphthene without bis-MSB. 135

List of Tables

1.1 Values of g_1 and g_2 for different neutrino flavours. 14

2.1 Parameters used in response function fitting. 43
2.2 Summary of scintillator cocktails selected for timing characterisation. 45
2.3 Best fit time constants for all candidate scintillator cocktails. 51
2.4 Best fit scaling constants for all candidate scintillator cocktails. . . 51

3.1 Tuned timing parameters of the SNO+ 0.6 g/L LABPPO scintillator cocktail. 62
3.2 Tuned timing parameters of the SNO+ 2.2 g/L LABPPO scintillator cocktail. 64

4.1 Effectiveness of direction reconstruction at different electron energies. 86
4.2 Magnitude of electron multiple scattering in LS at different energies 95
4.3 Effectiveness of direction reconstruction considering the effects of multiple scattering of electrons and biases in position reconstruction 97

5.1 Parameters used in the adaptive grid fitting optimisation algorithm. 115
5.2 Summary of test cases for the comparison of direction-position reconstruction. 117
5.3 Results of the adaptive grid direction-position reconstruction for 6 MeV electrons, compared to three test cases. 118
5.4 Results of the adaptive grid direction-position reconstruction for 10 MeV electrons, compared to three test cases. 124
5.5 Results of flat drive correction on mean drive and x-axis resolution. 125
5.6 Effectiveness of direction reconstruction at different electron energies using both the R1408 and the R5912 PMTs. 132
5.7 Summary of the simulated configurations of slow scintillator studies. 133
5.8 Detected light yield for slow scintillators compared to PPO. 136

Chapter 1

Introduction

"There is no point in using the word 'impossible' to describe something that has clearly happened."

- Dirk Gently's Holistic Detective Agency, Douglas Adams

After Wolfgang Pauli first posited the existence of the neutrino in 1930 as a solution to the β-decay spectrum [1], he supposedly stated "I have done a terrible thing. I have postulated a particle that cannot be detected." [2]. 1956 would see him proved both right and wrong as Cowan and Reines detected the antineutrinos emitted from beta decays in a nuclear reactor through observations of inverse beta decay in a liquid scintillator detector [3, 4]. Over the decades not only did neutrino detection become commonplace, new experimental techniques were rapidly developed. The first use of a neutrino beam at the Brookhaven Alternating Gradient Synchrotron led to the discovery of the muon neutrino [5]. The Homestake detector used neutrino capture conversion of $\nu_e + {}^{37}\mathrm{Cl} \rightarrow {}^{37}\mathrm{Ar}^{+} + e^{-}$ to detect solar neutrinos [6, 7]. This measurement of the solar neutrino flux disagreed with leading solar models, leading to the Solar Neutrino Problem (SNP) [8]. This was later solved by utilising a combination of charged current, neutral current and elastic scattering of neutrinos to demonstrate the existence of neutrino oscillations [9–11], proving the existence of neutrino mass. New detector technologies paved the way for new discoveries, allowing us to learn more about one of the most enigmatic fundamental particles.

Today there are many types of neutrino detector, each utilising different

strengths to continue pushing the frontier of Beyond the Standard Model (BSM) physics. Many solar neutrino detectors use Cherenkov ring imaging, mainly in water, in order to use the incoming direction of a neutrino for background reduction. Large scintillator detectors are utilising the benefits of the improved energy reconstruction that can be achieved with higher light yields to do precision low energy studies, including the search for neutrinoless double beta decay ($0\nu\beta\beta$). However, while directional Cherenkov rings can be present in any medium, in scintillator the Cherenkov photons are overwhelmed by the dominant high-yield scintillation photons. This means that directional information is hard to extract, as scintillation itself is emitted isotropically. If the Cherenkov ring could be sufficiently isolated, there would be the potential to combined the benefits of precise energy reconstruction with directional background rejection.

The goal of directionality in scintillator has been explored in the community for many years and remains prominent in discussions of the future of the field [12]. Directional reconstruction using time separated Cherenkov signals has been investigated in simulations of large scale experiments [13, 14]. Studies to separate Cherenkov photons have been done on a table top scale in a variety of scintillators using cosmic muons [15–18] and electrons [19–21], implementing a range of technologies. Statistical separation of directional sub-MeV solar neutrino events has been shown by the Borexino experiment [22]. LSND [23] and MiniBooNE [24] have shown directional reconstruction at high energy scales (10s MeV - 1 GeV) using low-yield scintillator to allow for a dominant Cherenkov signal. Future "hybrid" experiments have been planned that use water-based liquid scintillator (WbLS), where liquid scintillator is diluted in water to reduce the yield of photons and allow a more dominant Cherenkov signal, in combination with wavelength separation of Cherenkov and scintillation photons [25, 26].

So far, no large-scale high-yield scintillator experiment has so far been able to reconstruct direction on an event by event basis. In this thesis, a method for such

reconstruction will be presented which uses the timing separation between the Cherenkov and scintillation signals. Event-by-event directional reconstruction will be demonstrated in data using solar neutrinos at the MeV energy scale in the SNO+ detector.

Neutrino properties and interactions are described in Section 1.1, providing motivation for the methodologies contained within this thesis. Section 1.2 describes the production of neutrinos by nuclear interactions in the Sun. In Section 1.3 the physical processes behind scintillator and Cherenkov detectors are outlines, explaining the differences in timing that can be used to extract directional information from a scintillator detector. Additionally, potential methods of Cherenkov/scintillation hybridisation are discussed.

In order to increase the time separation, slower scintillators can be used. Several slow fluors are explored in Chapter 2. An adapted single photon method for measuring the timing parameters of a scintillator is described, and the emission time profiles of liquid scintillator containing slow primary and secondary fluors are presented.

The SNO+ experiment is described in Chapter 3. The geometry of the detector and the data acquisition systems are explained, followed by a timeline of experimental phases from the past, present and future. The simulation and reconstruction software of the detector are also described.

The methods and results of directional reconstruction in the SNO+ experiment are detailed in Chapter 4. A 2D probability density function is introduced, containing both time and topological information for individual detected photons in a given physics event. This is then used in a maximum likelihood reconstruction algorithm to find the most probable direction of electron travel through the scintillator. The effectiveness of this method is demonstrated in simulations and major limiting factors are discussed. The method then applied to high energy data of ^{8}B solar neutrino events.

The future of directional reconstruction in scintillator is discussed in Chapter 5. A method for combined direction-position reconstruction is explored. The effectiveness in simulation is presented with explanations of the limits of such methods in the SNO+ detector. The use of directional information to reduce biases in position reconstruction is demonstrated. Additionally, the possibilities of direction reconstruction in future detectors is investigated by simulating a SNO+-like detector with modern photon detection capabilities. Conclusions of this thesis can then be found in Chapter 6.

1.1 Neutrino Physics

Neutrinos are neutral spin-$\frac{1}{2}$ leptons. There are three generations, named after the corresponding charged-lepton flavours: ν_e, ν_μ and ν_τ. Neutrinos only interact through the weak force and gravity. They are known to violate charge-symmetry (as there is no detectable right-handed neutrino) and parity-symmetry (as there is no detectable left-handed antineutrino). Neutrinos are unique within the Standard Model (SM) for many reasons.

Neutrinos offer one of the most prominent windows to BSM physics available to physicists today. Multiple open questions in neutrino physics have implications across the entirety of physics, and so their properties and interactions have attracted decades of study. However, due to their weak interactions they remain difficult to detect, requiring significant investment in the development and commissioning of large neutrino detectors.

This section will give an overview of the properties of the neutrino, emphasising some of the open questions in neutrino physics.

1.1.1 Neutrino Oscillations

Neutrino oscillations were proposed as a solution to the SNP [27–29], after the measured solar neutrino flux was found to be significantly lower than that predicted by leading solar models (discussed further in Section 1.2). The theory of neutrino oscillation proposed that the expected electron neutrinos may have oscillated into a different type of neutrino, causing discrepancies between the measured and predicted flux. The discovery of neutrino oscillations by SNO [9] and SuperK [11] opened a wide ranging area of BSM physics for study.

Neutrino oscillations are caused by the fact that the three flavour eigenstates ($|\nu_{e,\mu,\tau}\rangle$) are a superposition of the three mass eigenstates ($|\nu_{1,2,3}\rangle$). While the flavour eigenstate of a given neutrino dictates the interaction paths available to the neutrino, the mass eigenstate dictates how the neutrino will propagate through space. The transformation between the flavour and mass eigenstates occurs using the Pontecorvo–Maki–Nakagawa–Sakata (PMNS) matrix, U, as in Equation 1.1.1.

$$|\nu_x\rangle = \sum_{\alpha} U_{\alpha,x}|\nu_\alpha\rangle \tag{1.1.1}$$

where $\alpha = e, \mu, \tau$ and $x = 1, 2, 3$. U is used to describe the three-flavour neutrino oscillation probabilities. As will be discussed further in Subsection 1.1.2, neutrinos have the possibility of being Majorana particles. U can be expressed as the product of two matrices, $U = U^D U^M$, where U^D is the Dirac matrix and U^M is the Majorana matrix. If neutrinos are in fact Majorana particles, U^M has the form

$$U^M = \begin{pmatrix} 1 & 0 & 0 \\ 0 & e^{i\phi_1} & 0 \\ 0 & 0 & e^{i\phi_2} \end{pmatrix} \tag{1.1.2}$$

where $\phi_{1,2}$ are the Majorana phases. If neutrino are not Majorana particles, $\phi_{1,2} = 0$ and $U^M = I$. U^D can be expressed as a combination of three two-flavour

oscillation matrices, as in Equation 1.1.3.

$$\begin{aligned} U^D &= \begin{pmatrix} 1 & 0 & 0 \\ 0 & c_{23} & s_{23} \\ 0 & -s_{23} & c_{23} \end{pmatrix} \begin{pmatrix} c_{13} & 0 & s_{13}e^{-i\delta} \\ 0 & 1 & 0 \\ -s_{13}e^{-i\delta} & 0 & c_{13} \end{pmatrix} \begin{pmatrix} c_{12} & s_{12} & 0 \\ -s_{12} & c_{12} & 0 \\ 0 & 0 & 1 \end{pmatrix} \\ &= \begin{pmatrix} U_{e1} & U_{e2} & U_{e3} \\ U_{\mu 1} & U_{\mu 2} & U_{\mu 3} \\ U_{\tau 1} & U_{\tau 2} & U_{\tau 3} \end{pmatrix} \end{aligned} \tag{1.1.3}$$

where $c_{xy} = \cos(\theta_{xy})$, $s_{xy} = \sin(\theta_{xy})$, θ_{xy} is the mixing angle between mass states x and y, and δ is the CP violation term. The probability of observing a neutrino oscillation from flavour α to flavour β after travelling a distance L through vacuum is given by Equation 1.1.4 [30].

$$P(\nu_\alpha \to \nu_\beta) = \sum_{k,j} U_{\alpha k} U^*_{\beta k} U^*_{\alpha j} U_{\beta j} \exp\left(-i\frac{\Delta m^2_{kj} L}{2E}\right) \tag{1.1.4}$$

where $\Delta m^2_{kj} = m^2_k - m^2_j$ is the difference in mass squared between the mass eigenstates k and j, and E is the energy of the neutrino. Oscillation experiments continue to improve precisions of the measurements of the mixing parameters present in the PMNS matrix, as well as the Δm^2 between the neutrinos.

Neutrino oscillation in vacuum requires no interaction with matter, and is an inherent property of neutrinos themselves. However, matter can affect the detection probability of neutrino flavours through the Mikheyev–Smirnov–Wolfenstein (MSW) effect. In matter, neutrinos can interact with particles via the weak force. While all three neutrino flavours are able to interact with electrons and nucleons via the Neutral Current (NC), only ν_e are able to interact with electrons via the Charged Current (CC) (further explanation of neutrino interactions will be described in Subsection 1.1.4). Because of this, propagating through matter changes the effective potential for ν_e differently to the other flavour states, cre-

ating a potential that is dependent on electron density. This leads to an altered mixing angle, and also creates sensitivity to the sign of Δm^2, which is not present in vacuum oscillations. This effect becomes prominent in solar neutrino measurements, where the neutrinos must traverse the dense electron cloud in the Sun before travelling through the vacuum of space.

A notable implication of neutrino oscillations is the existence of a neutrino mass. In the SM, the neutrino is massless and does not couple to the Higgs Boson. However, neutrino oscillations require a non-zero value for Δm^2, meaning neutrinos must have mass. This opens the question of how that mass is possible.

1.1.2 Neutrino Mass

While the discovery of neutrino oscillations provided proof for neutrino masses, there are still significant open questions on the topic. While the sign of Δm^2_{12} is known from solar neutrino measurements [10], only the absolute values are known for the other mass squared differences. This leads to the possibility for two different hierarchies of mass ordering, known as the normal and inverted hierarchy, demonstrated in Figure 1.1.

Additionally, while the Δm^2 of neutrinos are measured through oscillation experiments, this does not provide a measure of the absolute masses of the neutrinos. Direct measurements of the mass of the neutrino are still under investigation, such as the KATRIN experiment [32], which investigates the effect neutrino mass has on beta decay kinematics.

However, one of the biggest questions raised by the existence of the neutrino mass is the mechanism by which that mass could be possible. In the SM, neutrinos are not able to couple to the Higgs boson. This is because the general mass term of the SM Langrangian has the form shown in Equation 1.1.5 [33].

$$\mathcal{L}_D = m_D(\bar{\psi}_L \psi_R + \bar{\psi}_R \psi_L) \tag{1.1.5}$$

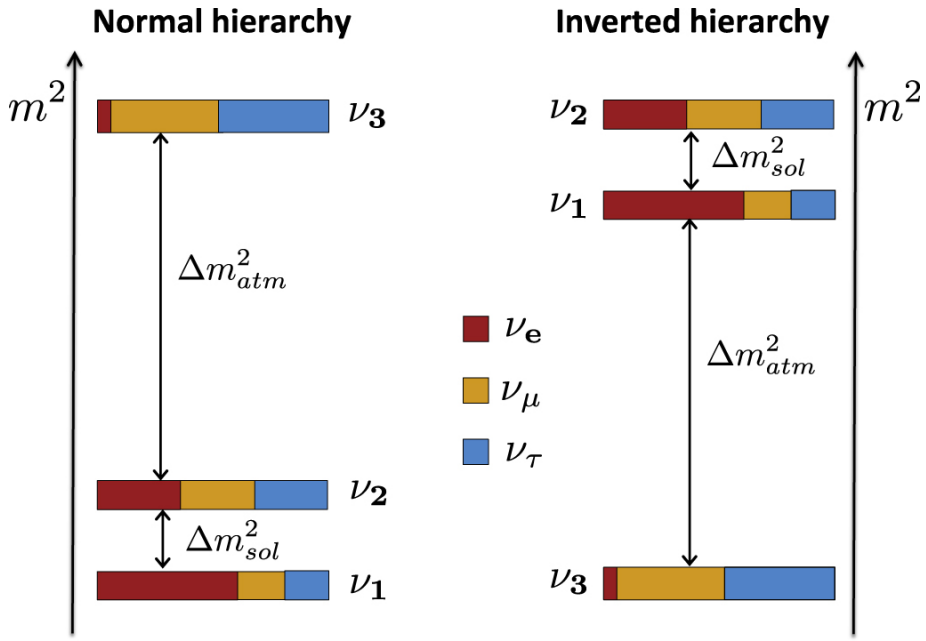


Figure 1.1: A diagram comparing the normal and inverted mass hierarchies for neutrinos. Each mass eigenstate is colour coded using approximate proportions for each flavour state. The Δm^2 are labelled as "atmospheric" and "solar", indicating the experimental regime in which they are typically measured. Figure taken from [31]

Where m_D is the Dirac mass of the particle (proportional to the coupling to the Higgs), ψ is a particle field, and L/R are the left/right chiral components. This Lagrangian requires both the left and right handed components of a particle to exist for it to have mass. However, in the SM a neutrino can only be left-handed, as only left-handed neutrinos are able to couple to the weak force. This means in order to have a neutrino with a Dirac mass, a sterile right-handed neutrino must be added that does not couple to the weak force but only interacts through gravity. While this solution is possible, it does not offer an explanation for the large difference in scale between neutrino masses and the other SM particles.

However, this is not the only option for the mass mechanism of neutrinos. Fermions in the SM are assumed to be Dirac fermions — they have a distinct particle and anti-particle. For charged fermions, this must be the case as the anti-particle has the opposite charge, so is fundamentally different to the particle. However, neutrinos are neutral, and therefore there is the possibility that there

is no difference between the neutrino and the anti-neutrino.

In 1937, Ettore Majorana presented a theoretical framework for a different type of particle [34]. The Majorana particle is defined by Equation 1.1.6 [35].

$$\psi^C = C\bar{\psi}^T = \psi \qquad\qquad C = i\gamma_0\gamma_2 \tag{1.1.6}$$

Where ψ^C is the charge conjugate of ψ, C is the charge conjugation matrix, and γ_0, γ_2 are Dirac matrices. This condition can only apply to neutral particles. It can be shown that under the Majorana condition, $\psi_R = \psi_L^C$ [36], and a new Majorana mass term can be formed as in Equation 1.1.7 [35].

$$\mathcal{L}_M^L = \frac{m}{2}(\bar{\psi}_L^C\psi_L + \bar{\psi}_L\psi_L^C) \tag{1.1.7}$$

Where m is the mass of the left-handed neutrino. If neutrinos are Majorana particles, this would allow for neutrinos masses without the introduction of sterile right-handed neutrinos, while also providing an explanation for the different mass scales of neutrinos and the other SM particles.

So far, no evidence has been found to either prove or disprove neutrinos as Majorana particles. However, many current and future experiments are searching for a phenomena that could confirm the Majorana nature of neutrinos: neutrinoless double beta decay.

1.1.3 Neutrinoless Double Beta Decay

Beta decay is a well understood process, where a neutron within a nucleus decays into a proton, emitting an electron and an anti-neutrino. Double beta decay is the process of a nucleus undergoing two simultaneous beta decays [37], as in Equation 1.1.8.

$$(Z, A) \rightarrow (Z + 2, A) + 2e^- + 2\bar{\nu}_e \tag{1.1.8}$$

The reason this occurs can be explained using the mass parabolas of isobaric nuclei (nuclei with a constant atomic number) as shown in Figure 1.2.

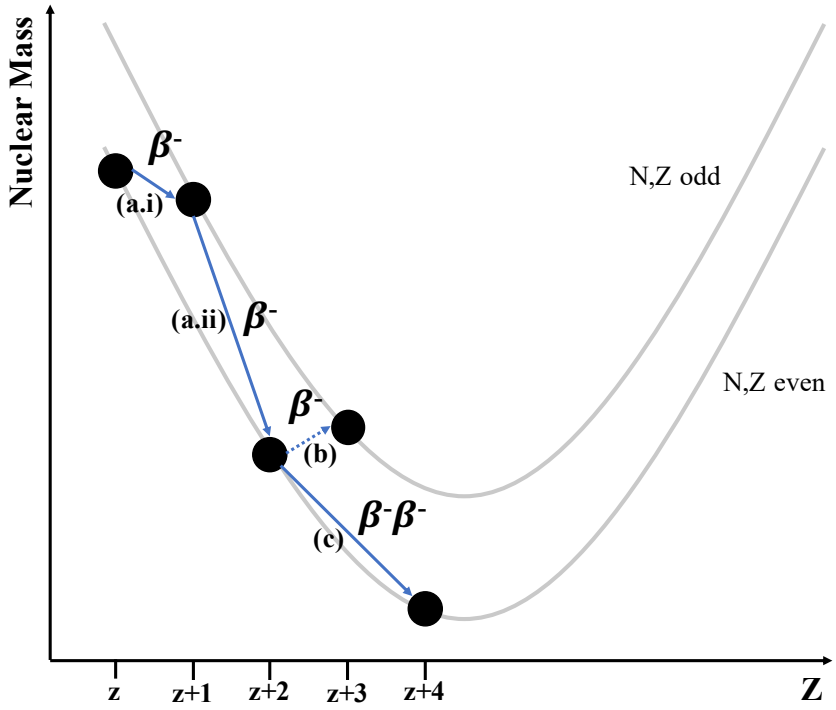
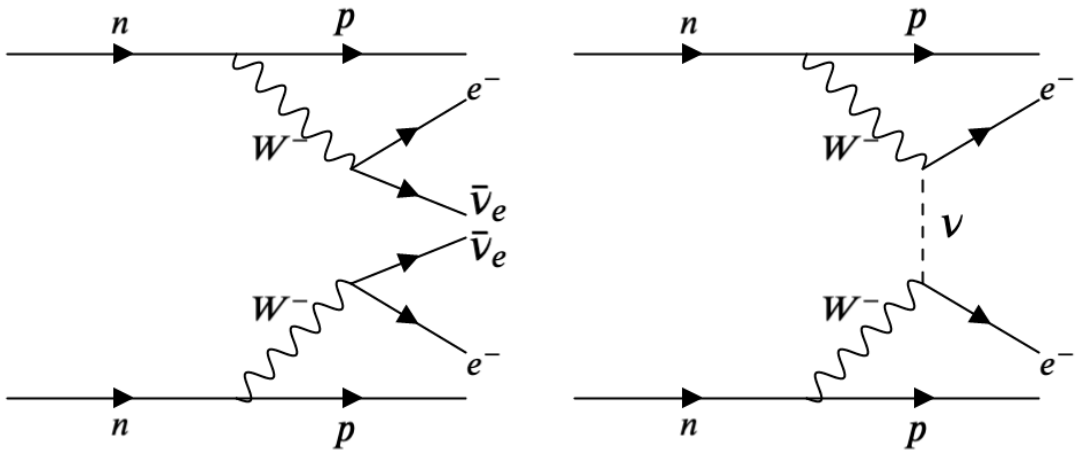


Figure 1.2: The mass parabolas of isobaric nuclei with an even atomic number. The pairing term in the binding energy splits the even-even nuclei from the odd-odd nuclei. β^- decay can occur between the parabola, changing Z by 1, as in (a.i) and (a.ii). In (b), the daughter nucleus would have a larger mass, so the β^- decay is forbidden. However, the nucleus can still decay via $\beta^-\beta^-$, changing Z by 2, as in (c). Processes that reduce Z are also possible through the emission of β^+, though not shown on this diagram.

When a nucleus has an even atomic number, it can have N and Z be both even or odd. It is energetically favourable for like nucleons to pair, leading to an additional term in the binding energy that reduces the mass of even-even nuclei [38], leading to two split mass parabolas. A β^- decay can occur between the parabolas as shown in (a.i) and (a.ii) in Figure 1.2, where the daughter nucleus has a smaller mass than the parent. The β^- decay in (b) would create a daughter nucleus with a larger mass than that of the parent, meaning this process is forbidden. However, the parent nucleus is not the most stable state, and can instead decay through two simultaneous β^- decays, as shown in (c). Double beta decay

has been experimentally observed in multiple isotopes [39].

If neutrinos are Majorana particles, there is another possibility for double beta decay. Rather than producing two antineutrinos, it is possible that the anti-neutrinos could annihilate, as they are their own anti-particle [40]. This process is known as neutrinoless double beta decay ($0\nu\beta\beta$). The Feynman diagrams of both two neutrino double beta decay ($2\nu\beta\beta$) and $0\nu\beta\beta$ are in Figure 1.3.



(a) $2\nu\beta\beta$ (b) $0\nu\beta\beta$

Figure 1.3: Feynman diagrams of double beta decay. In (a), two antineutrinos are emitted as expected. In (b), the antineutrinos annihilate due to their Majorana nature.

$0\nu\beta\beta$ has not yet been observed. Many experiments, both current and planned, have the search for $0\nu\beta\beta$ as a primary physics goal [41]. The detection of $0\nu\beta\beta$ would prove that neutrinos are Majorana particles, and would demonstrate a lepton number violating process. This discovery would have wide ranging implications throughout particle physics.

The main physics goal of SNO+ is to observe $0\nu\beta\beta$. This search will look for the distinct energy signal of $0\nu\beta\beta$ as a delta peak at the Q-value of the $2\nu\beta\beta$, as seen in Figure 1.4.

The separation between the $0\nu\beta\beta$ peak and the $2\nu\beta\beta$ spectrum end point is due to the mass of the neutrinos, which reduces the available energy given to

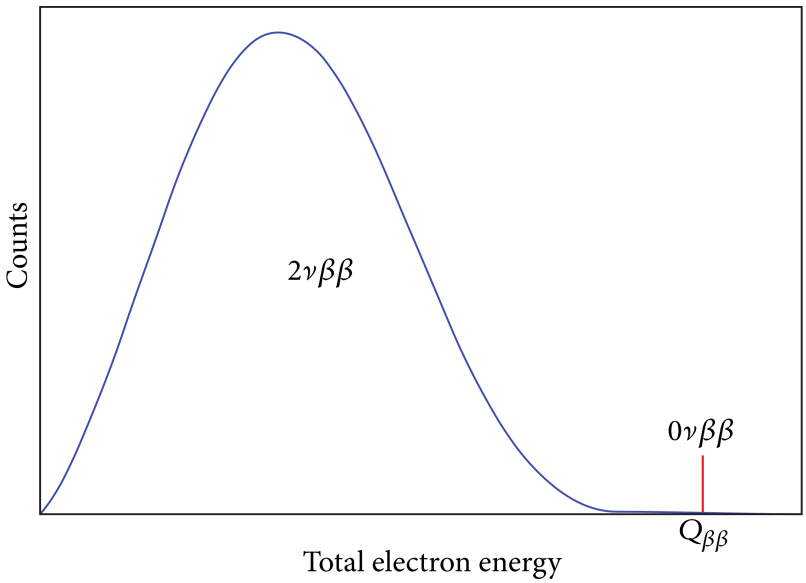


Figure 1.4: Energy signature of $0\nu\beta\beta$ as compared to the $2\nu\beta\beta$ spectrum. The spectrum is given as a function of the total energy of the two emitted electrons. There is a separation in energy between the end of the $2\nu\beta\beta$ spectrum and the $0\nu\beta\beta$ peak, corresponding to the neutrino mass. Figure taken from [42].

the electrons in $2\nu\beta\beta$. This means that the detection of $0\nu\beta\beta$ could also provide a method of measuring the Majorana mass of the neutrino. However, detector resolution effects smear both the signal and the background, reducing the separation. Because of this, there is a high importance placed on precise energy reconstruction in $0\nu\beta\beta$ experiments for the ability to resolve the peak.

1.1.4 Neutrino-Electron Elastic Scattering

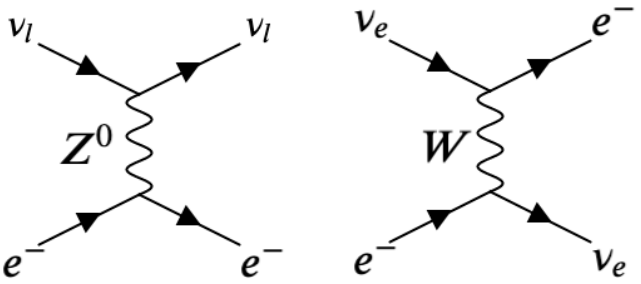
Neutrinos are detected through their interactions with matter. Because of this, neutrino interactions need to be well understood for any investigation of neutrino properties to be successful. The type of neutrino interaction used in each experiment is determined by the energy scale of the neutrinos being detected. Neutrinos can scatter off nuclei, nucleons, or even partons at a high enough energy. In a detector like SNO+, the incoming neutrinos are usually not of a high enough energy for the rebounding nucleus to emit a significant scintillator signal. Antineutrinos are detectable through Inverse Beta Decay (IBD), as in

Equation 1.1.9.

$$\bar{\nu}_e + p \rightarrow n + e^+ \tag{1.1.9}$$

However, the majority of detected neutrino interactions in SNO+ come from neutrino electron ($\nu - e$) elastic scattering (ES).

There are two leading order channels that $\nu - e$ ES can take. One is mediated by the Z boson, called the Neutral Current (NC) interaction. The other is mediated by the W boson, called the Charged Current (CC) interaction. The CC interaction is only available to ν_e, as the incoming energies of the neutrinos are not high enough to produce either a muon or a tau. The Feynman diagrams of these interactions are shown in Figure 1.5.



(a) NC (b) CC

Figure 1.5: Feynman diagrams for $\nu - e$ ES. The NC interaction (a) is available to all neutrino flavours. The CC interaction (b) is only available to ν_e due to energy contraints.

The differential cross-section of $\nu - e$ ES in the laboratory frame (where the initial momentum of the electron is 0) is shown in Equation 1.1.10 [36].

$$\frac{d\sigma}{dT_e}(E_\nu, T_e) = \frac{2G_F^2 m_e}{\pi}\left[g_1^2 + g_2^2\left(1 - \frac{T_e}{E_\nu}\right)^2 - g_1 g_2 \frac{m_e T_e}{E_\nu^2}\right] \tag{1.1.10}$$

Where T_e is the kinetic energy of the outgoing electron, G_F is the Fermi coupling constant, and E_ν is the energy of the incoming neutrino. The values of g_1 and g_2 are dependent on the neutrino flavour, and are defined as in Table 1.1 [36].

Radiative corrections must be introduced when measuring solar neutrinos

Neutrino Flavour	g_1	g_2
ν_e	$\frac{1}{2} + \sin^2(\theta_W)$	$\sin^2(\theta_W)$
$\nu_{\mu,\tau}$	$-\frac{1}{2} + \sin^2(\theta_W)$	$\sin^2(\theta_W)$

Table 1.1: Values of g_1 and g_2 in the differential cross-section for $\nu - e$ ES for different neutrino flavours. θ_W is the weak mixing angle, or Weinberg angle.

with a high flux [43]. When investigating neutrinos with energies >5 MeV, these corrections to the cross section reduce the probability of an electron recoil by $\sim 4\%$.

Of particular interest to the work in this thesis is the angular correlation between the incoming neutrino and the outgoing electron. While the direction of the incoming neutrino is important for background rejection of solar neutrinos, only the direction of the outgoing electron can be studied, meaning an understanding of the kinematics is crucial to setting limits on the accuracy of a possible reconstruction-based signal selection. By treating the interaction as a perfectly elastic scatter using relativistic kinematics (and assuming a massless neutrino), it's possible to show the angle between the incoming neutrino and the outgoing electron is given by Equation 1.1.11 [44].

$$\cos(\theta_{\nu-e}) = \frac{m_e + E_\nu}{E_\nu}\sqrt{\frac{E_e - m_e}{E_e + m_e}} \tag{1.1.11}$$

Where $\theta_{\nu-e}$ is the scattering angle, m_e is the electron mass, E_ν is the incoming energy of the neutrino and E_e is the outgoing energy of the electron. This means the scattering angle is determined by the outgoing energy of the scattered electron.

1.2 Solar Neutrinos

Solar neutrinos have long provided experimental motivation for physicists. The Sun produces neutrinos through nuclear processes, meaning that study of the neutrino flux from the Sun can provide information about the elemental composition and energetic processes within the Sun itself. Solar neutrinos were therefore an area of high interest for physicists in the latter half of the twentieth century. Initial investigations of this flux led to what became commonly known as the Solar Neutrino Problem (SNP).

Experimental measurements of the solar neutrino flux demonstrated a deficit when compared to leading solar models. In 1998, the Homestake Chlorine Detector published a rate of $2.56 \pm 0.16(stat) \pm 0.16(syst)$ SNU (Solar Neutrino Units; 1 SNU = 10^{-36} events/atom/sec) [7]. Predictions from theory at the time indicated an expected flux in chlorine detectors between 6.4 ± 1.4 SNU [45] and $9.3^{+1.2}_{-1.4}$ SNU [46]. Deficits in observed solar neutrino flux were also found in gallium detectors [47,48] and water Cherenkov detectors [49], although the discrepancy differed in different target media due to the different energy thresholds. Additionally, a study of atmospheric neutrinos using the Kamiokande-II detector saw a deficit in ν_μ flux, detecting only 58$\pm$7% of the predicated flux from MC studies [50], demonstrating that the SNP went beyond that of a solar model issue. The SNP was solved by the discovery of neutrino oscillations (handled mathematically in Section 1.1), by both the Super-Kamiokande experiment for atmospheric neutrinos [11] and the SNO experiment for solar neutrinos [9,10].

In the years since the solution to the SNP was found, solar neutrinos have continued to be studied at neutrino detectors, both for the measurement of neutrino oscillation parameters and to study solar models. They also provide a directional source with which to study directionality within a scintillator detector. This section will outline the types of processes within the Sun that produce neutrinos.

1.2.1 The Proton-Proton Chain

The Proton-Proton (PP) chain is named as such because it starts with two protons. There are several variations and paths [51], but all versions involve the creation of Helium from Hydrogen via $4\,^1\mathrm{H}^+ + 2\,\mathrm{e}^- \rightarrow {}^4\mathrm{He}^{2+} + 2\,\nu_\mathrm{e}$. The PP chain begins as follows (where E_ν is the emitted neutrino energy [52]):

$$\mathrm{p} + \mathrm{p} \rightarrow {}^2\mathrm{H} + e^+ + \nu_e \qquad E_\nu \leq 0.420\,\mathrm{MeV} \tag{1.2.1}$$

A second less common process (0.4% [51]) for the fusion of two protons is also possible, in the form:

$$\mathrm{p} + \mathrm{p} + e^- \rightarrow {}^2\mathrm{H} + \nu_e \qquad E_\nu = 1.442\,\mathrm{MeV} \tag{1.2.2}$$

The formation of ^{3}He then follows through the reaction:

$${}^2\mathrm{H} + \mathrm{p} \rightarrow {}^3\mathrm{He} + \gamma \tag{1.2.3}$$

From this point, the PP chain has multiple paths that it can undergo. The relative probabilities of each path are dependent on temperature [53]. In the Sun, PPI is the most common path (85% [51]), and involves one further interaction:

$${}^3\mathrm{He} + {}^3\mathrm{He} \rightarrow {}^4\mathrm{He} + p + p \tag{1.2.4}$$

PPII (14.98% [51]) involves the fusion of a ^{3}He with a preexisting ^{4}He:

$${}^3\mathrm{He} + {}^4\mathrm{He} \rightarrow {}^7\mathrm{Be} + \gamma \tag{1.2.5}$$

$${}^7\mathrm{Be} + e^- \rightarrow {}^7\mathrm{Li} + \nu_e \qquad E_\nu = \begin{cases} 0.862\,\mathrm{MeV}\,(89.7\%) \\ 0.384\,\mathrm{MeV}\,(10.3\%) \end{cases} \tag{1.2.6}$$

$${}^7\mathrm{Li} + \mathrm{p} \rightarrow {}^4\mathrm{He} + {}^4\mathrm{He} \tag{1.2.7}$$

PPIII (0.02% [51]) involves the creation of ^{8}B from ^{7}Be:

$$^3\text{He} + {}^4\text{He} \rightarrow {}^7\text{Be} + \gamma \tag{1.2.8}$$

$$^7\text{Be} + p \rightarrow {}^8\text{B} + \gamma \tag{1.2.9}$$

$$^8\text{B} \rightarrow {}^8\text{Be} + e^+ + \nu_e \qquad E_\nu \lesssim 15\,\text{MeV} \tag{1.2.10}$$

$$^8\text{Be} \rightarrow {}^4\text{He} + {}^4\text{He} \tag{1.2.11}$$

A final path is PPIV (2×10^{-5}% [51]), where ^{4}He is formed directly from the fusion of ^{3}He with a proton:

$$^3\text{He} + p \rightarrow {}^4\text{He} + e^+ + \nu_e \qquad E_\nu \leq 18.773\,\text{MeV} \tag{1.2.12}$$

There are a total of five interactions that emit neutrinos within the variations of the PP chain: pp (1.2.1), pep (1.2.2), ^{7}Be (1.2.6), ^{8}B (1.2.10) and Hep (1.2.12). While there has been experimental evidence for the detection of pp [54, 51], pep [55, 51], ^{7}Be [56, 51] and ^{8}B [6, 51] neutrinos, Hep neutrinos have not yet been detected despite their high energies, implying that PPIV is very subdominant.

1.2.2 The CNO Cycle

The other nuclear reaction chain that emits neutrinos is the Carbon-Nitrogen-Oxygen (CNO) Cycle. As with the PP chain, there are multiple paths for the CNO cycle to take, all of which create Helium from Hydrogen in the net reaction of $4\,^1\text{H}^+ + 2\,\text{e}^- \rightarrow {}^4\text{He}^{2+} + 2\,\nu_\text{e}$. Unlike the PP chain, the reactions in the CNO cycle use carbon, oxygen, nitrogen or fluorine as catalysts.

The first path available in the Sun is CNOI (99.95% [57]):

$$^{14}\mathrm{N} + p \rightarrow {}^{15}\mathrm{O} + \gamma \tag{1.2.13}$$

$$^{15}\mathrm{O} \rightarrow {}^{15}\mathrm{N} + e^{+} + \nu_e \qquad E_\nu \leq 1.732\,\mathrm{MeV} \tag{1.2.14}$$

$$^{15}\mathrm{N} + p \rightarrow {}^{12}\mathrm{C} + {}^{4}\mathrm{He} \tag{1.2.15}$$

$$^{12}\mathrm{C} + p \rightarrow {}^{13}\mathrm{N} + \gamma \tag{1.2.16}$$

$$^{13}\mathrm{N} \rightarrow {}^{13}\mathrm{C} + e^{+} + \nu_e \qquad E_\nu \leq 1.199\,\mathrm{MeV} \tag{1.2.17}$$

$$^{13}\mathrm{C} + p \rightarrow {}^{14}\mathrm{N} + \gamma \tag{1.2.18}$$

The second variation on the cycle is CNOII (0.05% [57]):

$$^{14}\mathrm{N} + p \rightarrow {}^{15}\mathrm{O} + \gamma \tag{1.2.19}$$

$$^{15}\mathrm{O} \rightarrow {}^{15}\mathrm{N} + e^{+} + \nu_e \qquad E_\nu \leq 1.732\,\mathrm{MeV} \tag{1.2.20}$$

$$^{15}\mathrm{N} + p \rightarrow {}^{16}\mathrm{O} + \gamma \tag{1.2.21}$$

$$^{16}\mathrm{O} + p \rightarrow {}^{17}\mathrm{F} + \gamma \tag{1.2.22}$$

$$^{17}\mathrm{F} \rightarrow {}^{17}\mathrm{O} + e^{+} + \nu_e \qquad E_\nu \leq 1.740\,\mathrm{MeV} \tag{1.2.23}$$

$$^{17}\mathrm{O} + p \rightarrow {}^{14}\mathrm{N} + {}^{4}\mathrm{He} \tag{1.2.24}$$

There are other variants of the CNO cycle that are possible, but due to the temperatures and elemental composition of the Sun, their contribution is negligible [53]. Experimental evidence has been shown for the detection of CNO neutrinos from the Sun [57], within an energy range of 780 keV to 885 keV where all three neutrino emitting processes (^{13}N, ^{15}O and ^{17}F) are present.

1.2.3 Solar Neutrino Energy Spectrum

The emitted neutrinos from each of these interactions have distinct energy spectra. The prominence of each variation of the chains and cycles would be reflected in the relative fluxes of neutrinos at different energies detected on Earth. This

information can then be used for updated solar models as more precise measurements become possible with larger, more sensitive detectors.

The energy spectra of solar neutrinos, emitted as part of both the PP chain and the CNO cycle, can be seen in Figure 1.6.

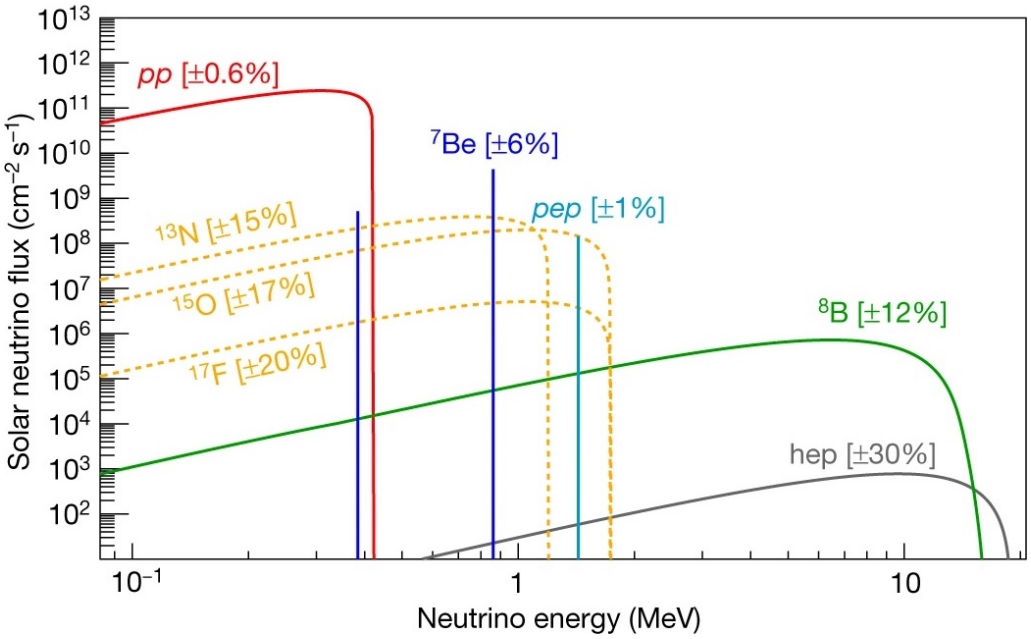


Figure 1.6: Energy spectrum of solar neutrinos from both the PP chains and the CNO cycle. Figure taken from [51], and made using data from [58] and fluxes from [59].

1.3 Photon-Based Neutrino Detection

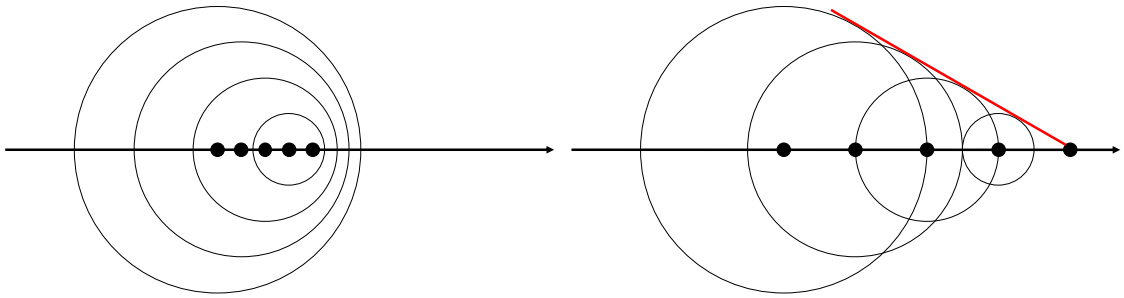
Neutrino experiments utilise a variety of technologies to detect the products of neutrino interactions in matter. The detection method used will be chosen based on the requirements of the neutrino study being conducted. The energy range, interaction products, and precision requirements must all be accounted for when selecting technologies for a new detector. While Time Projection Chambers (TPCs) are quickly becoming more common in neutrino beam experiments, photon-based detection is still used for many large scale solar neutrino detectors and $0\nu\beta\beta$ searches.

Photon-based detectors largely fall into one of two categories: Cherenkov and scintillator. Cherenkov and scintillator detectors do not tend to have the precision readout of position found in noble gas TPCs, which means that track reconstruction is rarely available. However, there are still many benefits to photon-based detection. The technology does not require the large voltages used in TPCs, making it cheaper to run and more easily scalable to large volumes. Many photon-based detectors do not require cryogenic temperatures to function, as is needed for the use of liquid noble gases, as is common in TPCs. Both Cherenkov and scintillator detectors have their own advantages and disadvantages. This section describes the processes behind both Cherenkov and scintillation light emission, and the possible methods for combining the detection techniques.

1.3.1 Cherenkov Detectors

Cherenkov detectors have contributed significantly to neutrino physics over the past decades. Both the SNO detector [9] and the Super-Kamiokande detector [11] used Cherenkov detection to measure neutrino oscillation. Some experiments even take advantage of the natural abundance of water and ice on earth, placing Cherenkov neutrino detectors in the ocean, such as ANTARES [60] and KM3NeT [61], or in the antarctic ice, such as IceCube [62].

Cherenkov radiation is emitted when charged particles travel through a dielectric material faster than the speed of light in that material [63]. This phenomenon was originally observed by Pavel Cherenkov [64, 65], and later formalised theoretically by Ilya Frank and Igor Tamm [66, 67]. As the charged particle moves faster than the electromagnetic field around it, it creates an asymmetric polarisation of the dielectric medium according to the direction of motion. The elementary electro-magnetic waves emitted from the individual points along the electron's track combine coherently, causing a wave front and the emission of light from the medium. This can be seen diagrammatically in Figure 1.7.



(a) $v < \frac{c}{n}$ (b) $v > \frac{c}{n}$

Figure 1.7: Diagrams showing the mechanism for the emission of Cherenkov radiation. In each diagram, the black points represent an individual point on the particle's trajectory, and the circles show the emitted electromagnetic wave from each point. In (a), the particle is moving with $v < \frac{c}{n}$, so the elementary electromagnetic waves do not coherently combine. In (b), $v > \frac{c}{n}$ and the elementary waves combine to form the red wave front.

The wavefronts are emitted at an angle according to the movement of both the charged particle and the speed-of-light reaction of the polarised material. This can be seen in Figure 1.8, and leads to the expression of the Cherenkov angle, θ_{ch}, found in Equation 1.3.1 [67].

$$\cos(\theta_{ch}) = \frac{c_n}{v} = \frac{1}{n\beta} \tag{1.3.1}$$

where c_n is the speed of light in the medium, v is the speed of the particle, n is the refractive index of the medium and β is v/c.

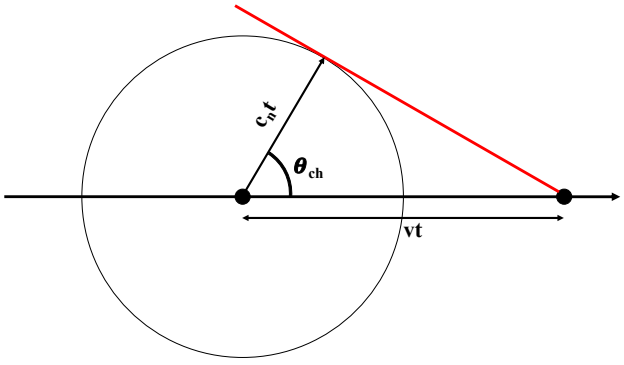


Figure 1.8: Derivation of the Cherenkov angle. In a time t, the particle moves vt between the black dots. The elemental wave travels a distance $c_n t$ from the original position of the particle. This allows for the calculation of θ_{ch}.

The energy loss of the electron through Cherenkov emission is defined by Equation 1.3.2 [67,68].

$$\frac{dE}{dx} = \frac{q^2}{c^2} \int_{\beta n > 1} \omega d\omega \left(1 - \frac{1}{\beta^2 n^2}\right) \tag{1.3.2}$$

Where dE is the energy loss, dx is the distance travelled and q is the charge of the particle. The number of photons (N) emitted between wavelengths λ_1 and λ_2 can then be given by Equation 1.3.3 [67].

$$\frac{dN}{dx} = 2\pi\alpha \left(\frac{1}{\lambda_2} - \frac{1}{\lambda_1}\right)\left(1 - \frac{1}{\beta^2 n^2}\right) = 2\pi\alpha \left(\frac{1}{\lambda_2} - \frac{1}{\lambda_1}\right) \sin^2(\theta_{ch}) \tag{1.3.3}$$

Where α is the fine structure constant. Frank and Tamm used this to show that a typical fast electron at the Cherenkov threshold for water ($\beta \approx 3/4$, equivalent to an energy of $\sim$262 keV) will emit $\sim$10 Cherenkov photons, consistent with experimental observations by Cherenkov [67].

These features of Cherenkov radiation create specific advantages and disadvantages for use in neutrino detectors. Advantages include the fact that Cherenkov radiation is emitted in any clear dielectric medium, including water. This leads to relatively low cost associated with the target medium of the detector. Cherenkov radiation also offers the ability to reconstruct a direction of a particle, due to the signature Cherenkov ring around the direction of motion. These rings can also be used for particle identification between electrons and muons. Electrons, being the lighter particle, are more easily scattered while travelling through the water, meaning electron Cherenkov rings appear "fuzzier" [69].

However, Cherenkov detectors also suffer from some disadvantages. Cherenkov radiation has a minimum energy threshold, requiring that $\beta > \frac{1}{n}$. Cherenkov radiation also has a comparatively low photon-yield, only emitting $\sim$10s of photons per MeV. This leads to a low precision for energy reconstruction in Cherenkov detectors.

Cherenkov detectors are well suited to neutrino studies where the neutrino source has a known direction, particularly solar neutrino studies. Flux measurements do not depend as rigidly on energy precision, and backgrounds can be rejected based on the travel direction of the scattered electron. However, very low energy neutrino studies, or searches that rely on a high precision of energy, are better suited to scintillator detectors.

1.3.2 Scintillator Detectors

Scintillator detectors have a similarly solid foundation already in neutrino physics. Liquid scintillator targets were used in the Cowan-Reines experiment [4] for the initial discovery of neutrinos, although they were not used to detect the products of a neutrino interaction. Instead they were used as a detection mechanism for the photons produced by electron-positron annihilation and neutron capture. Liquid scintillator detectors have been used for low energy solar neutrino studies, such as Borexino [70], low energy reactor anti-neutrino measurements, such as KamLAND [71] and Daya Bay [72], and $0\nu\beta\beta$ searches, such as KamLAND-Zen [73].

Unlike Cherenkov radiation, scintillation emission cannot occur in all media, but requires a scintillator. The molecules are excited as a charged particle traverses and deposits energy into the scintillator. The molecules then relax back to the ground state by emitting a photon [74]. This deexcitation energy will be individual to a given molecule, leading to a unique emission spectrum.

Scintillation emission corresponds to one of two luminescent phenomena: fluorescence or phosphorescence. For fluorescence, this process is a simple transition between states of the same multiplicity ($\Delta S = 0$), whereas phosphorescence involves the forbidden transition between states of different multiplicity ($\Delta S \neq 0$) [75]. This means the phosphorescence occurs over a much longer time scale, with lifetimes ranging between the milliseconds scale to hundreds

of seconds [76]. Typical fluorescence lifetimes range between nanoseconds and microseconds [76,77]. The phosphorescence can create a long-lived contribution to the emitted light, but is a rarer phenomenon in scintillators, as the molecule must first have been excited in a way that allowed for a $\Delta S \neq 0$ transition from the ground state — for example, ionisation. This is more common with heavier charged particles, creating a different time profile response to different types of ionising radiation in scintillators.

Large-scale detectors often use organic liquid scintillators due to the ability to create large quantities at the required purity levels [78]. These organic scintillators frequently contain benzene rings, such as linear alkyl-benzene (LAB) used in the SNO+ experiment. While three of the carbon valence electroncs are required for σ bonds between the carbon and hydrogen atoms, the one remaining electron is found in the perpendicular p-orbital. These orbitals overlap, and a π orbital of delocalised electrons is formed [74]. This can be seen in Figure 1.9.

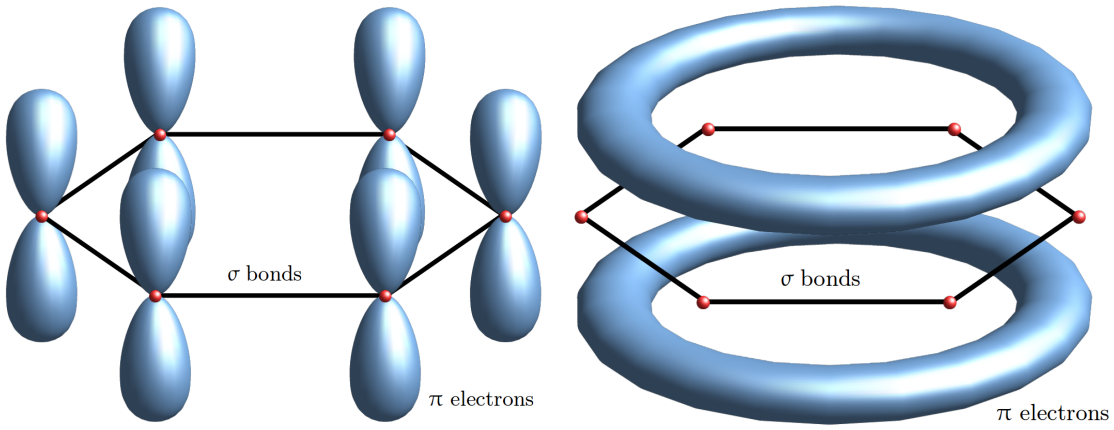


Figure 1.9: The electron orbitals present in a benzene ring. The individual p-orbitals in (a) overlap to form a delocalised band of electrons in the π orbital, as seen in (b). Figure taken from [79].

The delocalised ring of electrons has energy levels that correspond to the emission of optical photons, causing the scintillation used in large-scale particle detectors [74].

Once a photon is emitted, it can have a high probability of reabsorption into the scintillator to excite another molecule. This is not a desirable quality for a large-scale detector, as it means light will not reach the light detection technology placed around the outside of the scintillating target medium. There is a natural shift in emission compared to absorption spectra in scintillators due to vibrational relaxation [80], meaning that the use of a single pure scintillator is not impossible, but it is often desired to increase the detected light-yield further by using an additional wavelength shifter.

In a typical scintillator cocktail, there will be a solvent and a primary fluor, which acts as a wavelength shifter. While the solvent is excited by the charged-particles, it does not relax to the ground state by emitting a photon. Instead, it non-radiatively transmits the energy to the primary fluor, causing that to enter an excited state [74]. The fluor then deexcites by emitting a photon, which will be at a shifted wavelength compared to the solvent's emission spectrum. This process can be repeated through an additional secondary fluor, bringing the emitted photon's wavelength even further from the peak absorption of the solvent. The addition of fluors can also improve light yield due to their improved quantum yield — the proportion of their deexcitations that are undergone radiatively, and therefore the number of photons emitted. Individual detectors will tune the exact scintillator cocktail to the needs of the experiment, with considerations including the method of light detection and the size of the detector.

The light yield of a scintillator is given by Birks' Law [81], as seen in Equation 1.3.4.

$$\frac{dN}{dx} = L_0 \frac{\frac{dE}{dx}}{1 + k_B \frac{dE}{dx}} \tag{1.3.4}$$

Where N is the number of emitted photons, L_0 is the efficiency of the scintillator, and $\frac{dE}{dx}$ is the energy loss per unit length of the particle. The Birks' constant, k_B, is the product of two constants: the proportionality constant between concentration of ionised molecules and the energy loss, and the probability of an

ionised molecule being excited instead of an unionised one. However, as these two constants only appear as a product and are both dependent on the scintillator, they are considered to be a single constant. This means the Birks' Law indicates that light yield will be quenched due to the ionisation of molecules in the scintillator. This effect is more prominent for high values of $\frac{dE}{dx}$, where the light yield plateaus to a constant $\frac{L_0}{k_B}$. Light yield varies significantly between scintillator cocktails. The scintillator cocktail used for SNO+ (described in Section 3.2) showed yields of > 10000 photons per Mev [82].

This high light yield of scintillators constitutes the major advantage of scintillator detectors. The large number of detected photons provides a precise reconstruction of both energy and position. For searches such as $0\nu\beta\beta$, good energy resolution is crucial for the ability to distinguish signal from background (as discussied in Section 1.1.3). Good position resolution also contributes to background rejection, as many backgrounds come from "external" sources around the target medium and as such can be removed with a fiducial volume cut. Scintillators also do not have an energy threshold for photon emissions, meaning very low energy studies of sources such as solar neutrinos are possible.

The primary disadvantage of scintillator detectors is the lack of directional information in the scintillation signal. Scintillation light is emitted isotropically, and for most particle interactions the resolution is not sufficient to reconstruct particle tracks. This means that background rejection cannot be done on the basis of incoming neutrino direction. Not only does this impact solar neutrino studies where the source has a single known direction, but also any studies for which solar neutrinos are a background. For example, in the $0\nu\beta\beta$ search in the SNO+ detector, ^{8}B solar neutrinos are an irreducible background in the region of interest [79]. These neutrino experiments could benefit greatly from the directional information present in Cherenkov-based detectors, if the two technologies could be used simultaneously.

1.3.3 Hybrid Detectors

The topic of combining Cherenkov and scintillation detection techniques has attracted significant interest from the neutrino physics community in recent years [12]. Several methods have been proposed, with table-top scale prototypes already demonstrating the ability to distinguish between Cherenkov and scintillation signals. This subsection will offer an overview of the state of the field on hybrid Cherenkov/scintillation technologies and future detectors.

1.3.3.1 Correlated and Integrated Directionality

The Correlated and Integrated Directionality (CID) method was developed for use in the Borexino detector [22,83], with results first published in March 2022. In CID, individual events are not investigated for directional information. Instead, a large dataset is integrated over to find the angular distribution of individual photons, correlated with the direction of the sun. Cherenkov light is emitted instantaneously compared to the excitation and relaxation time of a scintillator. Therefore, only the first and second detected photons in a given event are used (after corrections are applied for time of flight across the detector). This creates the highest probability that the photons are Cherenkov, and therefore contain information about the direction of travel of the electron.

Angular information is measured in terms of α, the angle between the emitted photon direction and the solar direction, as shown in Figure 1.10.

Data from Phase 1 (May 2007–May 2010) of the Borexino experiment was used to test this method. 19904 events were selected with reconstructed electron energies between 0.5 MeV and 0.8 MeV. In this region, the dominant solar signal originates from ^{7}Be neutrinos, with small contributions from pep and CNO neutrinos. The distribution in α for the first detected photon from each event can be seen in Figure 1.11. This distribution is compared to simulated Monte Carlo (MC) distributions for solar neutrinos and isotropic electron background.

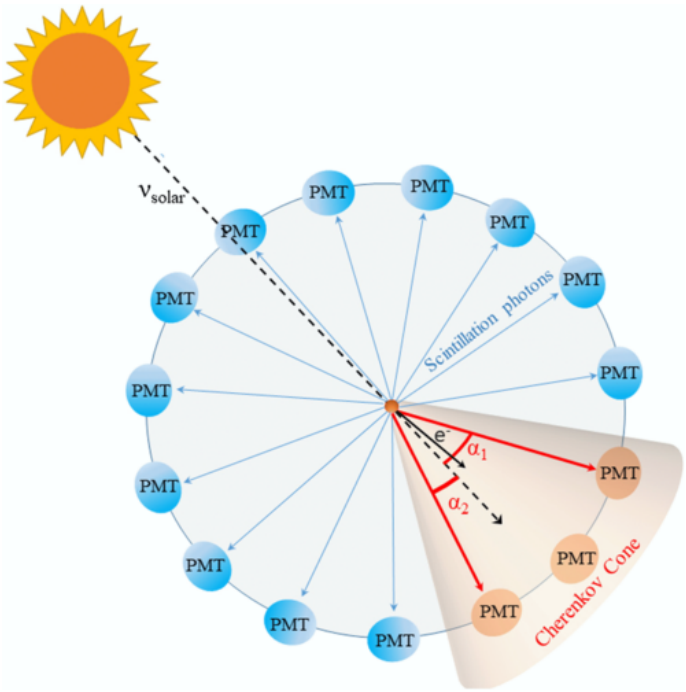


Figure 1.10: Definition of α, the angular parameter used in CID in the Borexino experiment. While scintillator light (blue) is not correlated to the solar direction, Cherenkov light (red) is emitted in a cone around the direction of travel. Only the first two detected photons are used for CID, displayed with angles α_1 and α_2. Figure taken from [83].

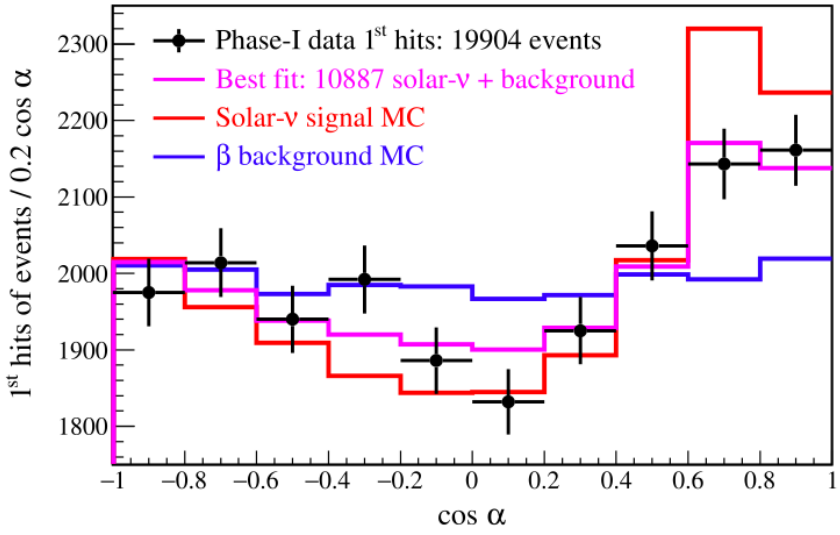


Figure 1.11: Distribution in α of the first detected photons for Phase 1 of the Borexino experiment. Distributions for simulated MC of solar neutrinos (red) and isotropic electron background (blue) are also included. The best fit distribution (pink) contained 10887 solar neutrinos. Figure taken from [83].

By performing a χ^2 fit over the distributions of the first and second detected photons (the details of which can be found in [22]), the number of solar neutrinos within the dataset was found to be $N_{solar-\nu} = 10887^{+2386}_{-2103}(stat) \pm 947(syst)$. A pure background hypothesis, with no detection of solar neutrinos, was rejected with a $> 5\sigma$ significance.

This result constitutes the first measurement of sub-MeV solar neutrinos using directional information from Cherenkov light in scintillator. This method could be used in combination with other event information (most prominently energy and position) to statistically separate solar events in large liquid scintillator detectors. However, for CID to produce result with large significance, it requires a large dataset to integrate over. It also cannot produce directional information for a single event. CID offers a method to determine the flux of solar neutrinos in a detector using the sun's direction, but cannot be used to reject solar neutrinos as backgrounds from other studies on an individual basis. In order to do this, methods of further separating the Cherenkov light are desired.

1.3.3.2 Wavelength Separation and Dichroicons

One method of hybridisation utilises the fact that the emitted wavelength of scintillation light is determined by the scintillation cocktail chosen and falls within a relatively narrow band, while Cherenkov light has a wide spectrum of emission [84]. This creates the opportunity for spectral sorting, where photons are labelled as scintillation or Cherenkov based on their wavelength. An example of a comparison between Cherenkov and scintillation spectra can be seen in Figure 1.12. It can be seen that long wavelength photons can be assumed to be Cherenkov, opening the possibility of separating Cherenkov photons for directionality within a scintillator detector.

While simple wavelength filters could allow some photon-detectors to be designated as purely for scintillation or Cherenkov, this would reduce the effective coverage of the detector as a whole, reducing the achievable energy resolution.

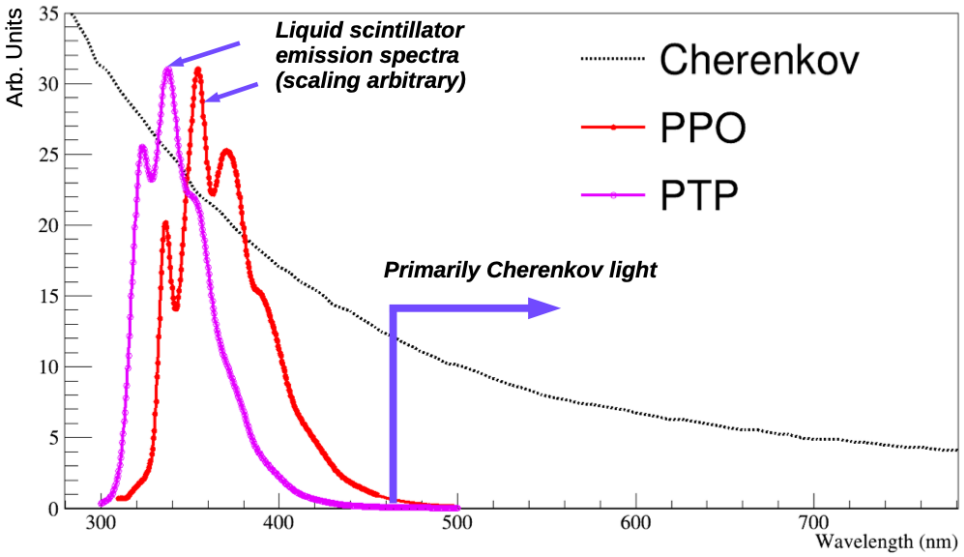


Figure 1.12: A comparison of Cherenkov and scintillation spectra, using the common fluors 2,5-Diphenyloxazole (PPO) and p-terphenyl (PTP). The scintillation spectra are relatively narrow at short wavelengths, whereas the Cherenkov spectra continues up to longer wavelengths. Photons with wavelengths above ∼460 nm are primarily Cherenkov photons. Figure taken from [85].

It would be desirable to sort the photons by wavelength, while still ensuring the majority are detected. One method of doing so is the "dichroicon" [21]. Dichroicons are based on Winston cones [86], a maximal-concentration reflector used in many photon-based detectors. Dichroicons replace the standard reflective mirror with wavelength filters, concentrating long wavelength photons to a primary photon-detector, while short wavelength photons are allowed to pass through to a secondary photon-detector. Multiple designs of dichroicon have been suggested involving different configurations of secondary detection mechanisms. A schematic of a prototype is shown in Figure 1.13, which uses two photomultiplier tubes (PMTs) and a long-pass filter.

The dichroicon allows short wavelength photons to pass through to a R1408 8-inch Hamamatsu PMT. The long wavelength photons, assumed to be Cherenkov, are instead concentrated down to a R7600-U20 Hamamatsu 1-inch square PMT. This allows directional information to be derived by only investigating information from the smaller primary PMT, while the high yield scintillation

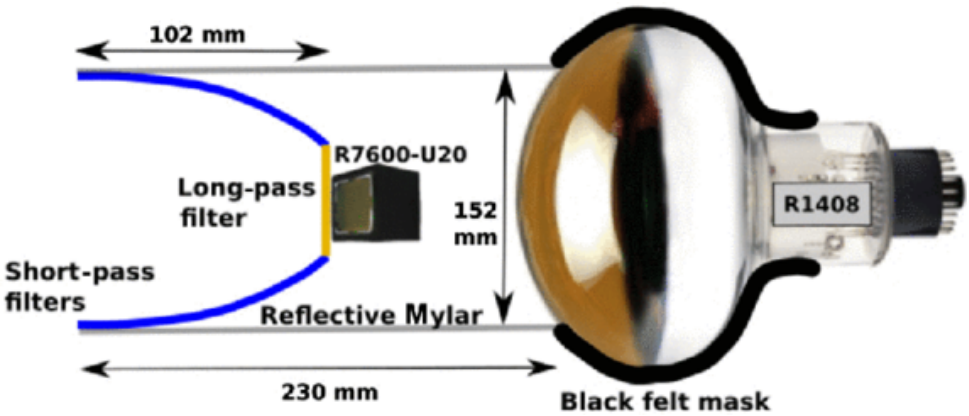


Figure 1.13: Schematic of a prototype dichroicon. The short-pass filter allows short wavelength photons through to a R1408 8-inch Hamamatsu PMT. Long wavelength photons (assumed to be Cherenkov) are instead concentrated down to a R7600-U20 Hamamatsu 1-inch square PMT. Figure adapted from [21].

light is still collected by the larger secondary PMT. Investigations of the prototype [21] showed the Cherenkov light could be identified with a 90% purity. The efficiency for detecting the short wavelength light was shown to be ∼30%, but it is expected that with adjustments to the reflector system this could be improved. Additionally, pulse-shape discrimination between β and α particles was demonstrated.

Dichroicons provide a very promising technology for the hybridisation of Cherenkov and scintillation detection mechanisms, maintaining a high detected light yield while still identifying Cherenkov photons to a high purity. However, many Cherenkov photons are still short wavelength, and so the number of detected Cherenkov photons is decreased. Additionally, dichroicons require a more sophisticated photon detection system, increasing costs in order to gain good coverage of a large-scale detector. The potential for investigation of dichroicons in a large-scale detector will be possible in the Eos demonstrator (a 4 ton detector with the ability to deploy various target media, with data taking planned to begin in 2024) [25] and the Theia detector (a prospective detector design planned to be filled with water-based liquid scintillator, with a potential target mass of up to 100 kt) [26].

1.3.3.3 Scintillation Suppression and Water-based Liquid Scintillator

Another method to extract directional Cherenkov information from a scintillator is to reduce the number of scintillation photons emitted, increasing the ratio of Cherenkov to scintillation photons. This method was used in the LSND [23] and MiniBooNE [87] detectors. LSND deployed mineral oil with a low concentration of fluor, using 0.031 g/L butyl-phenyl-bipheny-oxydiazole. For particles with $\beta = 1$, this led to a ratio of $\frac{N_{iso}}{N_{Cher}} \approx 5$ where N is the number of photoelectrons generated, *iso* refers to all isotropic light (including scintillation light and Cherenkov light that was absorbed and remitted isotropically), and *Cher* refers to directly detected Cherenkov light. For electrons with energies >20 MeV, an angular spread of 12° in reconstructed direction was reported. MiniBooNE used pure mineral oil, deploying no additional fluor, and reported angular resolutions <5° for both electrons and muons with energies >100 MeV [24]. Both detectors used the presence of low level scintillation light for improved energy resolution and particle identification.

Scintillation suppression can also by achieved through the use of Water-based Liquid Scintillator (WbLS) [88]. By putting a low concentration of scintillator (1-10%) into water, Cherenkov light can be allowed to dominate while still maintaining the emission of scintillation light for particles below the Cherenkov threshold. However, organic liquid scintillators are generally immiscible in water. In order to introduce the scintillator into the water, the scintillator cocktail is contained within spherical "micelles", shells made of compounds known as surfactants. The surfactants are chain molecules, with a hydrophilic end and a hydrophobic end. The structure of a micelle can be seen in Figure 1.14.

With the liquid scintillator incorporated into the water, it is possible to investigate the possibility for Cherenkov separation and directionality in WbLS. Multiple studies have been conducted on this topic [18, 89–91], with development ongoing [12]. Several demonstrators have been proposed for testing WbLS

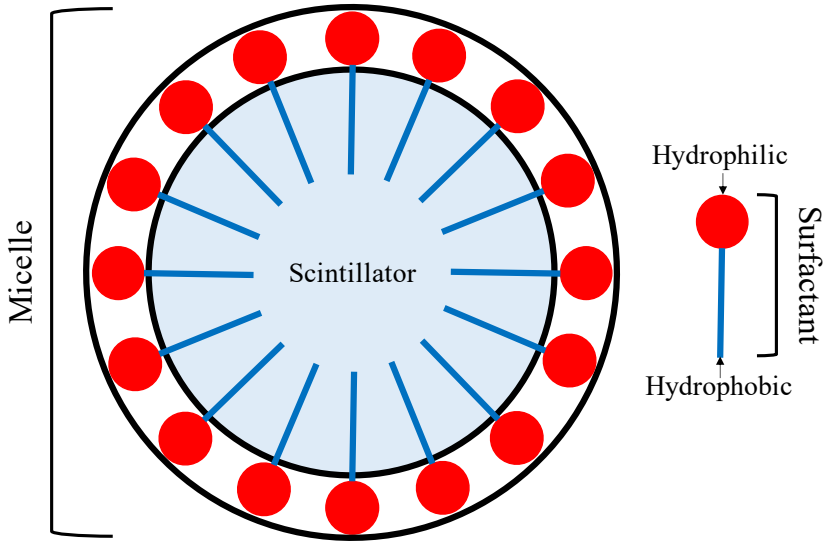


Figure 1.14: The structure of a micelle as used in WbLS. The micelle is made of surfactants, chain molecules with one hydrophobic end and one hydrophilic end. The surfactants create a shell, containing the liquid scintillator within the external water.

at the tonne-scale [12, 25, 92], and the THEIA detector will use WbLS as part of its hybrid detector program [26]. Predictions indicate that THEIA could have the capacity to outperform existing neutrino detectors in the search for the diffuse supernova neutrino background [93]. However, simulated studies have not shown an improvement in potential searches for CNO neutrino flux or $0\nu\beta\beta$ when using WbLS compared to conventional liquid scintillator. There is the potential for this to be improved by the introduction of additional Cherenkov separation techniques [14].

WbLS and other methods of scintillation suppression obtain directional information by operating as a Cherenkov-dominated detector, while benefitting from scintillation light for particle identification and detection of particles below the Cherenkov energy threshold. However, by suppressing the scintillation emission, the precise energy resolution that searches such as $0\nu\beta\beta$ rely on is lost. With a significant development program planned in the coming years, the exact capabilities of different WbLS cocktails will be thoroughly examined, leading to a new type of large scale neutrino detector.

1.3.3.4 Time Separation

As discussed in Section 1.3.2, scintillation light originates from the excitation and relaxation of the molecule to emit light. This process takes a characteristic lifetime, dependent on the exact combination of fluors used. Cherenkov light, however, is emitted instantly as the charged particle travels. This means that another way to separate Cherenkov light from scintillation is by timing, where Cherenkov light should be detected earlier than scintillation light. Additionally, dispersion in large-scale detectors can increase the time separation due to long wavelength light being primarily Cherenkov. Simulated studies of large-scale detectors often use time separation to select for "early" photons, using the anisotropy in the early Cherenkov light to reconstruct direction using methods similar to those used in Cherenkov detectors [13].

Typical scintillator cocktails currently used in neutrino detectors have rise times up to 1 ns, with primary fall times in the range of several nanoseconds [70, 82, 94]. In order to effectively separate the Cherenkov photons from the scintillation for use in direction reconstruction, fast photon detectors can be used. Modern 8 inch PMTs can have transit time spreads (TTSs) of under 700 ps [95]. Smaller PMTs can have much narrower TTSs. The CHESS experiment [96] used 26.2 mm Hamamatsu H11934-200 PMTs with a TTS of 0.27 ns [97] to demonstrate Cherenkov separation in linear alkylbenzene (LAB) with 2 g/L PPO [16], the scintillator cocktail used in the SNO+ experiment. However, smaller PMTs come with higher costs for large detectors when maximising coverage. Another fast photon detection technology is the Large Area Picosecond Photodetector (LAPPD). Commercially available LAPPDs [98] are 20 cm $\times$ 20 cm square tiles comprised of two layered microchannel plates (MCPs) [99]. The LAPPD offers millimetre-scale spatial separation of detected photons and a time resolution of 50 ps [100]. LAPPDs are not yet economically viable for large-scale neutrino detectors, but continued development is underway to investigate the potential for

use in Cherenkov separation in scintillator [12].

Alternatively, instead of speeding up the response of the photon detection technology, time separation of Cherenkov light could be achieved by slowing down the emission of scintillator light. Fast scintillators are often used in scintillator detectors as they offer more precise reconstruction of a position-time vertex. However, if the scintillator is slowed, fast photon detection would not be necessary to resolve the difference between "early" Cherenkov light and "late" scintillation light. Simulated studies of slow scintillators show that direction reconstruction could be possible in a large-scale neutrino detector, using realistic photon detection capabilities [101, 102]. In order to confidently project the potential for slow scintillator directionality, the characteristics of the fluors must be carefully measured. Chapter 2 details the measurements of the time parameters of four slow fluors, including the clear demonstration of time-based Cherenkov separation.

Chapter 2

Slow Fluors for Cherenkov Separation

"Nothing travels faster than the speed of light with the possible exception of bad news, which obeys its own special laws."

- Mostly Harmless, Douglas Adams

Direction reconstruction in scintillator through the use of timing separation is a technique well suited to low-energy studies, especially those that require high energy precision such as the search for $0\nu\beta\beta$. Time separation does not reduce the total light detected, as high-yield scintillators can still be used and no photons are lost to wavelength filtering. However, standard scintillator cocktails currently used in large LS neutrino detectors often have timing profiles faster than standard PMT response times. Fast scintillator emission allows increased precision of position-time reconstruction, as well as the ability to have a short trigger window. However, it decreases the effectiveness of directionality within the detector due to the inability to effectively separate early Cherenkov light. If future detectors wish to prioritise direction reconstruction for background rejection in low energy studies, slower fluors would be desirable.

To properly investigate the possibility of time separation of Cherenkov light in slow scintillators, the emission time profile of the scintillating material must be well known. This will allow the ability to distinguish which photons are

detected "early", and are therefore more likely to be Cherenkov photons for use in directional reconstruction. This chapter will present the measurement and characterisation of the time profiles for several slow scintillator mixtures, and demonstrate the possibility of directionality using these mixtures.

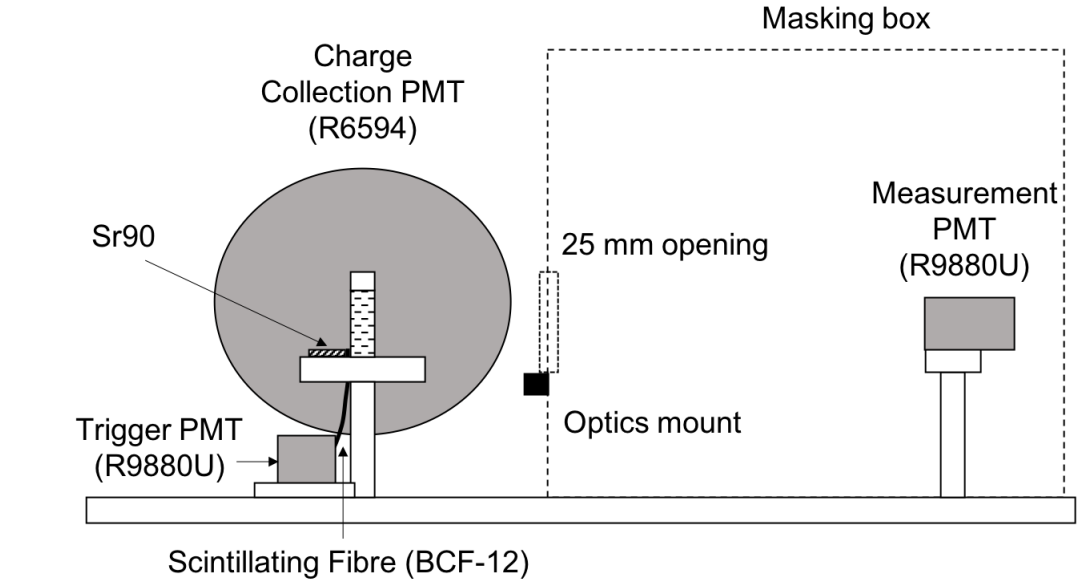
This analysis — including all figures presented in this chapter — was originally published in [20], along with measurements of spectral characteristics and light yields of each mixture. The time parameter measurements presented in the publication were conducted by the author of this thesis, including contributions to the creation of the experimental equipment, acquisition of the data, and development of the analysis methods and computational framework.

2.1 Method of Time Profile Measurement

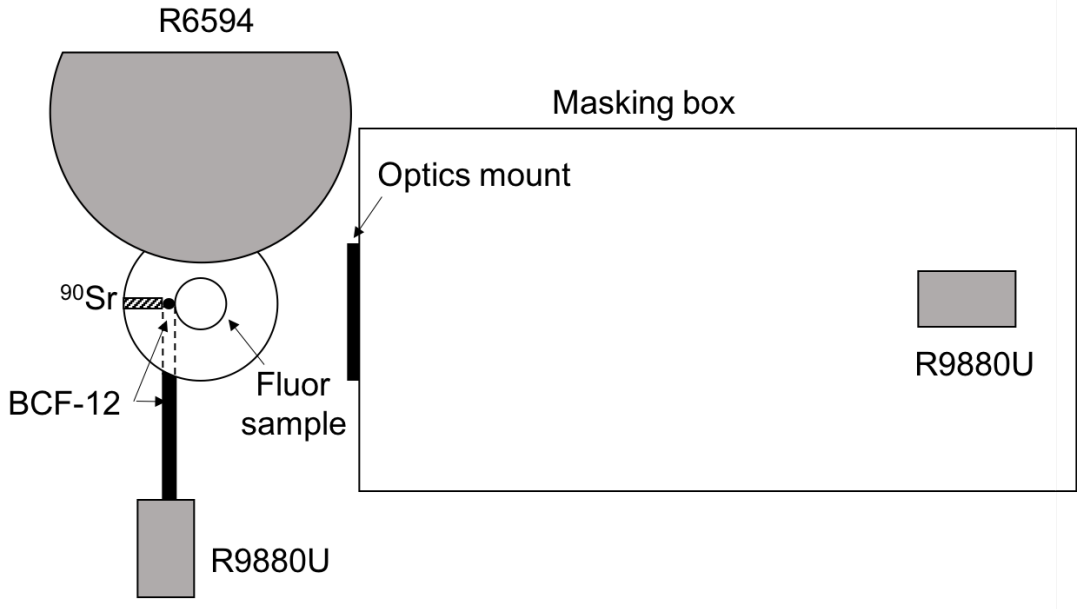
Emission time spectra measurements were conducted using an altered version of the single photon technique first suggested in [103]. A diagram of the experimental set up can be seen in Figure 2.1, and a photograph of the equipment can be seen in Figure 2.2. All equipment was contained within a sealed dark-box to exclude external light sources.

A ^{90}Sr source was used to excite the scintillator. The ^{90}Sr β decays to ^{90}Y, with a Q-value of 545.9 keV [104]. The ^{90}Y then undergoes a subsequent β decay with a Q-value of 2278.5 keV [104]. Before reaching the scintillator, the electron must pass from the source through a 2 mm-diameter scintillating fibre, and then 1 mm of glass vial wall. Through these materials, the electron will lose approximately 1 MeV [105]. This means only the β decay from the ^{90}Y will reach the scintillator, with typical energy depositions within the scintillator below 1 MeV.

Information about each event was stored using three photomultiplier tubes (PMTs). The first was the trigger PMT, a Hamamatsu R9880U-210 (UBA) PMT. This PMT was optically coupled to a 2 mm-diameter Saint-Gobain BCF-12 scintillating fibre using index matching gel. This fibre was threaded through the



(a) Side View



(b) Top View

Figure 2.1: Diagrams of the experimental set up of the emission time profile measurement in the "towards" configuration. Figures taken from [20]

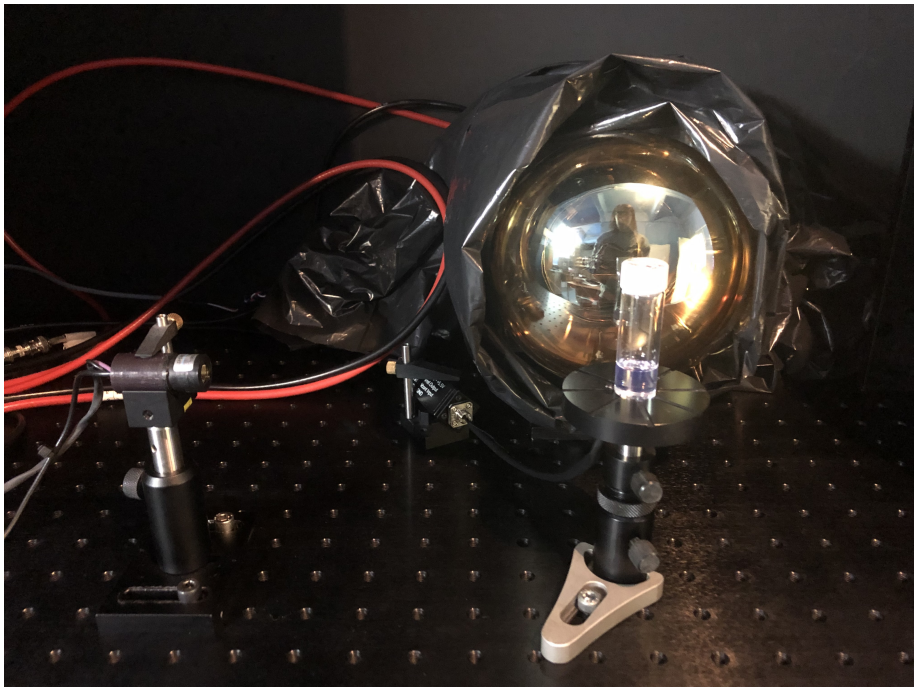


Figure 2.2: Photograph of the apparatus used for time profile measurements in the "away" configuration. The vial of scintillator rests on a stand with the large charge collection PMT placed close to it. The trigger PMT can be seen to the lower left of the charge collection PMT, with a black-coated scintillating fibre threaded through the base of the stand and optically coupled to the trigger PMT. The measurement PMT can be see on the left, which would be placed inside a masking box for data taking.

sample base plate to sit between the ^{90}Sr source and the vial of fluor sample. Light was detected in the trigger PMT as the electron passes through the fibre before it reaches the scintillator. The trigger PMT therefore acts as an independent trigger start for the timing measurement.

The second PMT was the charge collection PMT, a Hamamatsu R6594 PMT. This was placed $\sim$1 cm away from the vial. The charge collected on this PMT for each event was recorded, which is approximately proportional to the number of scintillation photons emitted by the scintillator. This measurement creates a relative scale of energy deposited in the scintillator by the electron. This was used to place a selection cut for events with high energy deposits in order to get rid of "tail" events – events with low energy depositions which may have less clearly defined time profiles.

The third PMT was the measurement PMT, another Hamamatsu R9880U-210 (UBA) PMT. This PMT was positioned inside a masking box with an adjustable iris, and placed at a distance from the scintillator sample that would allow a less than 10% occupancy (usually 10–20 cm, dependent on yield). The occupancy was defined as the percentage of hits in the trigger PMT that are coincident with a hit in the measurement PMT. A 10% maximum occupancy was chosen to reduce the probability of "multiple hits". When the occupancy is too high, there is a high probability that the measurement PMT will detect more than one photon for a given electron event. This will bias the time profile measurement, as only the first photon hit will be measured, leading to a loss in late-time photon hits in the measured profile. At a 10% occupancy, the probability of multiple hits is considered negligible. The masking box is used to reduce the effect of reflections and scattering of photons within the apparatus.

An additional experimental configuration was also considered. In the set up shown in Figure 2.1, the ^{90}Sr source is pointed towards the measurement PMT. This means a significant Cherenkov signal would be expected alongside the scintillator profile. To quantify this, the measurements were also performed using a configuration where the source is pointed away from the measurement PMT (placed on the same side of the vial as the measurement PMT). Cherenkov light in this configuration would result from electron scattering, photon scattering and reflections. This configuration was used as a comparison for the observation of the Cherenkov peak.

For the measurement of the time profile, events were selected using a time-based trigger. An event was triggered on a coincidence between the trigger and measurement PMTs within an 800 ns window. The time profile was then built using offline analysis which calculated the ΔT between the digitised measurement and trigger signals, and charge cuts were applied to select for events with a high energy deposition. Details of the digitisation process and ΔT calculation

can be found in [20]. The impact of time resolution from the digitisation process was considered negligible and was accounted for by measuring the Impulse Response Function.

2.1.1 Time Resolution Measurement

The time resolution of the experimental set up was quantified by measuring the Impulse Response Function (IRF) – the time response of the equipment to an instantaneous impulse of light. The scintillator sample was replaced by a sample of distilled water, meaning that only a Cherenkov signal would be emitted. The time profile was built in the same way as described above for scintillation profiles, and can be seen in Figure 2.3.

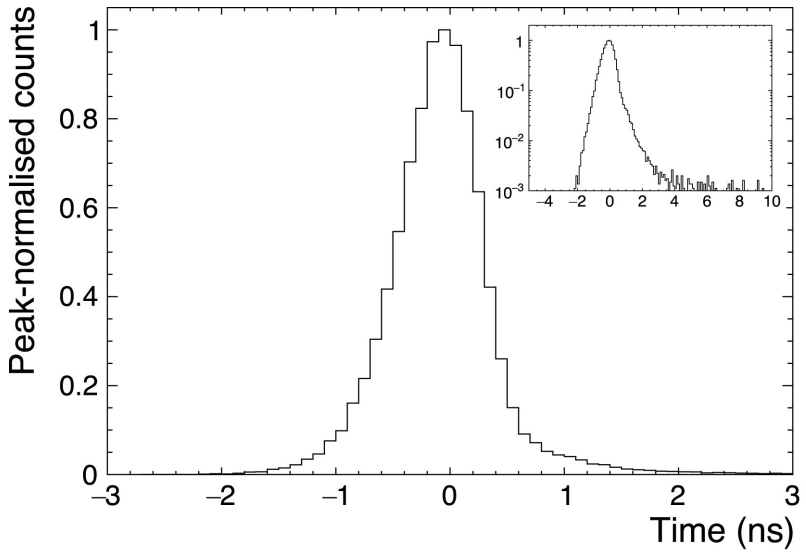


Figure 2.3: The impulse response function of the time profile measurement set up, measured using a Cherenkov signal from distilled water, with an inset showing the profile on a logarithmic scale. Figure taken from [20].

A Gaussian fit to the IRF provides a time resolution of approximately 390 ps. However, due to the non-Gaussian shape, the function was used in its entirety during the analysis of the scintillators. By measuring and building the IRF with the same method as the scintillation profiles, time resolution effects from all stages of the data taking process are accounted for.

2.2 Analysis of Scintillator Time Profiles

To characterise the timing profile of the fluors, an empirical model of the scintillation emission time spectrum was used, as seen in Equation 2.2.1.

$$f_s(t) = \sum_{i=1}^{n} \left(A_i \frac{e^{-\frac{t}{\tau_i}} - e^{-\frac{t}{\tau_r}}}{\tau_i - \tau_r} \right) + A' \cdot \frac{e^{-\frac{t}{\tau'}}}{\tau'} \tag{2.2.1}$$

This equation contains a sum of n components (n = 1 or 2, dependent on fluor), each with an exponential fall time (τ_i), a common rise time (τ_r), and a weighting (A_i). For the majority of the scintillator cocktails (with the exception of some pyrene configurations), fitting was improved by the inclusion of an additional component with an instantaneous rise time, and a fall time τ' on the order of τ_r. This has been attributed to emission of LAB, which occurs at a high wavelength that is not absorbed by most of the candidate fluors.

The scintillation emission profile is then combined with a Cherenkov emission component. The Cherenkov signal is assumed to be emitted instantaneously, as the travel time of the electron through the scintillator ($\sim 10^{-10}$ s) is on the same order of magnitude as the timing response resolution of the experimental set up. The fraction of emitted light comprised of Cherenkov photons is floated as the parameter F_{ch}. The optical emission spectrum of the scintillator cocktail is then defined as in Equation 2.2.2.

$$f_o(t) = (1 - F_{Cheren}) \cdot f_s(t) + F_{Cheren} \cdot \delta(t) \tag{2.2.2}$$

This optical emission spectrum is then convolved with the IRF described previously to create the full response model, as seen in Equation 2.2.3, which can be used to characterise the data.

$$f_r(t) = f_o(t_0 - t) \circledast IRF(t) \tag{2.2.3}$$

A summary of the parameters for this model can be found in Table 2.1.

Parameter	Description
τ_r	Common rise time of scintillator
τ_i	Decay time for ith component
A_i	Fraction of scintillation light in ith component
A'	Fraction of instantaneous component
τ'	Fall time of instantaneous component
F_{Cheren}	Fraction of Cherenkov photons
t_0	Start time for scintillation profile

Table 2.1: Parameters used in response function fitting.

The resulting function was scaled to the number of measured events in the given dataset. The fit was conducted by minimising the negative log-likelihood using a Minuit minimiser. The fit was conducted simultaneously over both the towards and away configurations. Time constants of the scintillator were required to be common between the two configurations, with F_{ch} and t_0 allowed to fit separately. This provided a more robust fit for the scintillator timing parameters, especially τ_r. The Cherenkov component can obscure the rising edge of the scintillator in the towards configuration, leading to a degeneracy in fitting for F_{ch} and τ_r. Fitting both measurements simultaneously reduced the covariance between the Cherenkov component and the rise time.

2.3 Candidate Fluors

Four candidate fluors were chosen for this analysis. All suggested scintillator cocktails use linear alkylbenzene (LAB) as the primary solvent as it is already the solvent of choice for many liquid scintillator experiments, including SNO+ [82]. All scintillator cocktails were deoxygenated using nitrogen before use to reduce

the quenching caused by oxygenation. Work completed in [20] also measured the relative light yield of the scintillator cocktails, as well as the absorption and emission spectra. These properties are also to be considered for the purpose of a future large-scale neutrino detector as a high measured light yield is desirable.

Acenaphthene ($C_{12}H_{10}$) was selected for use as a primary fluor. It was used at a concentration of 4 g/L in LAB. It was noted that the peak emission wavelength of the solution was ∼335 nm. A wavelength shifting secondary fluor may be required to use acenaphthene in a large scale experiment, as at this wavelength there is non-negligible absorption in LAB [20].

Pyrene ($C_{16}H_{12}$) was also selected as a primary fluor. Pyrene emits scintillation light in one of two states: excimer and monomer. The monomer emission occurs through the usual scintillation process detailed in Section 1.3, where a single molecule de-excites through the emission of a photon. The excimer state, however, is created through the interaction between two pyrene molecules, one excited and one in the ground state [106], as in Equation 2.3.1.

$$M + M^* \rightarrow (MM)^* \rightarrow M + M + \gamma \tag{2.3.1}$$

Where M is a pyrene molecule, * indicates an excited state, and γ is an emitted photon. The resulting dimer state has a lower excitation energy than the monomer state, and as such emits a longer wavelength photon than that released by the monomer. This provided a simple method of studying the two states separately. The monomer state was selected by placing a short pass 400 nm filter in the optics mount at the front of the masking box, and the excimer state was selected by using a long pass 450 nm filter. The excimer state is sensitive to concentration. The pyrene molecules become closer in proximity as the concentration increases, increasing the likelihood of the formation of an excimer state. Pyrene was used at multiple concentrations in LAB, ranging from 1 g/L to 8 g/L in order to investigate this effect. Above 2 g/L the monomer state becomes neg-

ligible and only the excimer state was measured.

9,10-Diphenylanthracene (DPA) ($C_{26}H_{18}$) was selected for measurement as both a primary and secondary fluor. As a primary fluor, a concentration of 5 g/L was used. As a secondary fluor, a concentration of 0.3 g/L was used alongside 2 g/L 2,5-Diphenyloxazole (PPO). While a higher light yield was achieved using DPA as a primary fluor, it was noted that (alongside the high cost of DPA compared to PPO) at high concentrations there may be significant reabsorption due to the relative absorption and emission spectra [20].

1,6-Diphenyl-1,3,5-hexatriene (DPH) ($C_{18}H_{16}$) was selected for used as a secondary fluor. It was used at a concentration of 0.1 g/L alongside 2 g/L PPO. It was noted that the emission spectrum of DPH extends to longer wavelengths than the other fluors, with a significant proportion of the emitted light above 450 nm. At these wavelengths, bialkili photocathodes as used in large PMTs become less efficient, so the potential observed light yield is reduced.

A summary of the selected scintillator cocktails can be found in Table 2.2.

Primary Fluor	Concentration(s) (g/L)	Secondary Fluor	Concentration (g/L)
Acenaphthene	4	—	—
Pyrene	1, 2, 4, 8	—	—
DPA	5	—	—
PPO	2	DPA	0.3
PPO	2	DPH	0.1

Table 2.2: Summary of scintillator cocktails selected for timing characterisation. All fluors were used in a solvent of LAB.

2.4 Results

The time profiles for the different candidate scintillator cocktails are presented, including both the binned ΔT profiles and the best fit response model parameters. A plot showing the difference between the measured data points and the fit curve is also provided. The results of the time parameter measurements are summarised in Tables 2.3 and 2.4.

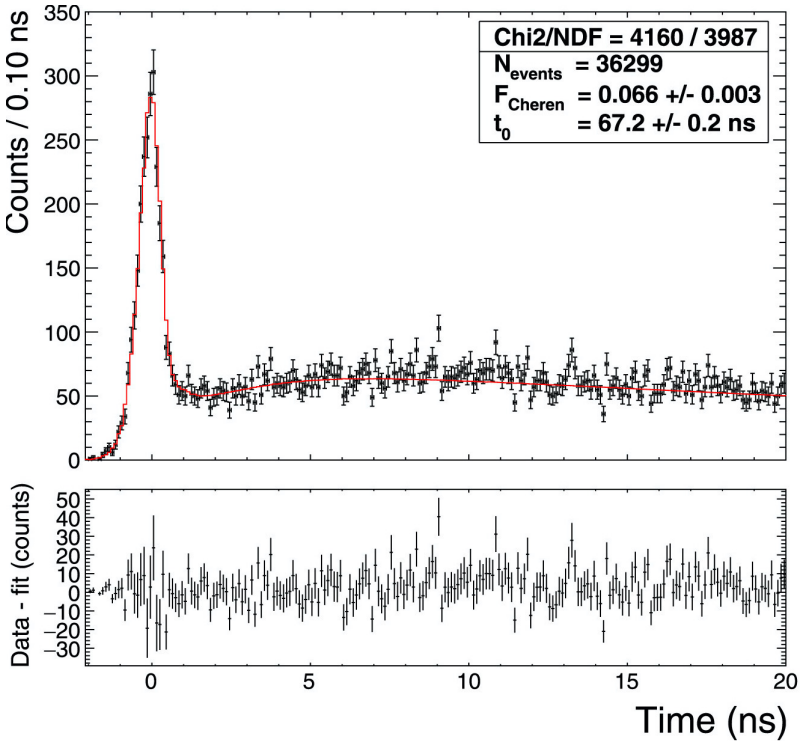
The time profiles of acenaphthene are presented in Figure 2.4. The measured profiles for both the towards and away configurations are shown, with a fit value for the rise time of 2.1 ± 0.2 ns and a fall time of 45.4 ± 0.3 ns. Investigations of acenaphthene in a solvent of cyclohexane have measured a fall time of 46 ns [107], comparable to the value found here. In the towards configuration, a significant Cherenkov peak is visible at $t = 0$. This peak is almost entirely removed in the away configuration, with a F_{Cheren} value consistent with 0 within uncertainty. There is visible directionality within this scintillator cocktail at these time scales.

The time profiles of pyrene are shown in Figure 2.5. The measured fall times were found to be comparable to previous measurements conducting using cyclohexane as a solvent [108]. However, the rise times of the scintillators were found to be different, indicating the effect of solvent on the rising edge of the scintillation emission. Again, there is a clear Cherenkov peak visible in the towards configuration for all pyrene measurements. However, F_{Cheren} is not always consistent with 0 in the away measurements, with the peak still visible. Cherenkov light in this configuration can be due to photon reflections off the vial, or scattering within the scintillator. This is more easily visible in the slowest scintillator cocktails, where even the reflected or scattered Cherenkov signal is not overwhelmed by the scintillation light. At 1 g/L pyrene, the monomer and excimer state are both presented. The excimer state has a very long rise time of 60.1 ± 1.2 ns, leading to extremely low levels of scintillation light contamina-

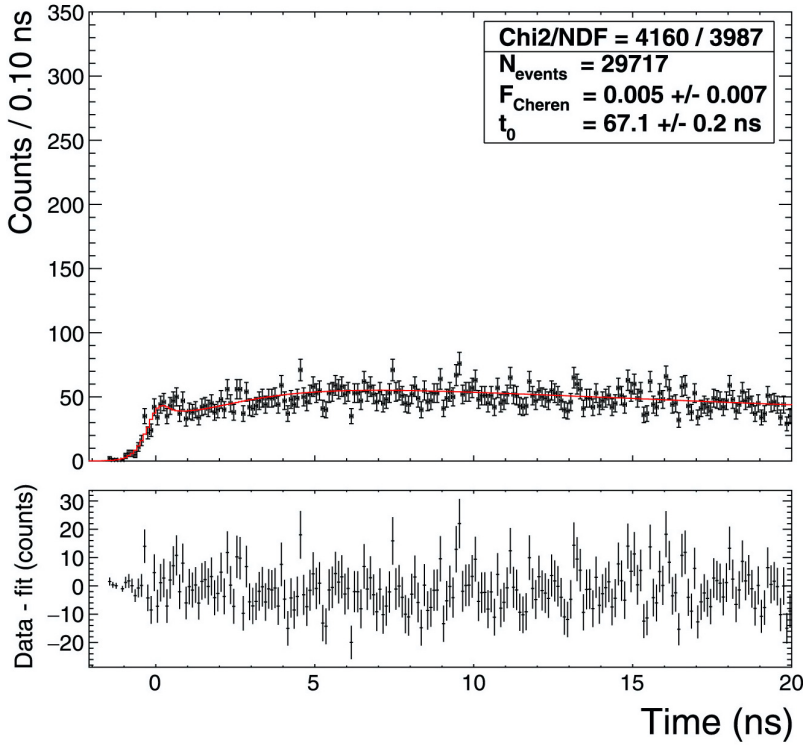
tion in the Cherenkov peak. The excimer emission component is concentration dependent, both in likelihood of emission and in its timing parameters. It can be seen that at 8 g/L pyrene, where the monomer component has become negligible, the scintillation time profile of the excimer state has become faster, with a rise time of 17.6 ± 0.5 ns and a fall time of 50.6 ± 0.6 ns.

Time profiles are presented for DPA as both a primary and secondary fluor in Figure 2.6. While the rise times of the two cocktails are consistent (3.2 ± 0.3 ns and 3.4 ± 0.3 ns for the primary and secondary fluor configurations respectively), the primary fall time of DPA as a primary fluor is slightly longer (13.0 ± 0.2 ns compared to 11.2 ± 0.3 ns). However, the Cherenkov peak is more easily visible when using DPA as a secondary fluor. This is because the light yield of DPA when used as a secondary fluor is $\sim$20% lower than when used as a primary fluor [20], leading to a higher fraction of Cherenkov light and a more visible Cherenkov peak.

Time profiles for DPH as a secondary fluor are presented in Figure 2.7. A rise time of 2.2 ± 0.2 ns and a primary fall time of 11.4 ± 0.4 ns are found. In the towards configuration, there is a visible Cherenkov peak on the rising edge of the scintillator profile.

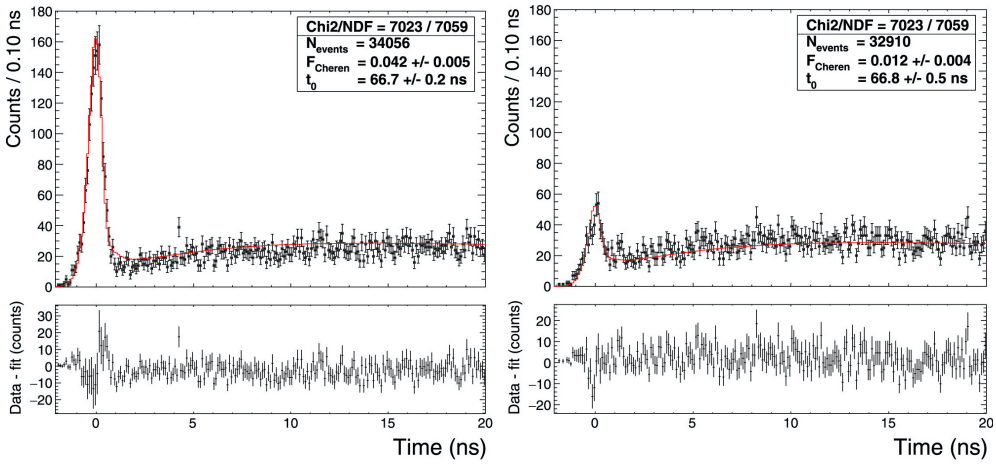


(a) Towards Configuration



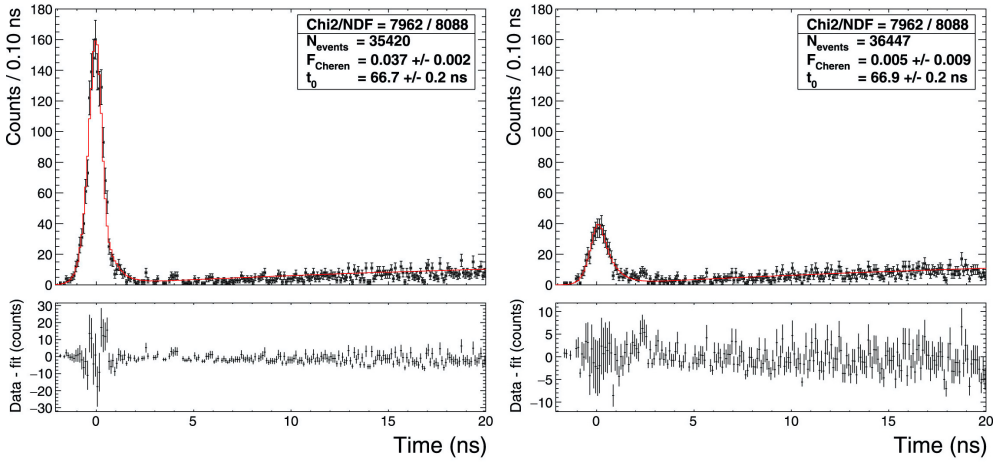
(b) Away Configuration

Figure 2.4: Time profile of acenaphthene at a concentration of 4 g/L in LAB, measured in both the towards (a) and away (b) configurations. The Cherenkov peak can be clearly seen separated from the scintillation light in the towards measurement. Figures originally published in [20].



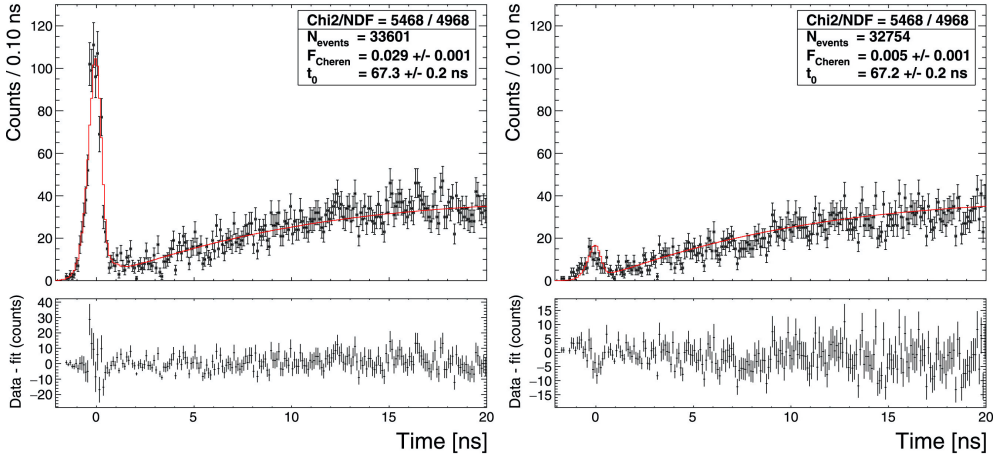
(a) 1 g/L, Monomer, Towards

(b) 1 g/L, Monomer, Away



(c) 1 g/L, Excimer, Towards

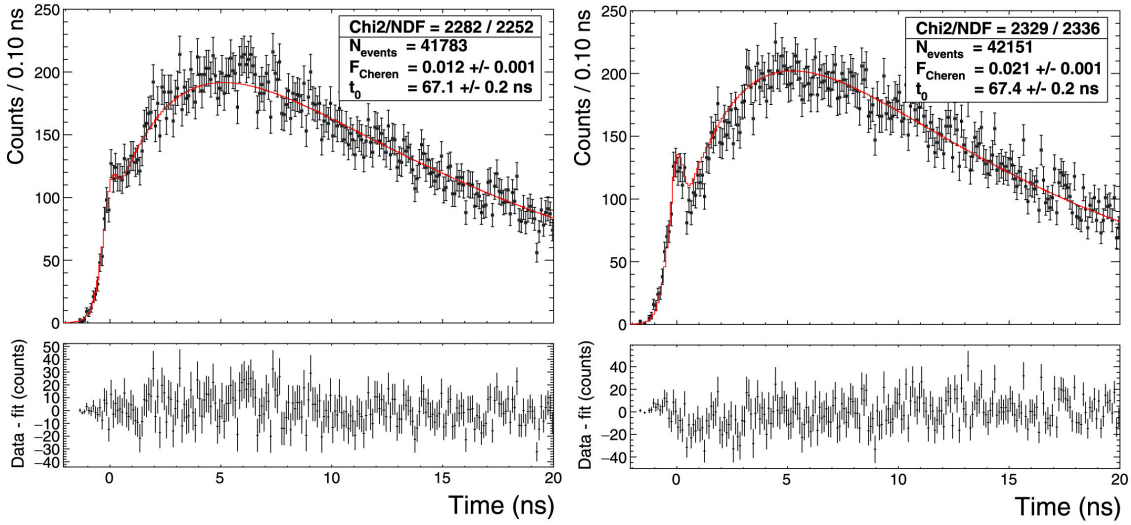
(d) 1 g/L, Excimer, Away



(e) 8 g/L, Excimer, Towards

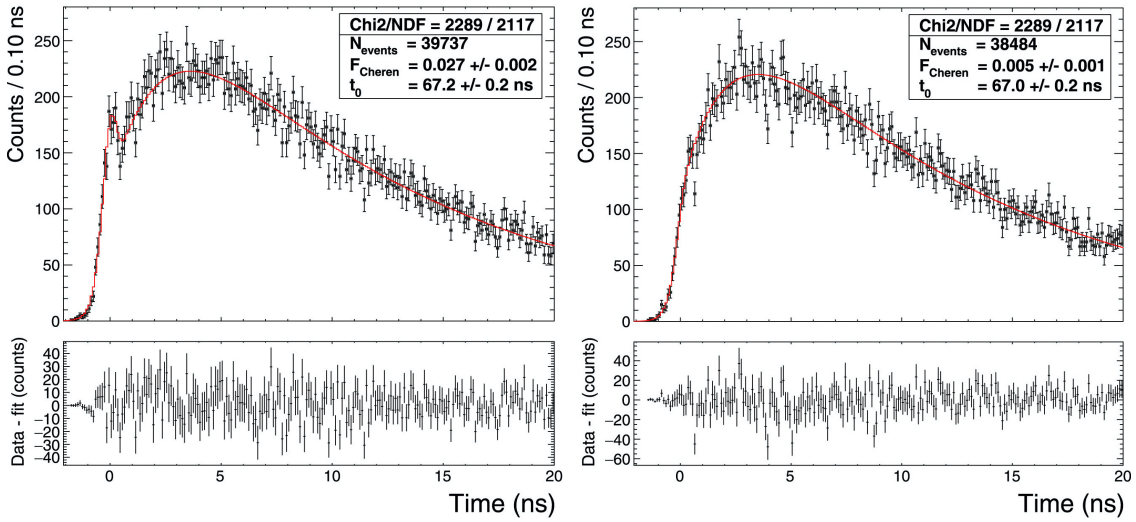
(f) 8 g/L, Excimer, Away

Figure 2.5: Time profiles for pyrene in both the towards (left) and away (right) configurations. Profiles are shown using a concentration of 1 g/L for both the monomer (a,b) and excimer (c,d) states. At 8 g/L only the excimer state is presented (e,f). Cherenkov peaks are clearly separated from the scintillation light in all towards measurements. Small Cherenkov peaks can be seen in the away measurements due to scattering. Figures originally published in [20].



(a) Primary Fluor (5 g/L) (b) Secondary Fluor (0.3 g/L)

Figure 2.6: Time profile of DPA used as both a primary fluor at a concentration of 5 g/L in LAB (a) and a secondary fluor at a concentration of 0.3 g/L, with 2 g/L PPO in LAB (b), measured in the towards configuration. Figures originally published in [20].



(a) Towards Configuration (b) Away Configuration

Figure 2.7: Time profile of DPH used as a secondary fluor at a concentration of 0.1 g/L, with 2 g/L PPO in LAB. Results were measured in both the towards (a) and away (b) configurations. Figures originally published in [20].

Fluor	Conc. (g/L)	τ_r (ns)	τ_1 (ns)	τ_2 (ns)	τ' (ns)
Acenaphthene	4.0	2.1 ± 0.2	45.4 ± 0.3	-	0.9 ± 0.4
Pyrene (excimer)	1.0	60.1 ± 1.2	83.8 ± 1.3	-	0.5 ± 2.6
	2.0	50.9 ± 3.8	65.2 ± 3.6	-	0.5 ± 0.2
	4.0	31.5 ± 1.0	52.6 ± 1.0	-	0.5 ± 0.1
	8.0	17.6 ± 0.5	50.6 ± 0.6	-	2.4 ± 13.5
Pyrene (monomer)	1.0	4.6 ± 1.7	101.2 ± 0.6	-	2.1 ± 7.6
	2.0	4.5 ± 0.8	63.8 ± 0.5	-	7.0 ± 0.8
DPA	5.0	3.2 ± 0.3	13.0 ± 0.2	76.3 ± 18.0	3.2 ± 1.3
DPA + PPO	0.3 + 2.0	3.4 ± 0.3	11.2 ± 0.3	49.0 ± 5.6	2.9 ± 1.4
DPH + PPO	0.1 + 2.0	2.2 ± 0.2	11.4 ± 0.4	67.1 ± 21.0	3.4 ± 1.2

Table 2.3: Best fit time constants for all candidate scintillator cocktails.

Fluor	Conc. (g/L)	A_1 (%)	A_2 (%)	A' (%)
Acenaphthene	4.0	98.6 ± 0.3	-	1.4 ± 0.3
Pyrene (excimer)	1.0	99.2 ± 0.2[1]	-	0.8 ± 0.2
	2.0	99.8 ± 0.1	-	0.2 ± 0.1
	4.0	99.7 ± 0.1	-	0.3 ± 0.1
	8.0	100.0 ± 0.1	-	0.0 ± 0.1
Pyrene (monomer)	1.0	99.0 ± 1.0	-	1.0 ± 1.0
	2.0	96.6 ± 1.9	-	3.4 ± 1.9
DPA	5.0	89.7 ± 2.5	5.7 ± 3.3	4.5 ± 2.1
DPA + PPO	0.3, 2.0	85.3 ± 2.9	10.3 ± 3.6	4.5 ± 2.2
DPH + PPO	0.1, 2.0	85.6 ± 2.3	5.8 ± 3.5	8.6 ± 2.6

[1] In [20] this value is quoted as 0.02. However, this is believed to be an error, and the correct value is given here.

Table 2.4: Best fit scaling constants for all candidate scintillator cocktails.

2.5 Conclusions

An adapted single-photon method for the measurement of time profiles was used to investigate four fluors for the possibility of Cherenkov separation in neutrino detectors. These fluors, measured in a variety of scintillator cocktails in a solvent of LAB, are each characterised as slow due to the relatively long timing constants when compared to scintillator cocktails commonly used in large-scale neutrino detectors. As Cherenkov light is emitted instantaneously, a slow scintillation emission could be separated from Cherenkov light using timing. The investigation of these fluors could therefore be used in the design of future hybrid Cherenkov-scintillator detectors.

In each of the candidate scintillator cocktails, there was a visible early Cherenkov peak when the time profile was measured using 0.1 ns bins. This was confirmed by conducting measurements with a source pointed both towards and away from the measurement PMT, allowing a comparison of Cherenkov light present in both the forward and backward directions.

Large-scale experiments include PMTs with significantly wider timing response curves than those used in this table top measurement, often on the order of several ns. This must be considered alongside the effect of the dispersion that occurs across the large distances in a neutrino experiment. The timing constants found here, which are on the order of several tens of ns, indicate there should still be a considerable separation power between the Cherenkov and scintillation signals in a large-scale experiment.

Other considerations must also be taken into account when designing a hybrid detector using slow scintillators. The slower scintillation profile will cause a loss in the position-time vertex resolution of a large scale scintillator experiment. However, the performance should still remain more precise than that of a Cherenkov detector. Absorption profiles of the slow scintillators must be accounted

for, with the possibility of needing to add a further fluor as a wavelength shifter in order to ensure a sufficient light yield for high-precision energy measurements. Additionally, trigger window length must be tuned in order to detect the maximum amount of scintillation light possible, while minimising the possibility of multiple events occurring in-window.

Further investigation has been conducted to quantify the directionality achievable in a large scale experiment using acenaphthene [101], involving the simulation of a SNO+-like detector containing high quantum efficiency PMTs and the use of a simultaneous time-position-direction maximum likelihood method. This study concluded directional information from slow scintillators could lead to an improvement in background rejection of solar neutrinos by a factor of ten in a $0\nu\beta\beta$ search, leading to an improvement of sensitivity (scaled as $S/\sqrt{(B)}$) of a factor of 1.6. Additionally, the CNO solar neutrino flux rate could be constrained to a 10% precision within $\sim$3 kiloton-years, assuming background rates comparable to those of the Borexino detector. The extraction of directional information from slow scintillators offers a powerful background rejection tool for solar neutrinos, while maintaining high performance of energy reconstruction needed for low energy neutrino studies.

Chapter 3

The SNO+ Experiment

"Oh no, not again."

- The Hitchhiker's Guide to the Galaxy, Douglas Adams

SNO+ is a multipurpose neutrino detector situated at SNOLAB in Ontario, Canada [109]. The detector utilises large parts of the infrastructure of the SNO experiment, a heavy-water detector that observed neutrino oscillations from solar neutrinos [9, 10]. SNO+ introduces several upgrades and changes to the detector, most notably the use of liquid scintillator as the target medium.

The main physics goal of SNO+ is the search for $0\nu\beta\beta$ using the isotope ^{130}Te, with additional studies into solar neutrinos, reactor anti-neutrinos, supernova neutrinos, geo-neutrinos, dark matter, and more [109,110]. The detector benefits from very low cosmic muon rates ($0.289 \pm 0.009\,\mathrm{m}^{-2}\,\mathrm{d}^{-1}$ [109]) — due to its location 2 km underground — as well as its large size and and potential for loading increasing concentrations of ^{130}Te for higher exposure.

This chapter offers an overview of the SNO+ detector. The hardware, geometry and data acquisition system of the SNO+ experiment are described in Section 3.1. The experimental phases of SNO+ are explained in Section 3.2, with details given for the data collection periods for this thesis. Section 3.3 describes the simulation of SNO+. Section 3.4 introduces the methods used to reconstruct the position-time vertex of events in SNO+ and the use of PMT hit information for the estimation of energy.

3.1 The SNO+ Detector

SNO+ is located within the 37 200 m^3 class-2000 clean room at SNOLAB [111]. A drawing of the SNO+ detector can be seen in Figure 3.1.

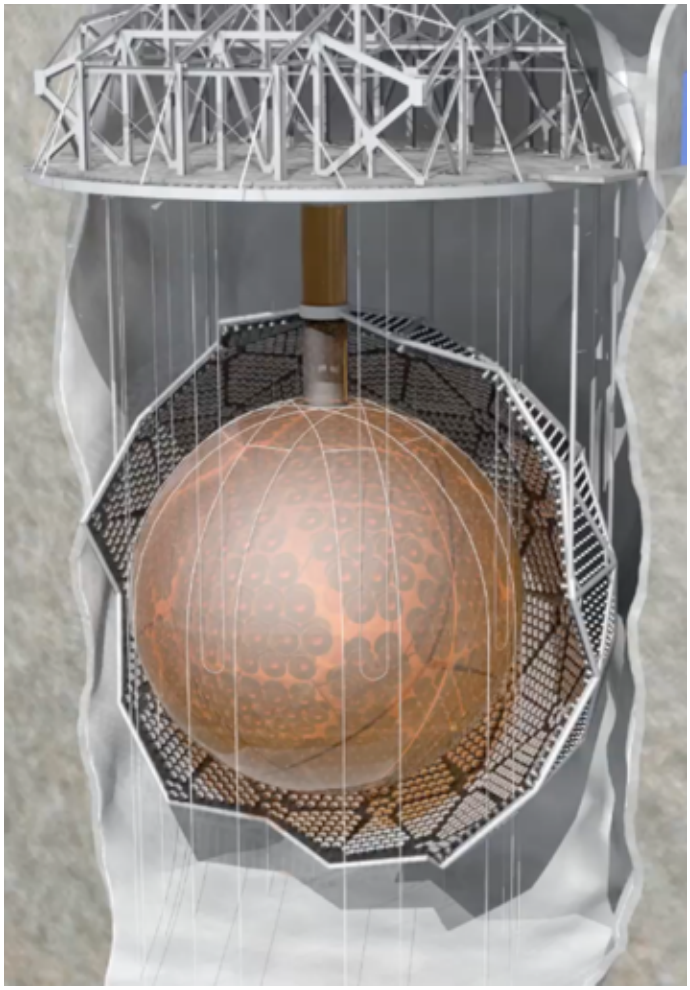


Figure 3.1: A simplified drawing of the SNO+ detector. Figure taken from [109].

The detector is housed within a 30 m tall cavity, originally excavated for the SNO experiment. The cavity is filled with 7000 t ultra-pure water (UPW) which acts as shielding from potential radioactive backgrounds in the surrounding rock, as well as part of an external muon veto system.

The target volume of the detector is contained within a 6 m radius spherical Acrylic Vessel (AV), with a thickness of 5.5 cm. This is shown in orange in Figure 3.1. A 7 m high cylindrical neck extends up from the top of the AV, through

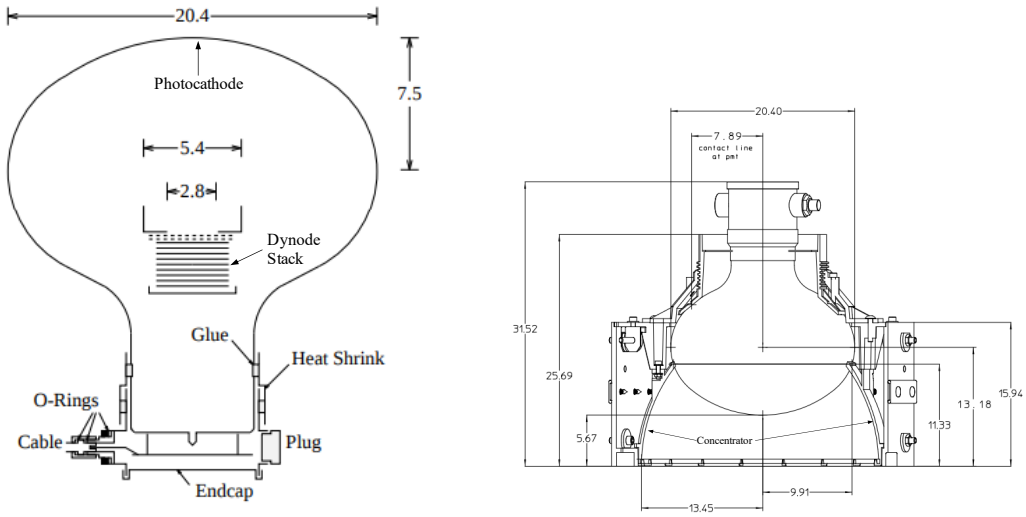
which the liquid target medium can be loaded. The AV is held in place by a series of Tensylon ropes. In the original SNO detector, the AV was filled with heavy water (D_2O), requiring hold-up ropes to keep the AV suspended in place. These ropes were attached to the AV through grooved plates around the equator of the detector. However, in SNO+, the target mass is an LAB-based liquid scintillator with a density less than that of water. This meant that the upgrade to SNO+ required the additional installation of hold-down ropes, formed in a net around the neck of the AV and attached to the bottom of the cavity. The target medium housed within the AV has undergone multiple commissioning and experimental phases as described in Section 3.2.

The PMT Support Structure (PSUP) is a 92-sided geodesic polygon with an average radius of $\sim$8.35 m which surrounds the AV. The PSUP holds 9362 inward-facing PMTs, each mounted with a concentrator to create a 54% effective coverage. Additionally, 91 PMTs are mounted externally to the PSUP, known as the the Outward Looking PMTs (OWLs). These PMTs are used for a muon veto, as they detect Cherenkov photons emitted by the muon as it passes through the external water before entering the target mass of the detector. The target medium is shielded from the radioactivity of the PMTs by the water buffer between the AV and the PSUP.

Both the water in the cavity and the target medium in the AV are protected from radioactive contamination through cover gas systems. High purity nitrogen gas is circulated through the area above the cavity water at a rate of 5 L/min. In the area of the AV neck above the target medium, high purity nitrogen gas is held in a sealed system, with the concentration of radon within the gas continuously monitored.

3.1.1 Photomultiplier tubes

SNO+ uses 8-inch Hamamatsu R1408 PMTs, each equipped with a 27 cm diameter truncated Winston cone concentrator [112]. Schematics of these can be seen in Figure 3.2.



(a) (b)

Figure 3.2: Schematic drawings of a Hamamatsu R1408 PMT, as used in SNO+, with and without a truncated Winston cone concentrator. Round PMT glass at the top of the PMT holds the photocathode. Dimensions are in cm. Figures adapted from [113].

When a photon hits the photocathode on the front of the PMT, a photoelectron is released. The internal vacuum of the PMT is held under an electric field. This accelerates electrons through a dynode stack, causing the electrons to multiply as they cascade through multiple collisions. The resulting influx of electrons causes a measurable signal on the anode, housed in the base of the PMT.

The time taken for the electrons to transverse the PMT is known as the "transit time". The distribution of transit time can be seen in Figure 3.3, as simulated in the SNO+ experiment. This distribution was originally measured by the SNO collaboration, with tuning of late pulsing done by the SNO+ col-

laboration. The peak at 0 ns corresponds to the typical transit path of an electron cascading through the dynode stack. A Gaussian fit of this peak returns a standard deviation of 1.577 ns. The early peak at ~ -18 ns is caused by photons passing through the photocathode and instead hitting the dynode, known as "pre-pulsing". The later pulses at 10 ns and 40 ns are caused by the photoelectron backscattering off the dynode stack. Either the scattering is elastic, and the electron takes time to drift back to the dynode and start the cascade, or the scattering is inelastic, causing two cascades.

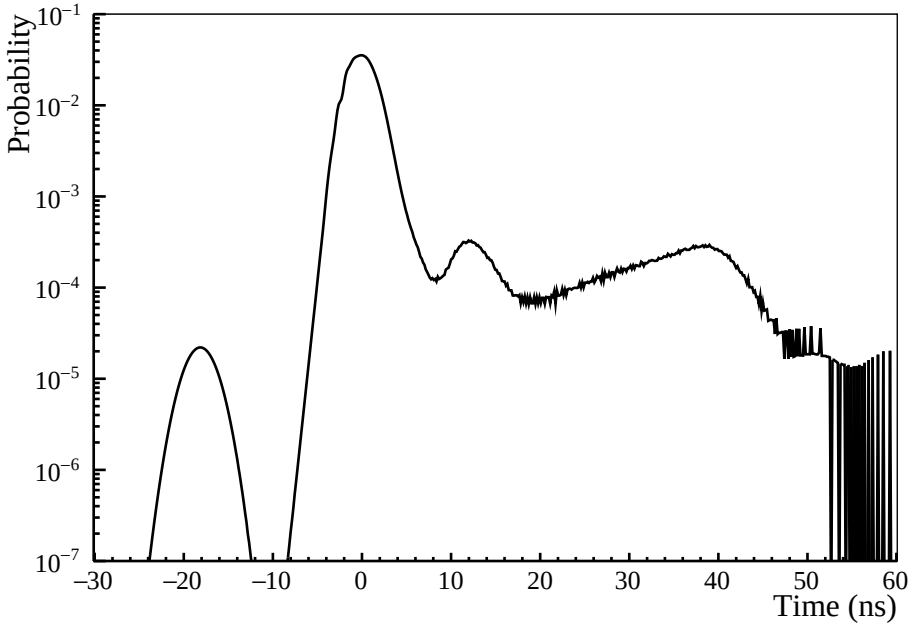


Figure 3.3: Probability distribution of the transit time as simulated in SNO+ for the Hamamatsu R1408 PMT, measured by the SNO collaboration and tuned by the SNO+ collaboration.

The response efficiency of PMTs can be separated into two components. The first is the quantum efficiency, which is the percentage of incident photons that create a photoelectron at the photocathode. The second is the collection efficiency, which is the percentage of photoelectrons which reach the first dynode to cause a cascade. The product of these two efficiencies define the total efficiency of the PMT. The efficiency as a function of wavelength for the Hamamatsu R1408 PMT can be seen in Figure 3.4.

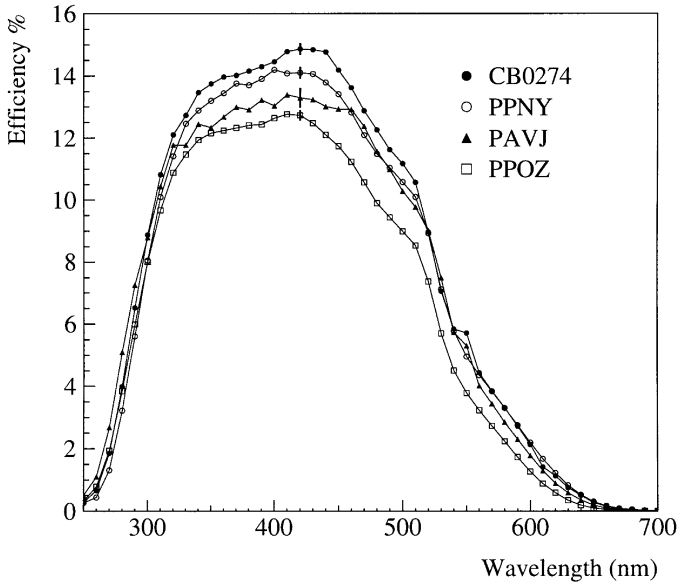


Figure 3.4: Efficiency of the Hamamatsu R1408 PMT as a function of wavelength, measured for four example PMTs. Figure taken from [114].

3.1.2 Data Readout and Acquisition

The majority of the Data Acquisition (DAQ) hardware is housed on the deck above the SNO+ detector. This hardware allows information about detected photons to be read out as data files by analysers. This section provides a brief overview of DAQ hardware and further details can be found in [113, 109]

Once a PMT has been hit by a photon and the anode has collected the electron cascade signal, the pulse is transmitted to a Front End Card (FEC). If the signal pulse is larger than the FEC trigger threshold, the PMT is counted as "hit", and the FEC sends a trigger pulse to the Master Trigger Card (MTC). If the MTC receives a sufficient number of trigger pulses in a given time window, a Global Trigger (GT) is issued. The GT is sent back to the FECs, which calculate the time elapsed since the initial trigger and the charged collected by the PMT. A 400 ns trigger window is set, keeping all data collected in the FECs for 180 ns before and 220 ns after the GT. The GT is given an identifying number (GTID) and the hit time and charge information is transmitted to computers for the event to be built and reconstructed, as described in Section 3.4.

Data is stored in "runs" of up to one hour. This allows for discrete blocks of data for the purpose of data processing and data quality checks. Runs are denoted as set "types", for example calibration, physics or maintenance, and provide a simple method of tracking detector status through time.

3.2 Experimental Phases of SNO+

The main physics goal of SNO+ is the search for $0\nu\beta\beta$, which requires a target medium of liquid scintillator loaded with the isotope ^{130}Te. However, several phases of commissioning are required in order to achieve this final cocktail [109]. Each phase also created the possibility for alternative physics analyses, as well as detector calibration. Therefore, stable data acquisition phases were defined, with each phase identified by the target medium in the detector.

3.2.1 The Water Phase

The first phase of SNO+ contained a target of 905 t of UPW. The use of UPW in the AV reduced the contamination of radon into the detector from the air, mitigating future background once scintillator was loaded. This also allowed the detector to operate as a Cherenkov detector, and a data acquisition period was defined from May 2017 to July 2019.

During this time, multiple physics searches were carried out, including the detection of solar ^{8}B neutrinos [115], a search for invisible nucleon decay [116], a measurement of neutron-proton capture [117], and the first evidence of antineutrinos from nuclear reactors in a water Cherenkov detector [118]. Additionally, calibration tasks were undertaken in order to tune simulations of the detector, including the optical parameters of the detector materials and the responses of the PMTs [119]. Measurements were also conducted of the background rates of detector components for use in future physics searches, and an improved cover gas system was developed for background reduction.

3.2.2 The Partial-Fill Phase

The LS used in SNO+ is PPO as a primary fluor in a solvent of LAB. The method of scintillator deployment involved the addition of LS to the top of the detector, while UPW was removed from the bottom. This was possible due to the difference in density of the two liquids (with LAB having a density of $0.856\,\mathrm{g/cm^3}$) and the immiscibility of LAB in water, leading to an interface between the top LAB layer and the bottom UPW layer. This interface gradually descended through the detector, and was visible through photographs taken by cameras mounted on the PSUP, as seen in Figure 3.5.

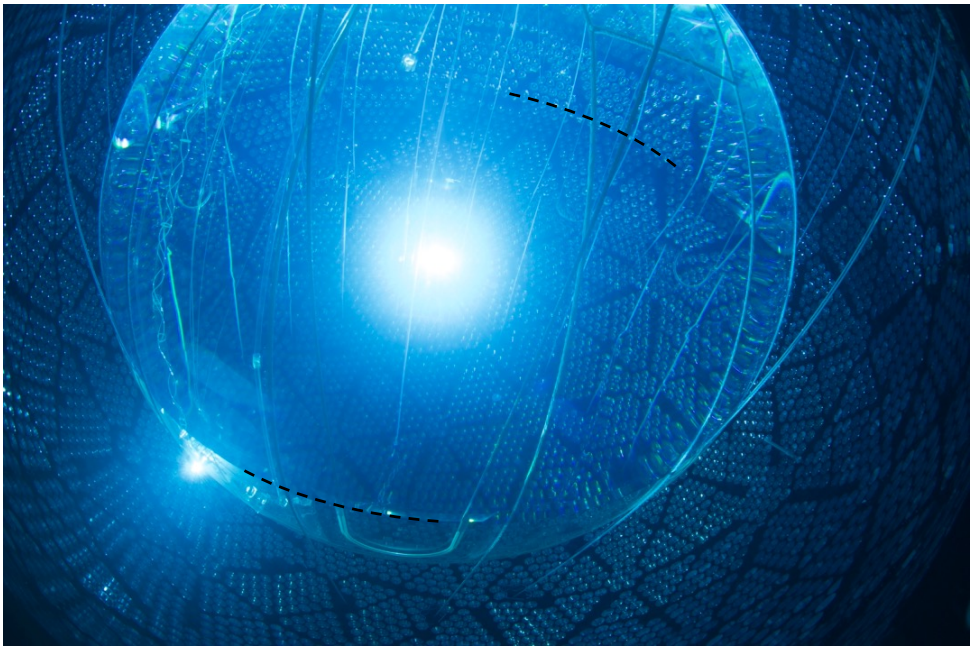


Figure 3.5: Photograph taken of the SNO+ detector during the partial-fill phase, using a camera mounted on the PSUP. Sections of the LS-UPW interface are indicted by black dashed lines.

Due to the exceptional circumstances of the COVID-19 lockdown, the process of filling the detector with LS was paused. This meant that SNO+ underwent a stable period of data taking in which the detector contained 365 t of LS, with the interface occurring $\sim$75 cm above the equator of the AV. This phase occurred from March to October 2020.

The method of scintillator deployment also involved the gradual addition of PPO into the scintillator cocktail, with the first stages of LAB filling containing a lower concentration than the target of 2.2 g/L. During the period of the partial-fill phase, the scintillator cocktail contained 0.6 g/L PPO in the LAB.

During this period, background measurements and calibration tasks continued, now with the ability to assess the optical parameters of the scintillator. The light yield was found to be ∼300 NHit/MeV using calibration of known ^{214}Bi-^{214}Po (BiPo214) decays. BiPo214 events are an internal background of the detector. They can be identified due to the short half-life of ^{214}Po, which creates two coincident events in the detector of known energies and close physical proximity [120]. The scintillator timing parameters were also measured in-situ by identifying BiPo214 background events and then iteratively tuning timing parameters in simulation until the results of Monte Carlo (MC) simulation matched those in data [120]. The scintillation profile was modelled as in Equation 3.2.1.

$$f_s(t) = \sum_{i=1}^{n} \left(A_i \frac{e^{-\frac{t}{\tau_i}} - e^{-\frac{t}{\tau_r}}}{\tau_i - \tau_r} \right) \tag{3.2.1}$$

The 0.6 g/L cocktail was found to have three exponential components ($n = 3$). The rise time (τ_r) was found to be 0.8 ns, and the remaining tuned parameters (A_i, τ_i) can be found in Table 3.1.

i	1	2	3
τ_i (ns)	13.5	23	98.5
A_i	0.55	0.335	0.115

Table 3.1: Tuned timing parameters of the SNO+ 0.6 g/L LABPPO scintillator cocktail.

Additionally, initial physics searches for solar neutrinos and reactor antineutrinos were completed during this phase.

3.2.3 The Full-Fill $0.6\,\mathrm{g/L}$ Phase

Deployment of the scintillator resumed in October 2020. In April 2021, the LAB fill of the AV was completed. The LS target remained at the lower concentration of $0.6\,\mathrm{g/L}$ PPO, with plans to add the remaining PPO after a short stable period. Data was collected in this configuration from April to June 2021. The light yield and timing parameters for this phase were verified to be the same as in the partial-fill phase. Further optical calibrations and background radioactivity measurements were completed in this period.

3.2.4 The Scintillator Phase

The final stage of LS deployment increased the concentration of PPO until the target concentration of $2.2\,\mathrm{g/L}$ was reached. This was completed in April 2022, and as such began the official scintillator phase of the SNO+ experiment. At the time of writing, this is the current phase.

The scintillator phase allows for crucial detector calibrations and background measurements. Background radioactivity, both internal and external to the AV, must be closely constrained for a sensitive $0\nu\beta\beta$ search to be conducted, so these studies are conducted before the addition of an isotope. This phase also offers the opportunity for many ongoing physics analyses, including measurements of the solar neutrino flux, the measurements of Δm^2_{21} and θ_{21} from the detection of reactor anti-neutrinos, and the potential for the observation of a supernova.

Once again, the timing parameters of the scintillation emission were tuned iteratively by comparing MC simulation to tagged BiPo214 events in data. The $2.2\,\mathrm{g/L}$ cocktail was found to have three exponential components (n=3). The rise time (τ_r) was found to be 0.85 ns, and the remaining tuned parameters can be found in Table 3.2. A comparison of the tuned timing profiles in both PPO concentrations can be seen in Figure 3.6.

i	1	2	3
τ_i (ns)	5.0	24.46	399
A_i	0.656	0.252	0.092

Table 3.2: Tuned timing parameters of the SNO+ 2.2 g/L LABPPO scintillator cocktail.

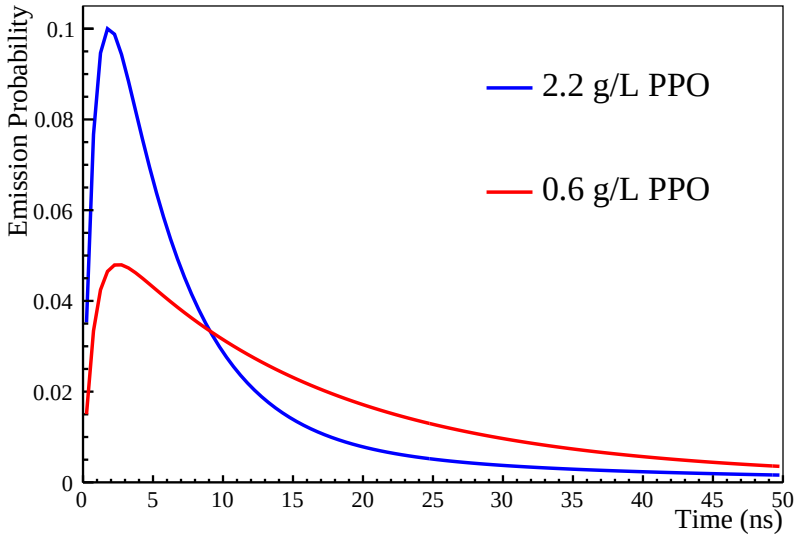


Figure 3.6: Comparison of the tuned time profiles of 0.6 g/L and 2.2 g/L PPO scintillator cocktails. The 0.6 g/L scintillator has a slower profile than the higher concentration.

3.2.5 The Tellurium Phase

In order to achieve the main physics goal of SNO+ — the search for $0\nu\beta\beta$ — the SNO+ experiment will need to be loaded with a $2\nu\beta\beta$ source. ^{130}Te was chosen for SNO+ due to its good optical qualities in LAB, high natural abundance, and long $2\nu\beta\beta$ half life [109]. The addition of tellurium does decrease the light output of LABPPO, although methods of reducing this effect are being developed [79,121]. These include the addition of the stabiliser N,N-Dimethyldodecylamine (DDA) and the secondary fluor 1,4-bis(2-methylstyryl)benzene (bisMSB). Initial loading will go to 0.5% by mass of natural tellurium, although there is a possibility of increased loading in future stages.

3.3 Software and Simulation

The primary software used for the SNO+ experiment is an adapted version of the Reactor Analysis Tool (RAT) [122], originally intended for use in the Braidwood Experiment [123]. The software has been developed for specific use in the SNO+ experiment [109] for both the MC simulation of physics events in the detector and the analysis of data. RAT is written in C++ and uses ROOT [124] for data analysis, as well as storing data in a custom ROOT file named RATDS (used for both data and simulated MC). RAT uses GEANT4 [125, 126] for simulation of the detector, including detailed geometry adjustable to the various phases of detector operation. The GLG4Sim package [127] is used for the generation of Cherenkov and scintillation photons within the simulation. Parameters for both simulation and data processing are stored in the dynamic database RATDB, allowing for values to be updated on a run-by-run basis. This can be used to create MC simulation with values accurate to reality for a given run number, including detector conditions such as which channels are off and trigger statuses.

Event simulation in RAT starts with the three step generation of an initial particle: kinematics of the physical interaction (providing an initial energy and momentum), a position, and a time. High level event generators have been developed for the SNO+ experiment, combining all three steps into a single generator for a known signal or background in the detector. This includes $0\nu\beta\beta$, solar neutrino interactions, and particular radioactive decays. Once the initial event has been generated, GEANT4 is used to propagate the particles throughout the detector, including the generation of photons that are then "detected" at the simulated PMTs. Simulated electronics and event builders then create a RATDS file that can be run through reconstruction and analyses in the same way as a data file, while additionally storing the MC truth information.

3.4 Event Reconstruction in SNO+

The output data from the SNO+ detector for a given event contains two main pieces of information: PMTs that have been hit, and the times of those hits. From this information, physical event-level quantities can be reconstructed for use in physics analyses. This section describes the algorithm used to reconstruct the position-time vertex developed by the SNO+ collaboration. The reconstructed position-time vertex will then be used in the direction reconstruction algorithms developed by the author and described in Chapter 4. The NHit parameter is also described, along with its correlation to energy and use in the directionality study in this thesis.

3.4.1 Position-Time Vertex

Within the SNO+ detector, the majority of events are considered to be single-site, consisting of a single position-time vertex (with the exception of high energy muons that traverse the AV). Some types of events within the detector would be more accurately considered multi-site. For example, an emitted γ can scatter at a different location after an initial radioactive decay. Algorithms that can distinguish between a true single-site event and a multi-site event have be studied [128]. However, the signal considered for the purpose of this thesis is neutrino-electron elastic scattering, a true single-site event. For this reason, only the reconstruction of single-site position-time vertices is described here.

The reconstruction of the position-time vertex relies on a quantity known as the time residual. The time residual is defined as:

$$t_{res} = t_{hit} - t_{event} - t_{flight} \tag{3.4.1}$$

where t_{hit} is the hit time of the PMT, t_{event} is the time of the event (found through either reconstruction or MC truth data), and t_{flight} is the time of flight for the

photon between the event position and the PMT. Time of flight is calculated assuming straight line paths, and is found by:

$$t_{flight} = \frac{d_w}{v_w} + \frac{d_a}{v_a} + \frac{d_s}{v_s} \tag{3.4.2}$$

where $d_{w,a,s}$ is the distance travelled in water, acrylic or scintillator respectively, and $v_{w,a,s}$ is the group velocity of light in that medium (approximated for 400 nm photons). The time residual is therefore an estimation of the emission timing spectrum of an event. Details of time residual parameter are discussed further in Chapter 4, including small variations dependent on position. For the purpose of position-time reconstruction, the variations in the time residual distribution due to event position are not considered.

A probability density function (PDF) of t_{res} can be generated using one of two methods. The first method is used in the "multiPath" reconstruction algorithm. The PDF is formed from a table-top measurement of the time profile of the scintillator, conducted using a single photon coincidence method [129]. The time profile is then convolved with the impulse response function of the detector as a whole, tuned to data using an ^{16}N source in the water phase. This method does not account for the changes in time response due to reemission and the large scale of the detector. However, it also does not rely on the accurate tuning of scintillator parameters in the simulation. This PDF is used in partialFitter, the reconstruction algorithm used as standard for all data and MC simulation in the partial-fill phase and the full-fill 0.6 g/L phase, and is used for all position reconstruction in the direction reconstruction analysis detailed in Chapter 4.

The second method to generate the PDF is used in the "multiPDF" reconstruction algorithm. The PDF is generated using a large number of simulated electrons. A t_{res} distribution is then calculated from the results of the simulations, using a maximum event radius of 4 m. This method accounts for reemission as modelled in the simulation, but relies heavily on accurate modelling of the

scintillator time profile and optical parameters. This PDF is used in scintFitter, the algorithm used as standard for all data and MC simulation in the scintillator phase. MultiPDF is used for a seed position in the combined direction-position reconstruction and for the modern PMT studies conducted in Chapter 5.

For either PDF, the reconstruction of the position-time vertex is performed using a maximum-likelihood search to find the best fit position and time. The likelihood of a proposed position-time vertex ($\vec{r}_{event}, t_{event}$) is constructed as shown in Equation 3.4.3.

$$\log(\mathcal{L}(\vec{r}_{event}, t_{event})) = \sum_{i}^{N} \log(p(t^{i}_{res})) \tag{3.4.3}$$

The time residual of a given hit (t^{i}_{res}) is calculated for the proposed event position and time, and the probability (p) of that time residual is found from the relevant PDF. The log-likelihood is then found from the sum of the log-probabilities of each PMT hit, The position-time vertex that corresponds to the maximum likelihood (found using the Powell optimisation method) is then returned as the reconstructed position and time.

The performance of position-time reconstruction in simulation using both multiPath and multiPDF can be seen in Figures 3.7 and 3.8, using RAT version 7.0.5. Simulations of electrons with isotropic directions were run in a perfect-state full-fill detector containing 0.6 g/L PPO. To calculate the bias and resolution at a given energy and radius, histogram distributions of $x_{recon} - x_{true}$ were created from the simulation, where x is the relevant parameter, *recon* indicates the reconstructed value and *true* indicates the MC truth value. A Gaussian distribution was then fit to each of these histograms. The bias was defined as the mean of the Gaussian distribution, and the resolution was defined as the standard deviation.

In order to represent the reconstruction performance as a function of radius, electrons were simulated in shells of width 400 mm. Electrons with an energy

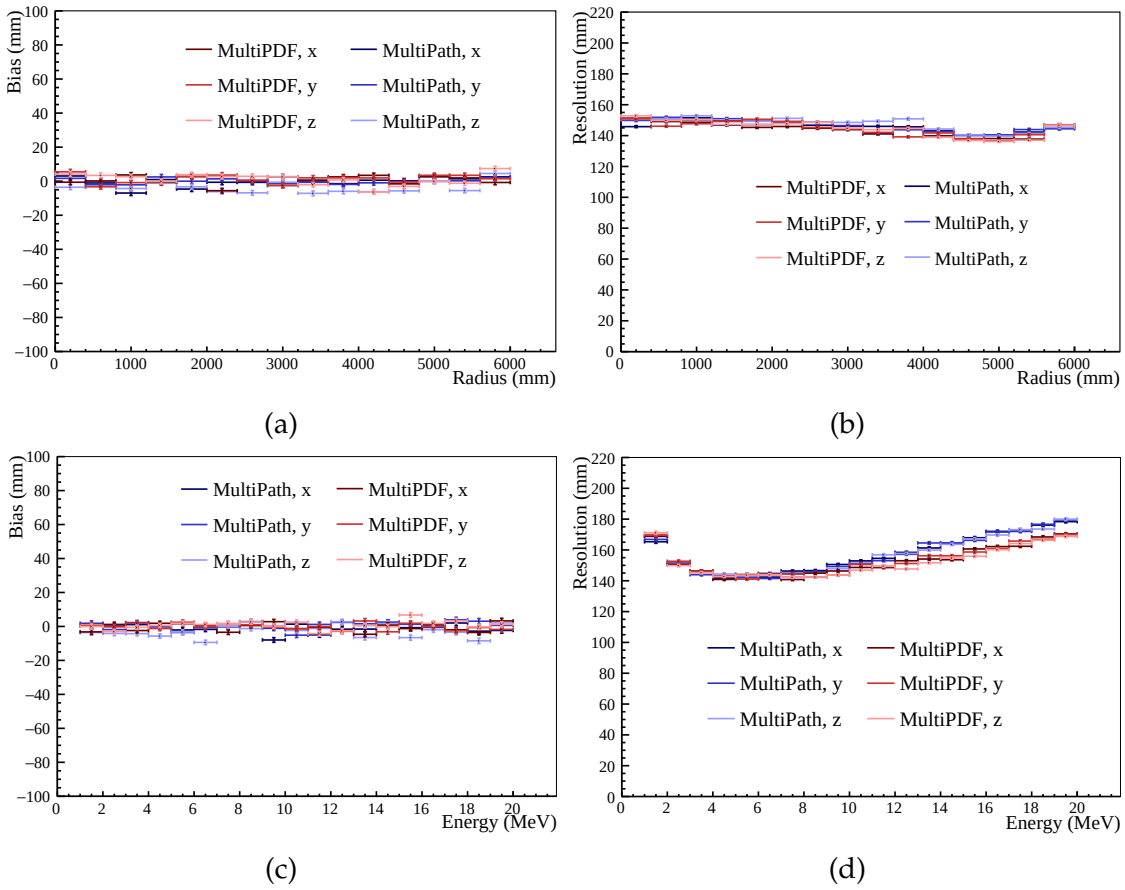


Figure 3.7: Performance of position reconstruction in SNO+ simulation, using both the MultiPath and MultiPDF methods. Results are displayed for simulations of a 0.6 g/L PPO scintillator cocktail. Each point represents a Gaussian fit to $x_{i,recon} - x_{i,true}$ distributions, where x_i is the relevant position parameter.

of 6 MeV were used to evaluate position-time reconstruction. This is because the directionality study conducted in this thesis uses electrons with energies >5 MeV. Analyses in SNO+ generally use a maximum radius cut of 5.5 m. This is both to reduce external backgrounds and to avoid optical effects near the AV, where the straight line approximations or light paths are no longer valid. In order to represent the reconstruction performance as a function of energy, electrons were simulated across the range 1–20 MeV throughout the volume of the detector, out to a radius of 5.5 m to provide an equivalent performance for physics analyses.

When investigating position reconstruction as a function of radius at 6 MeV,

resolutions of $\sim$150 mm are seen in all directions with variation across the detector on the order of $\sim$10 mm. Additionally, when examining the resolution as a function of energy, there is an optimal minimum at $\sim$6 MeV. This is because there are two competing effects that contribute to the possible precision. The PDF created for position-time reconstruction uses 3 MeV electrons, chosen to be close to the $0\nu\beta\beta$ region of interest, which should lead to more accurate position reconstruction at this energy. However, more photons available at higher energies, which allows for a more precise reconstruction. This creates two competing effects, resulting in the minimum being at a higher energy than expected from the PDF. For an energy range of 1–20 MeV , position resolutions range between 140–180 mm in all directions. Within the scale of the resolution, there are negligible biases to position reconstruction, generally $<$10 mm, with no obvious trends in either energy or radius.

However, clear biases are seen in the reconstruction of time, with the two reconstruction methods demonstrating biases in opposite directions. There are clear negative trends in the bias of time reconstruction as a function of both energy and radius. The time resolution at 6 MeV has a value of $\sim$0.25 ns for radii $<$5 m, but the biases reach up to 1 ns.These biases are due to arbitrary time offsets included in the PDFs created for both reconstruction methods. Time offsets are intended to account for electronic response times of the detector.

The reconstructed position-time vertex is required for the reconstruction of direction described in Chapter 4. Therefore, understanding the performance of such reconstruction allows for estimation of the impact position-time reconstruction has on the ability to reconstruct direction. The resolution of position leads to an uncertainty of photon travel times $<$1 ns. The PDF used for the reconstruction of direction uses bins of width 1 ns, so the impact of position resolution is considered to be subdominant. Similarly, the resolution of time reconstruction is not considered to be a significant factor in the reconstruction of direction. The

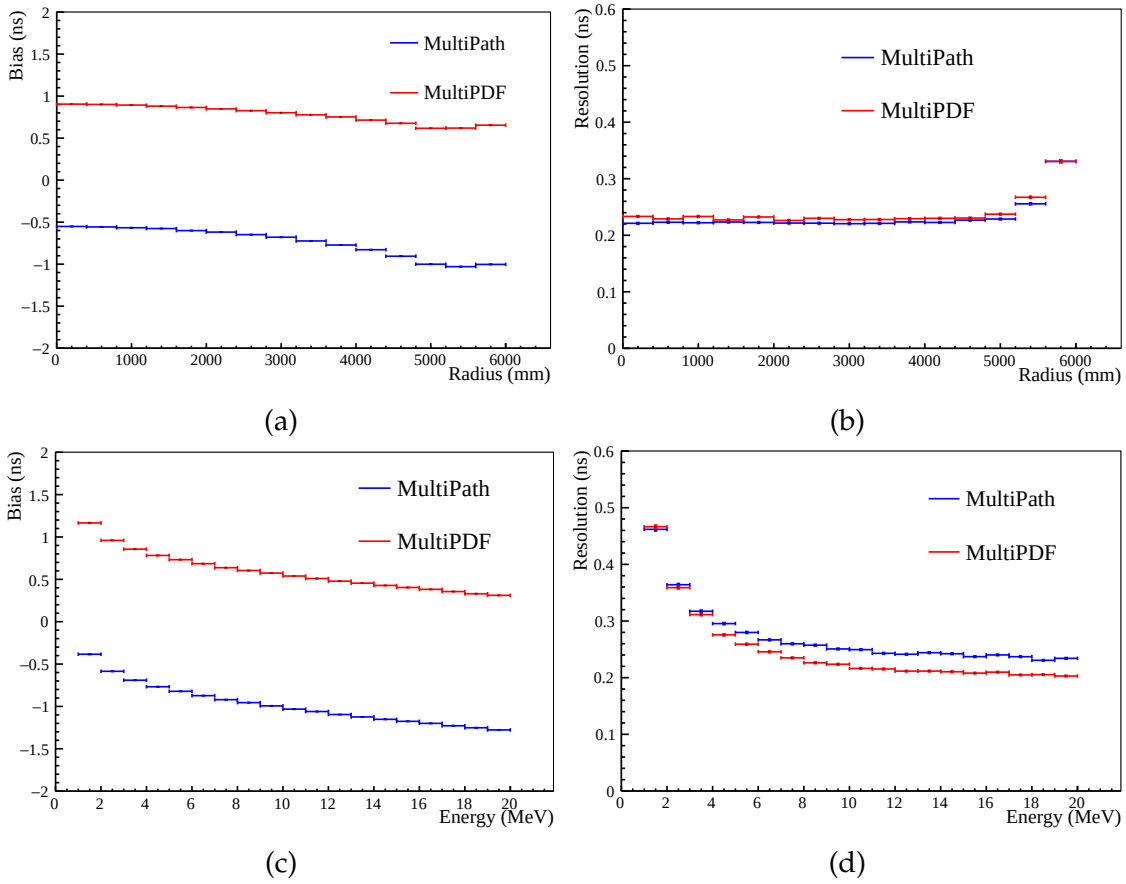


Figure 3.8: Performance of time reconstruction in SNO+ simulation, using both the MultiPath and MultiPDF methods. Results are displayed for simulations of a 0.6 g/L PPO scintillator cocktail. Each point represents a Gaussian fit to $t_{recon} - t_{true}$ distributions, where t is the initial time of the electron emission.

bias of time reconstruction is accounted for by ensuring that the same position-time reconstruction algorithm is used for both the creation of the PDF and the reconstruction of events in data. This ensures that the same arbitrary offset is applied, largely removing the effect of this bias. There will be small changes in the bias dependent on energy and radius, but for a data set with energies >5 MeV and radii <5.5 m, these are considered negligible. Further discussions of position-time reconstruction and its effect on directionality studies are found in Section 4.2

3.4.2 Energy and NHit

Reconstruction of energy in the SNO+ detector uses the relationship between energy loss of a particle and emitted photons in a scintillator described by Equation 1.3.4. However, not every photon emitted by the scintillator will be detected in the PMTs. As such, a parameter called NHit is used to quantify the scintillation emission, the number of PMTs that are hit in a given trigger window. PMTs that are not calibrated or experience electronic crosstalk are removed from the total count of hits, leading to the parameter also being known as "NHitClean". The relationship between energy and NHit can be seen in Figure 3.9. This plot was generated using simulations of mono-energetic electrons at the centre of the detector in 0.6 g/L PPO.

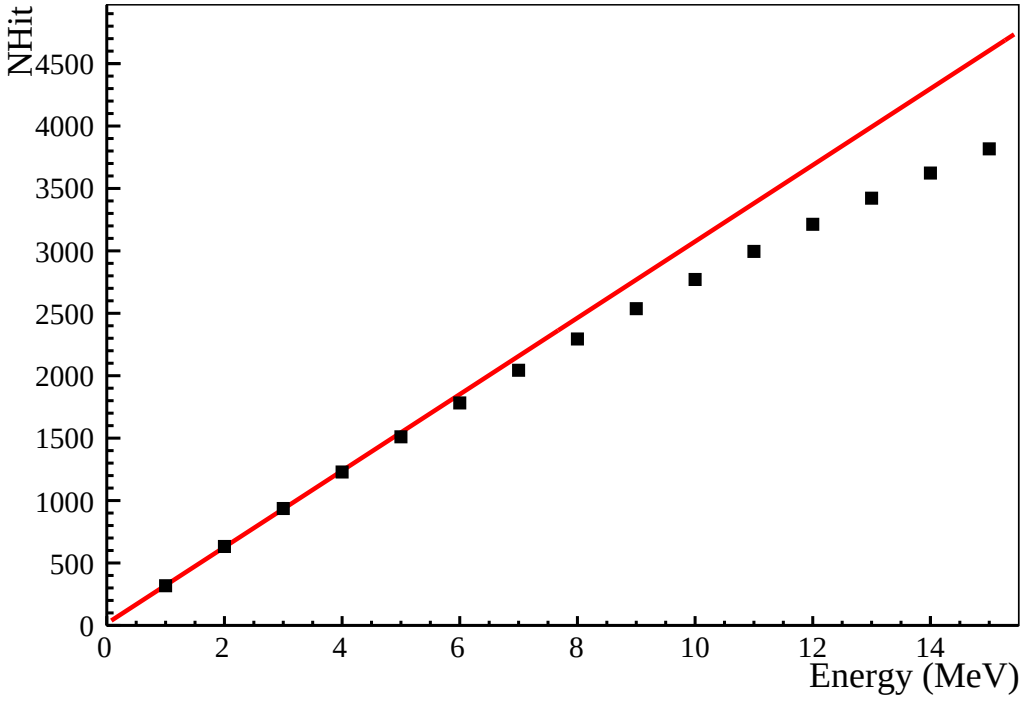


Figure 3.9: NHit as a function of energy for mono-energetic electrons simulated in the centre of the detector. The AV was filled with 0.6 g/L PPO in LAB. It can be seen that relationship ceases to be linear at higher energies. A straight line fit to the energy range 1–4 MeV is shown in red, with a slope of 306 NHit/MeV. Each point represents the mean of a Gaussian fit to the NHit distribution, and error bars are too small to be visible.

As expected, higher energy electrons have a higher NHit. However, the relationship is not linear at higher energies. This is because the detector "saturates", where individual PMTs start detecting multiple photons in a single event and the scintillator emission is no longer proportional to the number of PMTs hit. A straight line is fit to the energy range 1–4 MeV (shown in red), with a slope of 305.5 ± 0.1 and an intercept of 15.0 ± 0.3. The slope is often quoted as the "NHit/MeV", despite the non-linearity, as a measure of light yield in the SNO+ detector. The non-zero intercept is due to the non-linearity of Birks' law at low energies. Within SNO+ analyses, methods have been developed to correct the NHit parameter and account for multiple-hits on single PMTs [130, 79]. However, as the analysis in this thesis only utilises a single energy cut and does not rely on the energy spectrum of detected events, the NHit parameter is used without correction.

Saturation can also occur as an event occurs closer to the AV. This is because the PMTs on the near-side of the AV to the event will detect the majority of the photons, leading to multiple hits in a small cluster of PMTs. The effect of position on saturation can be seen by looking at NHit as a function of radius. Figure 3.10 shows the NHit distribution of 5 MeV electrons simulated in shells of thickness 300 mm, in an AV filled with 0.6 g/L PPO in LAB.

The NHit decrease as the radius approaches the AV, with a significant loss in detected light when the radius becomes greater than 5.5 m. For energy reconstruction in the SNO+ detector, position-corrections are implemented to account for the variations in NHit across the detector volume. However, it can be seen that detected NHit is close to constant at $\sim$1500 NHit for smaller radii, and as such position-correction is not used for the purpose of this thesis. This cut will remove electrons with energies close to 5 MeV with radii $>$5 m from the data set, as the NHit will not be > 1500. While this will result in a small reduction of data useable for reconstruction of direction, any radius-dependent effects on

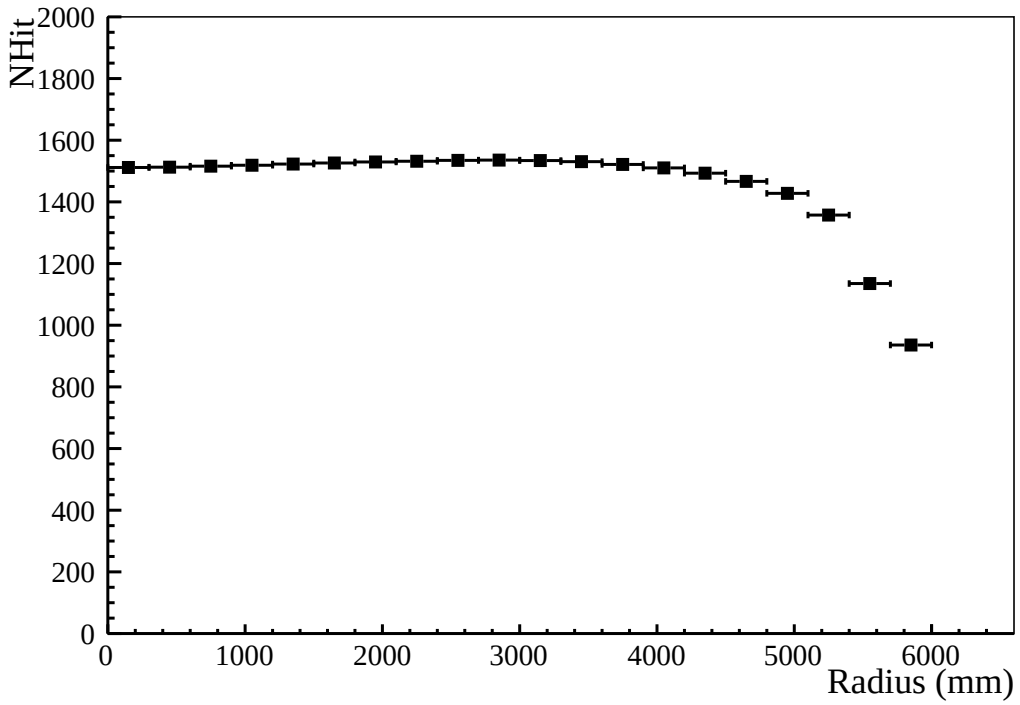


Figure 3.10: NHit as a function of radius for 5 MeV electrons simulated in 0.6 g/L PPO. The NHit decreases near the edge of the AV due to the saturation of the nearby PMTs. Each point represents a gaussian fit to the NHit distribution, and vertical error bars are too small to be visible.

direction reconstruction will be accounted for by applying the same NHit cut to MC predictions.

Reconstruction of event-level parameters offers important discrimination ability between signal and background in neutrino experiments. The following chapter describes the methods and results of direction reconstruction in SNO+, including the impact of the other reconstructed parameters of position and time. Chapter 5 then investigates the potential for improvements to position reconstruction with directional components.

Chapter 4

Reconstruction of Direction in Liquid Scintillator

"Solutions nearly always come from the direction you least expect, which means there's no point trying to look in that direction because it won't be coming from there."

- The Salmon of Doubt, Douglas Adams

One method to extract directional information from a liquid scintillator (LS) based experiment, such as SNO+, is to isolate the directional Cherenkov light using time. As previously discussed, this is possible as Cherenkov light is emitted instantaneously, whereas scintillation light has a characteristic rise and fall time. As the SNO+ detector has taken data through phases of different PPO concentration (described in Section 3.2), it is notable that these timing parameters can change with fluor concentration. Simulated studies of large-scale detectors indicate that time separation could be successfully utilised to reconstruct direction [13]. By using light from the rising edge of the scintillation timing profile, where the anisotropy from Cherenkov light can be clearly seen, direction reconstruction could be possible in the SNO+ detector.

This chapter outlines the method used to reconstruct direction in the SNO+ detector, before demonstrating the use of the method in both simulation and data. This demonstration is the first such event-by-event reconstruction of solar neutrinos in a large-scale high-yield liquid scintillator neutrino detector. Lim-

itations of this method are also investigated, including the reliance on accurate position reconstruction and the degradation of direction reconstruction caused by electron multiple scattering.

4.1 Directionality Methods

In order to reconstruct direction on an event-by-event basis, a maximum likelihood fitter is used. While simpler methods (such as finding the centroid of the Cherenkov photon vectors as used in [13]) are possible, the comparatively slow timing response of the PMTs and lower detector coverage mean this method is less effective. Biases in the position reconstruction (discussed in 4.2.1) are particularly problematic for this method. While methods to correct this position vertex bias are investigated in Chapter 5, it is found that, in the SNO+ scintillator mixture, these methods are only effective at energies of 10 MeV or above.

The physical parameter reconstructed is the initial direction of movement of a charged particle (usually an electron) through the scintillator. Throughout this section, electrons are used in simulation both for the creation of a Probability Density Function (PDF) and for testing the effectiveness of the direction reconstruction method. This is because elastic scattering on electrons is the interaction through which SNO+ observes ^{8}B solar neutrinos, as described in Subsection 1.1.4. The correlation between incoming neutrino direction and electron initial direction is discussed in Section 4.4. The definitions of other reconstructed parameters used in the reconstruction of direction can be found in Section 3.4. For the analysis outlined in this chapter, position-time reconstruction is conducted using the partialFitter. Simulations were run using the RAT software described in Section 3.3 using the optical parameters coordinated for 0.6 g/L PPO in LAB (as used for the Partial-Fill and Full-Fill phases of data taking used in this study, described in Section 3.2). Unless otherwise stated, the detector is simulated with the AV filled with LS, and with perfect detector conditions (i.e. all channels on).

4.1.1 Probability Density Function

A maximum likelihood fitter compares an individual event to a PDF. Therefore, a PDF that clearly demonstrates the anisotropy of the Cherenkov cone at early times is required. This cone presents as a peak in "photon angle" (θ_γ), defined as the angle between the true event direction and the photon direction, shown in Figure 4.1. The photon direction is estimated as the vector between the event position and the hit PMT. This simplistic approach does not account for refraction angles between media, resulting in a potential smearing of the Cherenkov peak as events at larger radii approach the acrylic vessel (AV).

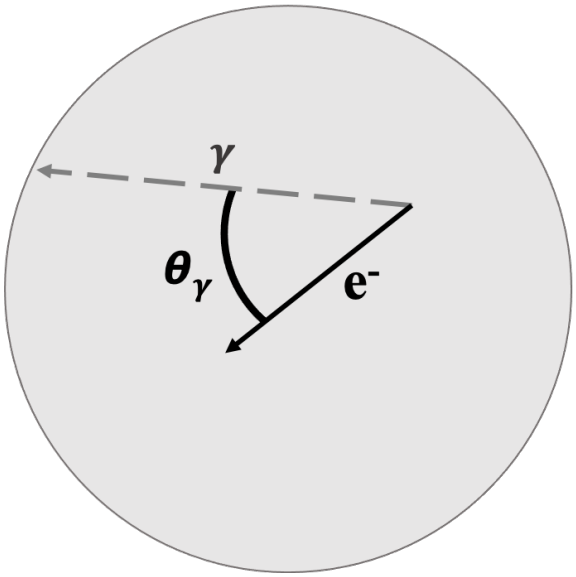
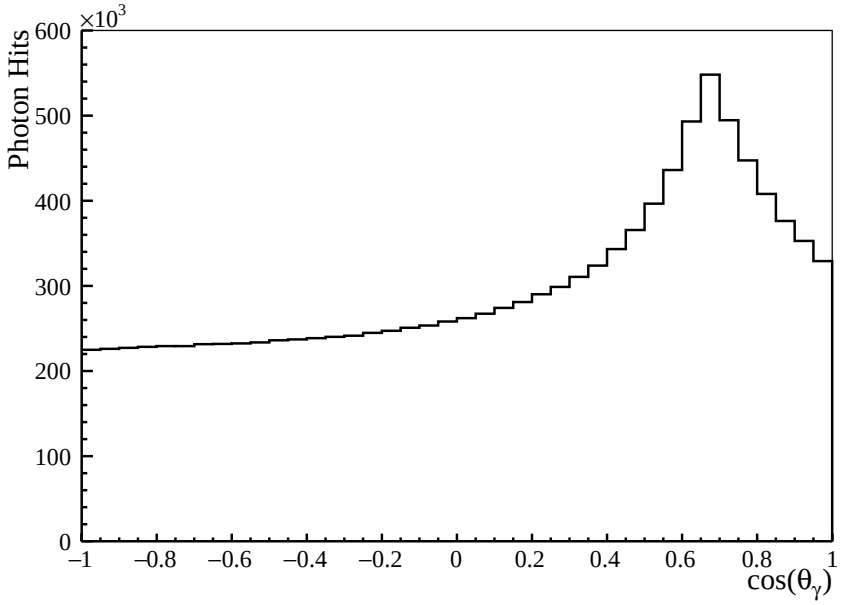
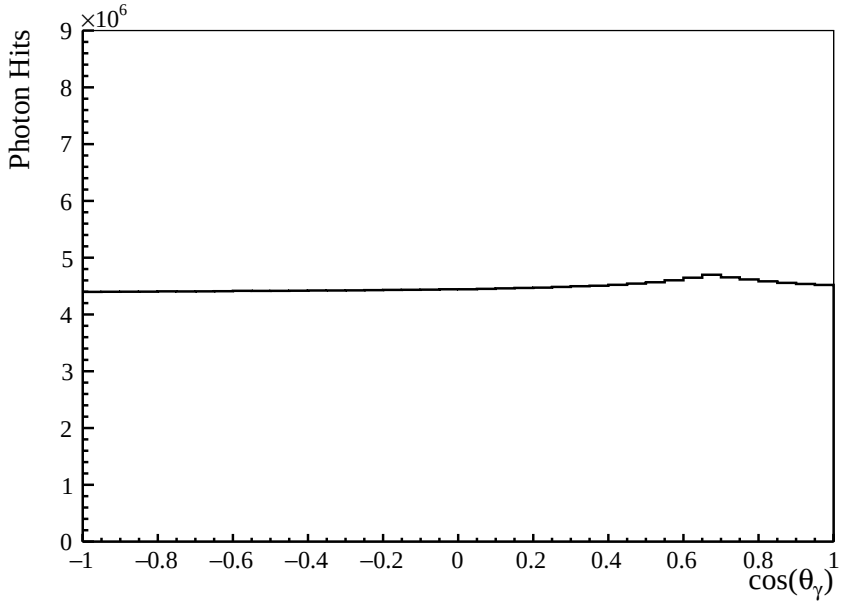


Figure 4.1: Figure demonstrating the "photon angle" (θ_γ), defined as the angle between the event direction and the photon direction. Photon direction is estimated as the vector between the event position and the hit PMT.

In a non-scintillating material (where all photons are Cherenkov photons), this peak is obvious and can be used as a PDF in a likelihood fitter to find the direction, as in Figure 4.2a. However, in scintillator this peak is overlaid onto an isotropic background of scintillation light which has significantly higher light yield. The peak is therefore difficult to isolate and the directional Cherenkov information becomes more difficult to extract, as in Figure 4.2b.



(a) Cherenkov Light Only



(b) Cherenkov and Scintillation Light

Figure 4.2: Photon distribution as a function of $\cos(\theta_\gamma)$ for simulations of 10^5 electrons of energy 6 MeV and isotropic directions in the SNO+ detector. Distributions plotted for Cherenkov light only (a) and a combination of Cherenkov and scintillation light (b). With only Cherenkov light, the peak is prominent at $\cos(\theta_\gamma) \approx 0.7$, the expected angle for a 6 MeV electron. The addition of scintillation light increases the light collected by a factor of ~ 15, meaning the Cherenkov peak becomes barely visible.

In order to isolate the Cherenkov peak, a method must be found to separate the early Cherenkov light using time. This can be done by adding information about the emission time of a photon to our PDF using the time residual (t_{res}) parameter (described in Equation 3.4.1). As Cherenkov light is emitted instantaneously, Cherenkov light should arrive at an earlier t_{res} than scintillation light. By running simulations with either Cherenkov or scintillation light turned off individually, it is possible to see the t_{res} distributions for each emission process, as seen in Figure 4.3.

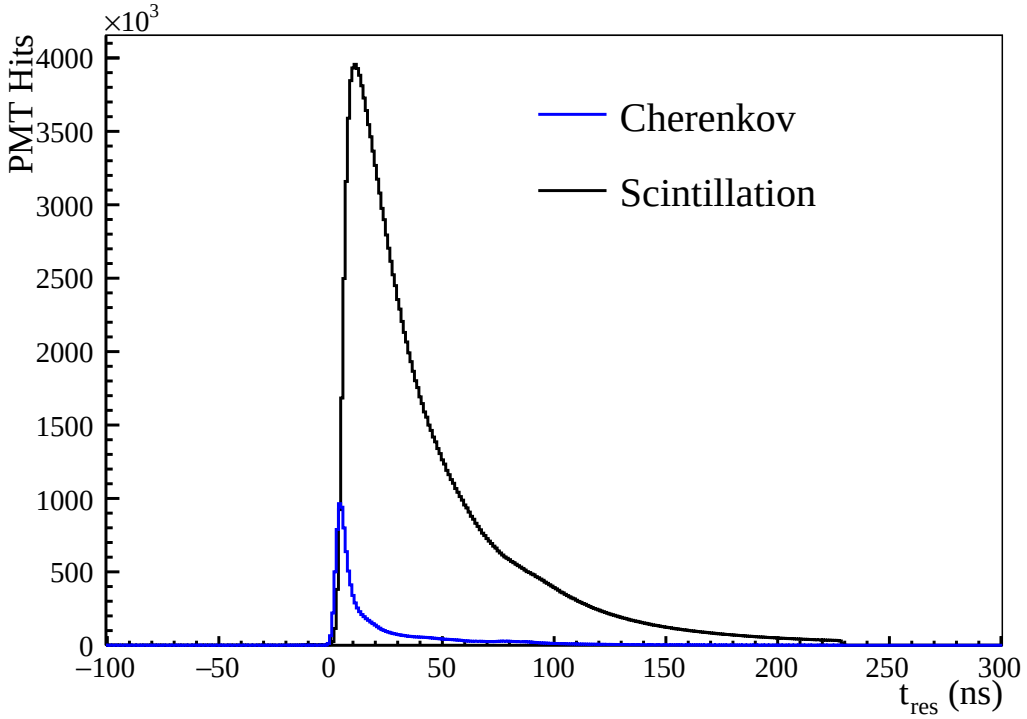
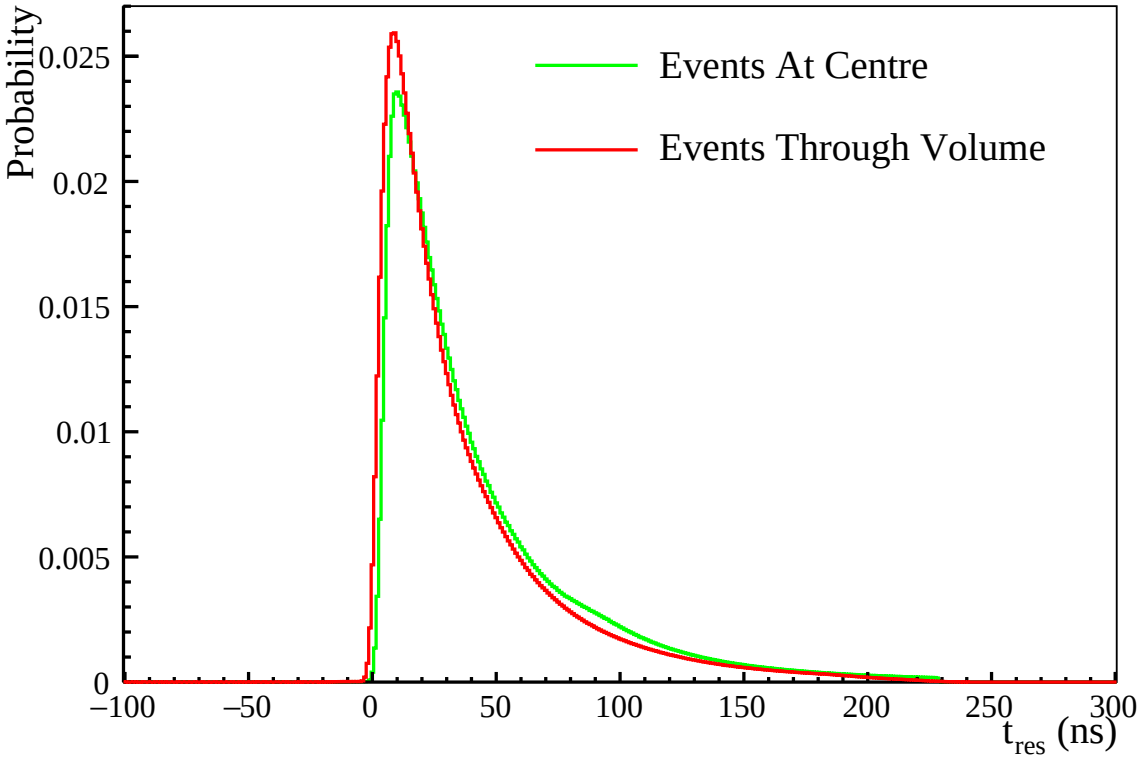


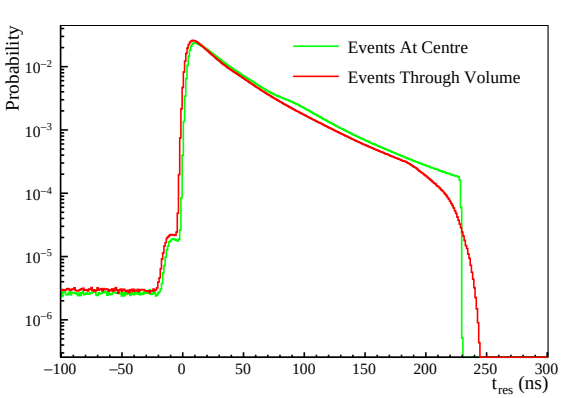
Figure 4.3: Distributions in t_{res} for Cherenkov and scintillation light individually. Cherenkov light is emitted early, within the rising edge of the scintillation profile. Each distribution was created using simulations of 10^5 electrons of energy 6 MeV at the centre of the detector.

It is clear that Cherenkov light is emitted early and t_{res} could be used to separate Cherenkov from scintillation light. However, while these distributions have been made by simulating electrons in the centre of the detector, in reality events will occur throughout the entire volume. t_{res} estimates emission times using straight light path approximations for photons. As events approach the AV,

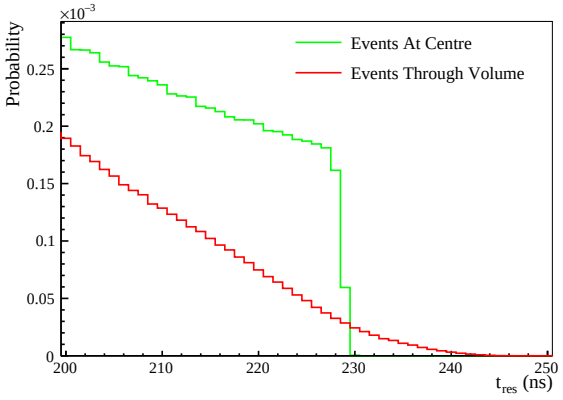
causing refraction angles to become large, this estimation becomes less accurate. To investigate this effect, time residual distributions for events both at the centre and throughout the volume of the scintillator medium can be seen in Figure 4.4.



(a) Photon hits plotted by Time Residual



(b) Time Residual plot, logarithm



(c) Time Residual plot, distribution tails

Figure 4.4: A comparison of the time residual plots for events in the centre (green) and throughout the volume (red) of the AV. The difference in the width of the peak visible in (a) and (b) is caused by the inaccuracy of the straight line path estimation. The tail cut off visible in (b) and (c) is caused by the processed event window. A small pre-pulsing peak is visible at early times in (b). Plots were created using simulations of 10^5 electrons of energy 6 MeV.

The first difference between the distributions is the width of the peak, caused by the inaccuracy of the straight line estimation as the event approaches the AV. The closer the event is to the edge of the scintillator volume, the larger the angles of refraction will become. These refracted light paths take a shorter time for light to traverse than the estimated straight line, meaning the calculated t_{flight} is too large, creating a t_{res} that is too small. This is what leads to the narrower peak in Figure 4.4a when events are simulated through the volume. This also causes the rising edge of the distribution to appear earlier.

Additionally, a sharp cut off can be seen in the tail for the events at the centre, whereas the events throughout the whole volume have a smooth tail. This is due to the event window cuts placed on the events by the detecter trigger logic. As described in Section 3.1.2, PMT hits are only stored as part of an event in a window of $(-180\ ;\ 220)$ ns around around the global trigger. In the centre, this event window cut is directly translated to the t_{res} plot as t_{flight} will vary little from photon to photon, and as such, a cut off is seen at 230 ns. However, throughout the whole volume, t_{flight} varies significantly between "near" and "far" PMT hits in a single event. This means the "near" hits can be within the event window, but have a t_{res} >230 ns, creating a gradual tail.

In order to represent the detector as a whole, the time residual plot created over the entire volume of the detector could be used as the basis for a PDF. However, as will be discussed in Section 4.3, events too close to the AV will not be used in the data set for this analysis. A fiducial volume will be used with a radius of 5.5 m from the centre of the AV. To accurately reflect this, the PDF for the direction reconstruction will also use this fiducial volume.

It is now possible to create a 2D PDF using $\cos(\theta_\gamma)$ and t_{res} in order to find the Cherenkov peak. Keeping time information in the PDF allows the rising edge of the scintillation profile to be used as a whole, without tuning for the fraction of Cherenkov photons. A time window of $(-5\ ;\ 15)$ ns is used in order to reduce

the impact of the distribution tail.

In order to identify the Cherenkov peak, the PDF is first generated assuming the MC truth position-time vertex for the electron in the calculations of both $\cos(\theta_\gamma)$ and t_{res}. This PDF was created using 6 MeV electrons within a radius of 5.5 m of the centre of the AV, and can be seen in Figure 4.5.

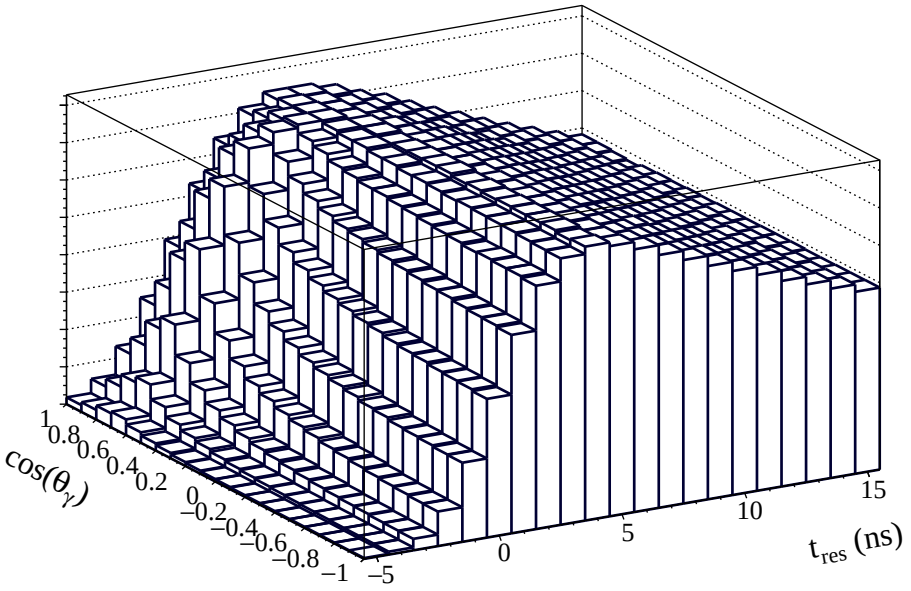


Figure 4.5: The 2D PDF in t_{res} and $\cos(\theta_\gamma)$, assuming the MC truth position-time vertex. At early times, a peak is visible at the expected angle of $\cos(\theta_\gamma) \approx 0.7$. The PDF was created using simulations of 10^5 electrons of energy 6 MeV throughout the AV with a maximum radius of 5.5 m.

There is clear anisotropy on the rising edge of the scintillation light. The Cherenkov peak is visible and, therefore, can be used as the basis for a direction reconstruction algorithm. However, in data the position-time vertex would need to be reconstructed. It is therefore also useful to look at this PDF using the reconstructed position and time (as described in Section 3.4) for all calculations. This PDF was also created using 6 MeV electrons within a radius of 5.5 m of the centre of the AV, and can be seen in Figure 4.6.

There are immediately visible differences between the PDFs. Most notably, there is an apparent peak in angle at $\cos(\theta_\gamma) = -1$, meaning light detected in the direction opposite to the electron's direction of travel. This is more clearly

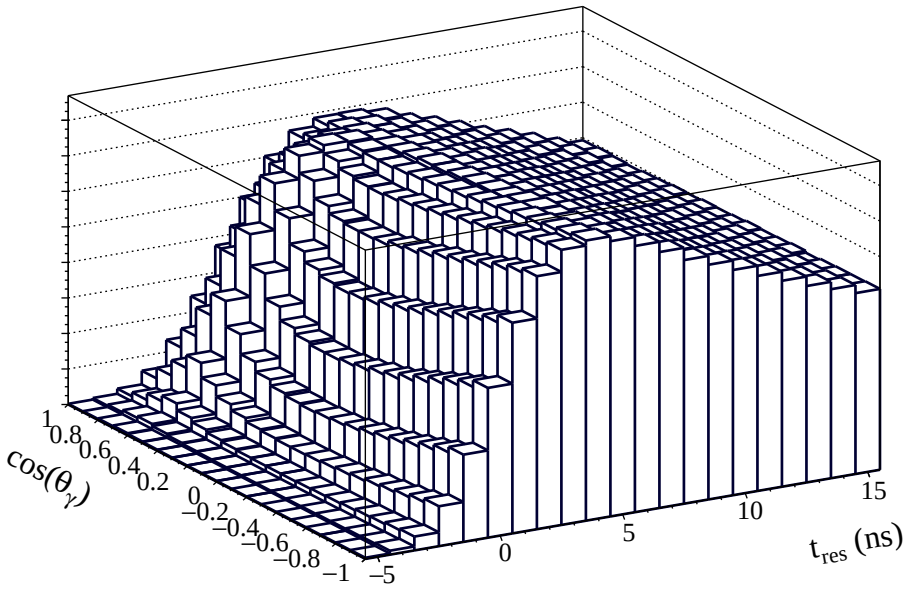


Figure 4.6: The 2D PDF in t_{res} and $\cos(\theta_\gamma)$, using the reconstructed position-time vertex. While the Cherenkov peak is still visible close to the expected angle of $\cos(\theta_\gamma) \approx 0.7$, there is also an apparent peak in the backwards direction of $\cos(\theta_\gamma) = -1$. The PDF was created using simulations of 10^5 6 MeV electrons throughout the detector volume, with a maximum radius cut of 5.5 m.

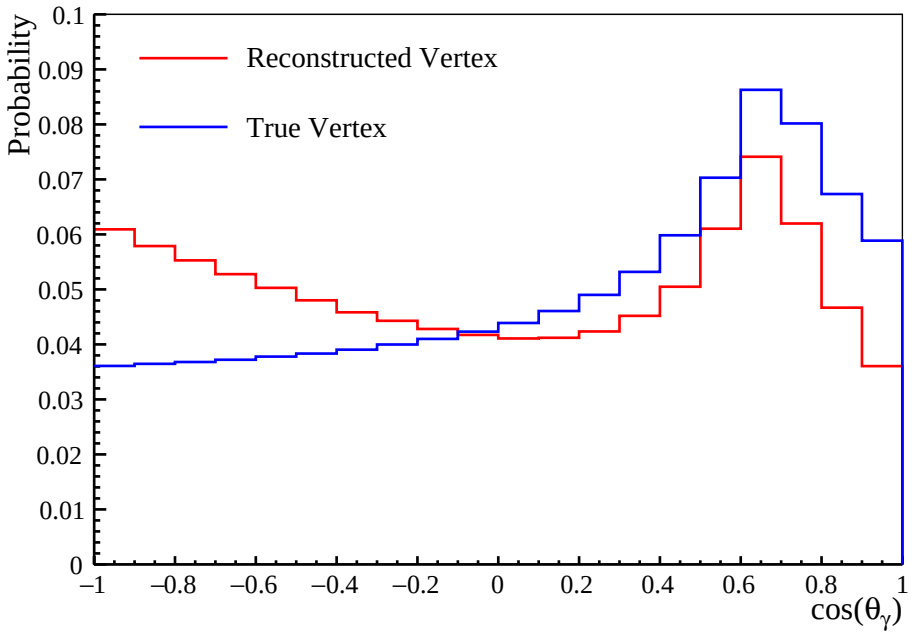


Figure 4.7: A comparison of photon hits with a calculated $t_{res} < 2$ ns in $\cos(\theta_\gamma)$ for the true and reconstructed vertices. It can be seen that there is a significant peak in the backwards direction ($\cos(\theta_\gamma) = -1$) when using the fitted vertex. The Cherenkov peak has also shifted slightly. The distributions created using simulations of 10^5 6 MeV electrons throughout the detector volume, with a maximum radius cut of 5.5 m.

seen in a comparison of only photon hits with a calculated $t_{res} < 2$ ns (Figure 4.7). This view also shows a slight shift in the Cherenkov peak angle to lower $\cos(\theta_\gamma)$, corresponding to a wider Cherenkov angle.

This difference must be caused by inaccuracies in the reconstruction of the position-time vertex. This will be investigated in Section 4.2.1. However, even with an unusual shape, the anisotropy in θ_γ on the rising edge of the scintillation profile means this PDF can be used to reconstruct direction.

4.1.2 Reconstruction of Direction

Direction is reconstructed by using the histogram in Figure 4.6 as a PDF in a binned maximum likelihood fit. A grid search optimiser was chosen for robustness. This involves taking equally-spaced steps along each dimension, and then at each step calculating the likelihood using a binned likelihood sum as given by Equation 4.1.1:

$$\ln(\mathcal{L}) = \sum_i n_i \ln(p_i) \tag{4.1.1}$$

where $\mathcal{L}$ is the likelihood, i is the bin number, n is the number of photons detected in that bin, and p is the height of the bin in the PDF.

This method maps the likelihood space to find the point with the maximum likelihood. For the results presented in this thesis, 50 steps were taken in $\cos(\theta)$ and 90 steps were taken in ϕ, where θ and ϕ are the polar and azimuthal angle, respectively, in detector coordinates.

Direction reconstruction was tested using electrons simulated over the volume of the detector at energies in the range 2 MeV to 20 MeV. These simulations were run using detector conditions from 100 runs from within the combined Partial-Fill and Full-Fill data set (explained in more detail in Section 4.3). The use of these conditions means the detector is simulated in the same state as the true detector for a given run number, including the same channels being turned off and the fill level of the detector. This is expected to reduce the effectiveness

of the direction reconstruction, due to loss of photocathode coverage and complex optics in Partial-Fill. However, this also allows a more accurate comparison between predictions from simulation and the results from data.

Only events with a valid position-time vertex reconstruction were allowed. A radius cut of $r < 5.5\,\text{m}$ was applied to all runs to avoid the optical effects introduced by large refraction angles and total internal reflection close to the AV. A cut of $z > 1\,\text{m}$ from the equator of the AV was also applied for Partial-Fill runs due to the water-LS interface, which also suffers from refraction and reflection causing inaccurate reconstruction. The results are presented in terms of $\cos(\alpha)$, where α is the angle between the MC true initial direction and the reconstructed direction of the electron. These results can be seen in Figure 4.8.

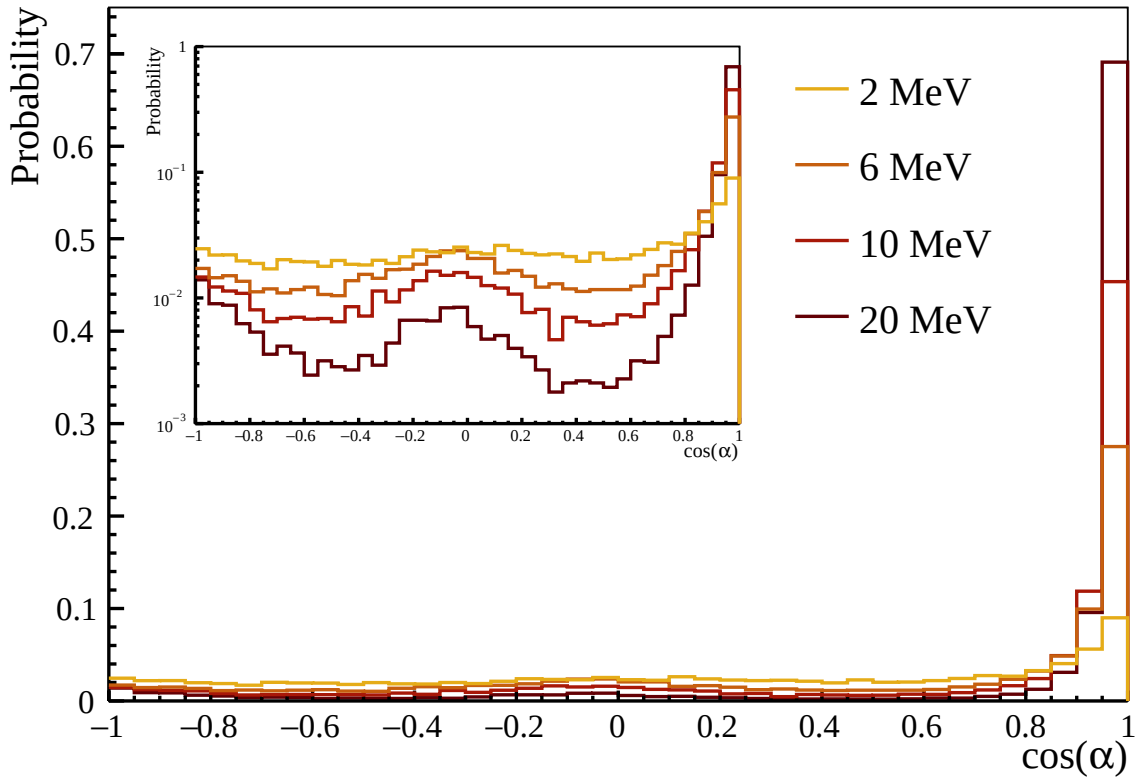


Figure 4.8: Results of direction reconstruction for simulations of different electron energies, with a log plot inset. Simulations were run using representative run conditions. It can be seen that there is a strong energy dependence for the effectiveness of the reconstruction. There is also an interesting tail shape seen, with small peaks at $\cos(\alpha) \approx 0$ and $\cos(\alpha) = -1$.

In order to compare the effectiveness of the directional reconstruction, the percentage of events with $\cos(\alpha) > 0.8$ is calculated. The results of this can be seen in Table 4.1. Reconstruction of the electron direction is strongly dependent on the energy of the electron, as expected, with higher energy electrons reconstructing more accurately. There is also an unusual tail shape observed, with peaks at $\cos(\alpha) \approx 0$ and $\cos(\alpha) = -1$. This shape is due to position reconstruction effects, and is explored in more detail in Section 4.2.1.

Energy (MeV)	% with $\cos(\alpha) > 0.8$
2	21.9 ± 0.4
6	45.6 ± 0.6
10	64.6 ± 0.7
20	83.0 ± 0.8

Table 4.1: Comparison of the directional reconstruction for simulated electrons at different energies, based on the percentage of events that reconstruct with $\cos(\alpha) > 0.8$. Uncertainties are assumed to be purely statistical.

The results of this direction reconstruction method hold significant promise. If used on high energy events, a simple cut of $\cos(\alpha) > 0.8$ would make it possible to retain 45-80% (depending on energy) of the directional signal events while rejecting 90% of an isotropic background. More sophisticated background signal extraction, such as a likelihood comparison used in conjunction with energy, could make the efficiency of this background rejection method even higher.

However, there are phenomena that affect the ability to reconstruct direction in SNO+. These place limits on of the accuracy of direction reconstruction that is obtainable. In order to understand where improvements may be made to this method, and what the maximum effectiveness would be, two major limiting effects are explored in Section 4.2.

4.2 Effects Limiting Direction Reconstruction

There are several factors impacting the effectiveness of the direction reconstruction. The most prominent of these are the accuracy of position reconstruction and the electron multiple scattering within the detector.

4.2.1 Effect of Position Reconstruction

In Section 3.4, the method of reconstruction of a position-time vertex in the SNO+ detector was explained. The resolution was found to be $\sim$15 cm in each cartesian coordinate (creating a spatial resolution of $\sim$26 cm) with no significant biases. However, when these reconstruction algorithms are tested, electrons are generated with isotropic directions. This means a bias related to the direction of movement of the electron would not be seen.

In order to investigate the position reconstruction along the direction of motion of the electron, the drive parameter is used. Drive is defined as the mis-reconstructed distance along the true direction of momentum of a particle, as illustrated in Figure 4.9.

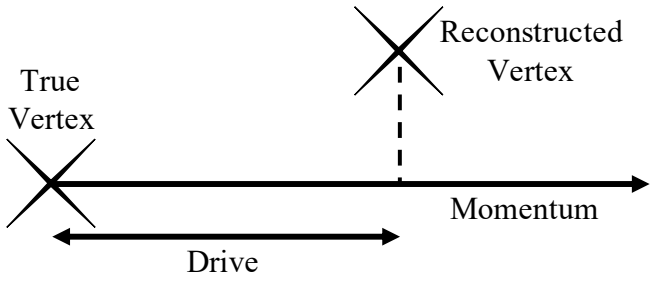


Figure 4.9: Figure demonstrating drive, the mis-reconstruction of the position vertex along the particle's true direction of momentum.

Using the same 100 simulated runs as described in the previous section, the drive of 6 MeV electrons can be investigated. This is seen in Figure 4.10.

Using a Gaussian fit to this distribution, there is a bias of 188.5 ± 0.6 mm and a standard deviation of 84.8 ± 0.5 mm. This bias changes with energy, as can be

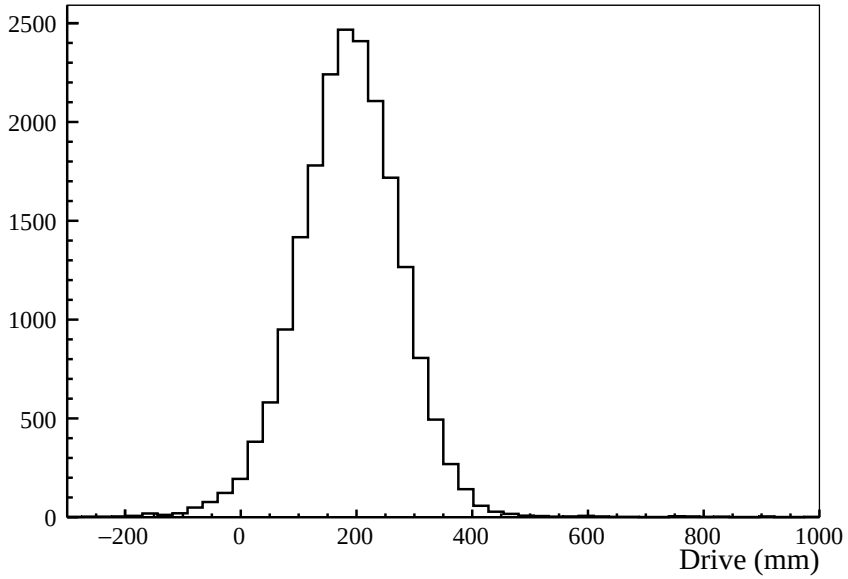
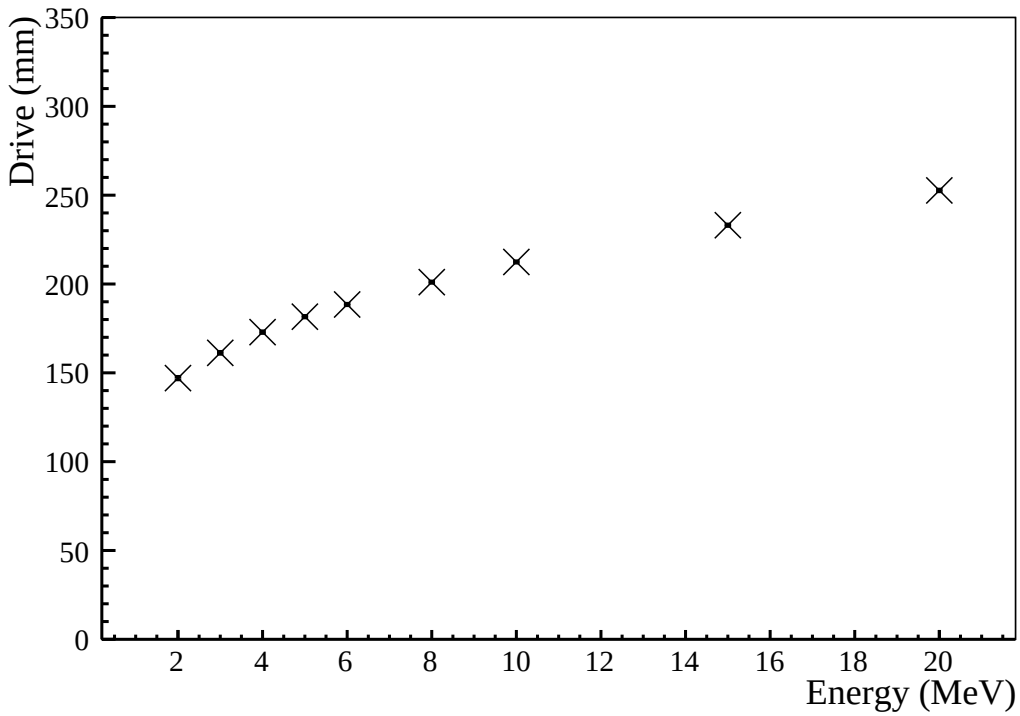


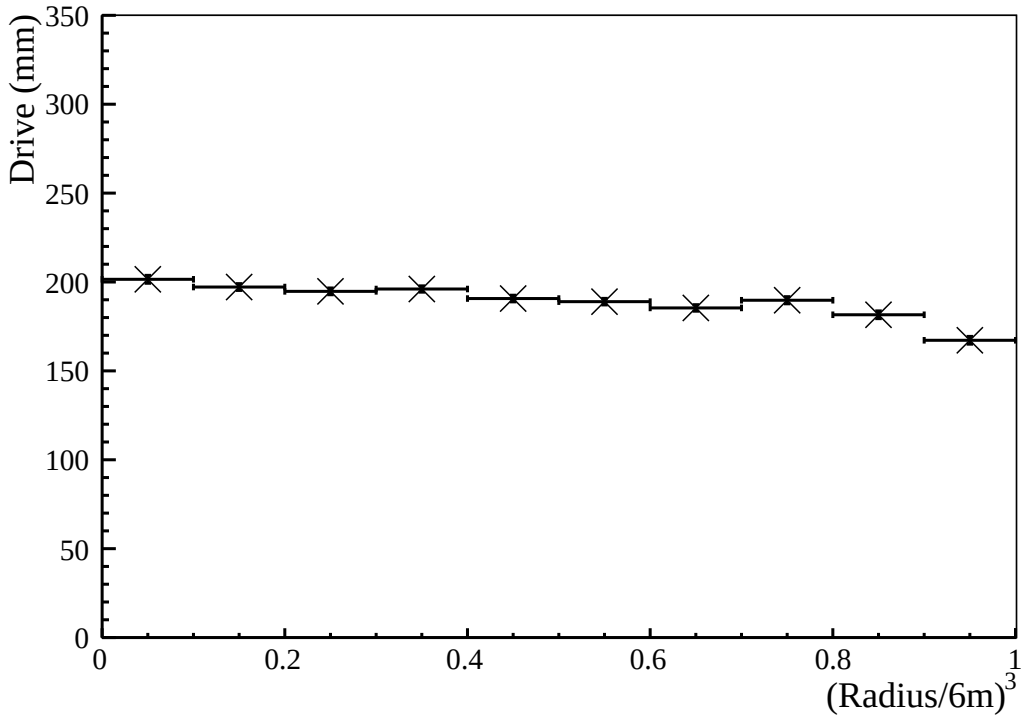
Figure 4.10: The drive of simulated 6 MeV electrons in SNO+ detector. When fit to a gaussian, this distribution has a mean of 188.5 ± 0.6 mm and a standard deviation of 84.8 ± 0.5 mm.

seen in Figure 4.11a, with higher energies producing a larger drive. It does not have a strong dependance on radius, as seen in Figure 4.11b, although it does decrease slightly near to the AV.

The existence of drive is due to two causes: track length and Cherenkov light. As explained in Section 3.4, in event reconstruction in SNO+ it is assumed that any given event is point like. However, after an electron is scattered, the electron travels a certain distance before stopping. It is assumed that the reconstructed point vertex will be located at an average position somewhere along the track, which would cause a small drive effect in the direction of motion compared to the initial scattering event position. However, by looking at the average energy deposition in LAB ($\frac{dE}{dx} \approx 2\,\text{MeV/cm}$), it can be shown that the track should only be a few centimetres long at these energies. This can be confirmed by turning off Cherenkov light in simulation, which leads to a large decrease in drive, as seen in Figure 4.12.



(a) Drive as a function of energy.



(b) Drive as a function of radius, 6 MeV.

Figure 4.11: The drive as a function of energy and radius in simulation. The mean was obtained by fitting drive distributions to a Gaussian. Vertical statistical error bars are too small to be visible. Drive has a large dependence on energy, increasing at higher energies. There is not a strong dependence on radius, but very near to the AV drive decreases slightly.

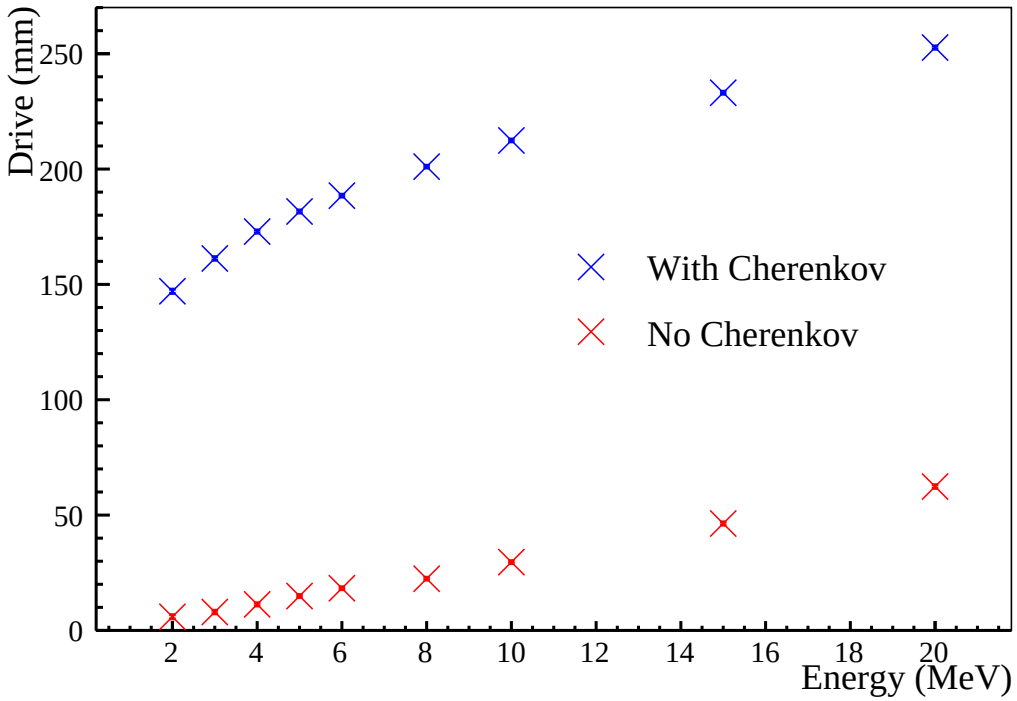


Figure 4.12: A comparison of drive with and without Cherenkov light present in simulation. Statistical error bars are too small to be seen. It can be seen that drive is significantly smaller when Cherenkov light is omitted.

It is clear that Cherenkov light adds significantly to the drive. As Cherenkov light is both directional and "early", a position reconstruction based on t_{res} causes the vertex to be pulled in the direction of the Cherenkov light, as demonstrated in Figure 4.13.

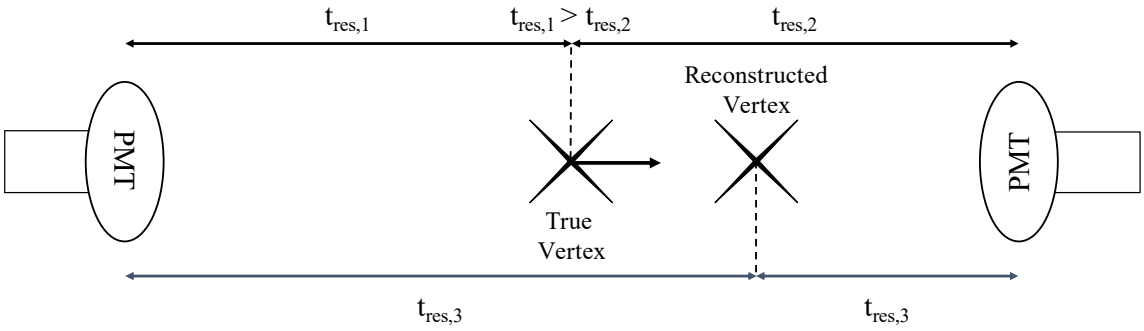


Figure 4.13: A simplified explanation of drive. As Cherenkov light is emitted before scintillation light, t_{res} in the forward direction is smaller than that in the backward direction. Moving the vertex along the direction of motion decreases the time of flight in the forward direction, increasing the time residual calculated at the forward PMT.

At the true vertex, a time residual is calculated in example "backward" and "forward" directions, $t_{res,1}$ and $t_{res,2}$ respectively. As t_{res} (defined in Equation 3.4.1) is an estimation of emission time and directional Cherenkov light is emitted earlier than isotropic scintillation light, $t_{res,1} > t_{res,2}$. However, position reconstruction algorithms used in SNO+ do not account for angular information in the photon hit distribution. This means the vertex will be pulled forward, increasing t_{flight} in the backward direction and decreasing it in the forward direction. At the final reconstructed vertex, the calculated t_{res} in both directions are now the same.

Alongside there being a directional component of position reconstruction, drive also has an impact on the effectiveness of direction reconstruction. It was seen in Section 4.1.1 that the PDF in $\cos(\theta_\gamma)$ and t_{res} changes when using either the MC truth or reconstructed position-time vertex. The cause of this change can now be attributed to the effect of drive. As the reconstructed vertex is moved forward along the direction of motion of the electron, the t_{flight} to PMTs located in the backwards direction increases. This decreases the t_{res}, making these hits appear to have been emitted earlier and causing the peak at $\cos(\theta_\gamma) = -1$ in Figure 4.6. The shift in cone angle seen in Figure 4.7 can be explained by the reconstructed position being closer to the observed Cherenkov ring on the PMTs, creating an artificially widened Cherenkov angle.

As the shape of the event is changed by drive, the results of direction reconstruction are also changed. The effect of position reconstruction inaccuracy on direction reconstruction can be tested by running direction reconstruction assuming the true position-time vertex. The PDF shown in Figure 4.5 is used for the maximum likelihood search. A comparison of direction reconstruction using the true and reconstructed event vertices can be seen in Figure 4.14, using the simulation of 6 MeV electrons in the run conditions described in previous sections.

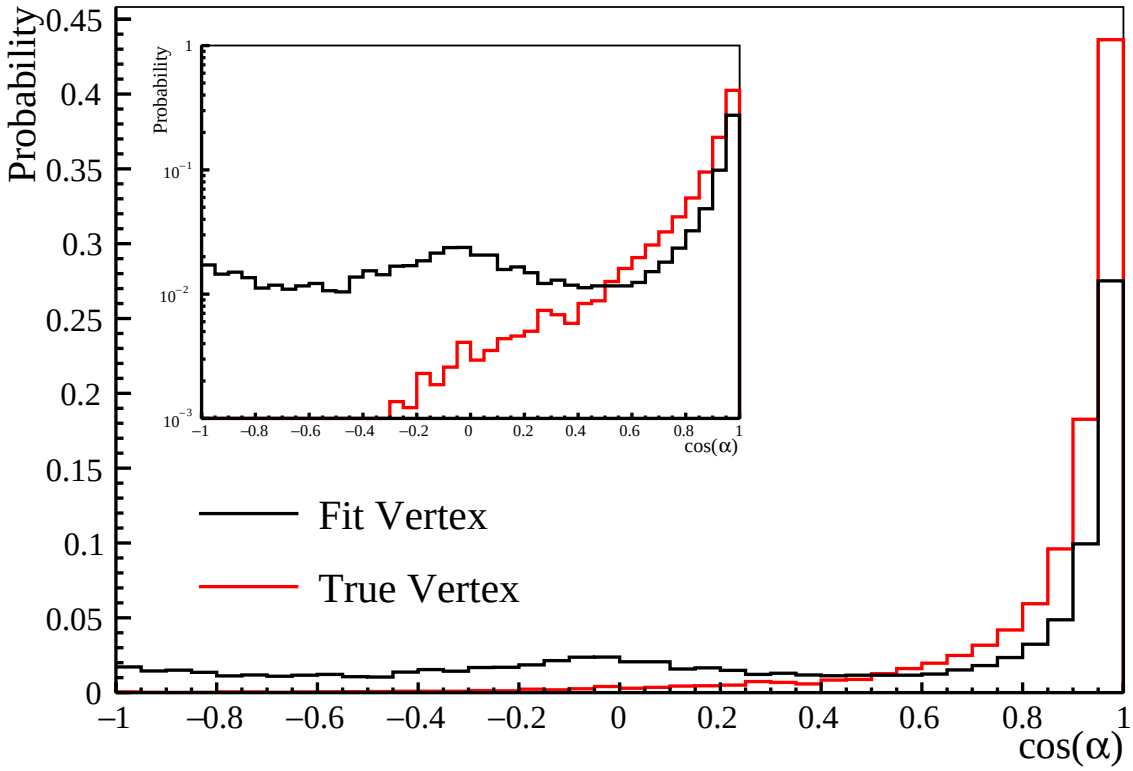


Figure 4.14: Results of direction reconstruction, comparing the use of reconstructed and MC truth positions. Plots generated for simulations of 6 MeV electrons. It can be seen that using the true position gives a large improvement in direction reconstruction. Notably, the peaks at $\cos(\alpha) \approx 0$ and $\cos(\alpha) = -1$ are no longer present.

The mis-reconstruction of the position-time vertex has a large impact on the potential for directionality. The percentage of events that reconstruct with $\cos(\alpha) > 0.8$ increases from 45.6 ± 0.6 to 77.4 ± 0.7. Notably, there is also a change to the shape of the distribution tail. The peaks in the tail disappear when the true position is used, confirming they are caused by the drive of a reconstructed vertex. Drive causes the "backwards" peak to appear in the early times of an event, which creates a degeneracy in the likelihood space used to reconstruct the direction. Finite photon sampling then causes a minority of events to reconstruct with direction either opposite or perpendicular to the true direction. The variation in drive also changes the individual prominences of the backwards peak, meaning some events will not be easily reconstructed against the PDF.

The reconstruction of position and direction seem to be interdependent, with each parameter affecting the ability to reconstruct the other. This opens the possibility of reconstructing a single direction-position-time vertex, with the view to improving both parameters. This is explored in Section 5.1, and the limitations of such a method in the SNO+ detector are discussed. Improved position reconstruction that reduces drive has scope for improving direction reconstruction, and should continue to be investigated.

4.2.2 Effect of Electron Multiple Scattering

Electron multiple scattering (MSC) is the process of an electron undergoing several small-angle scatters as it traverses through matter [131]. Direction reconstruction assumes the electron travels in one direction along a straight track, around which a Cherenkov cone is emitted. However, MSC changes the direction of travel, meaning it will impact the ability to reconstruct direction.

The magnitude of MSC can be investigated in MC by comparing an "average" direction of travel to the initial direction of momentum for an electron. This average direction vector can be constructed between the initial and final points of the electron track in MC, as demonstrated in Figure 4.15. In MC, the initial point of the track is classified as the MC truth position vertex of the event.

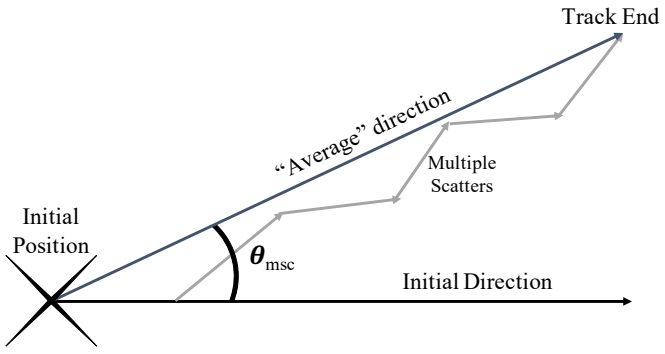


Figure 4.15: An explanation of the angle θ_{msc}. An average direction of the particle track is defined as the vector between the MC initial position of an electron and the final position of the MC track. θ_{msc} is then defined as the angle between this average direction and the initial MC truth direction of the electron's momentum.

The distributions of $\cos(\theta_{msc})$ can be seen in Figure 4.16 for electrons with energies 2 MeV, 6 MeV and 10 MeV. These distributions were generated using electrons in the run conditions described in Section 4.1.2.

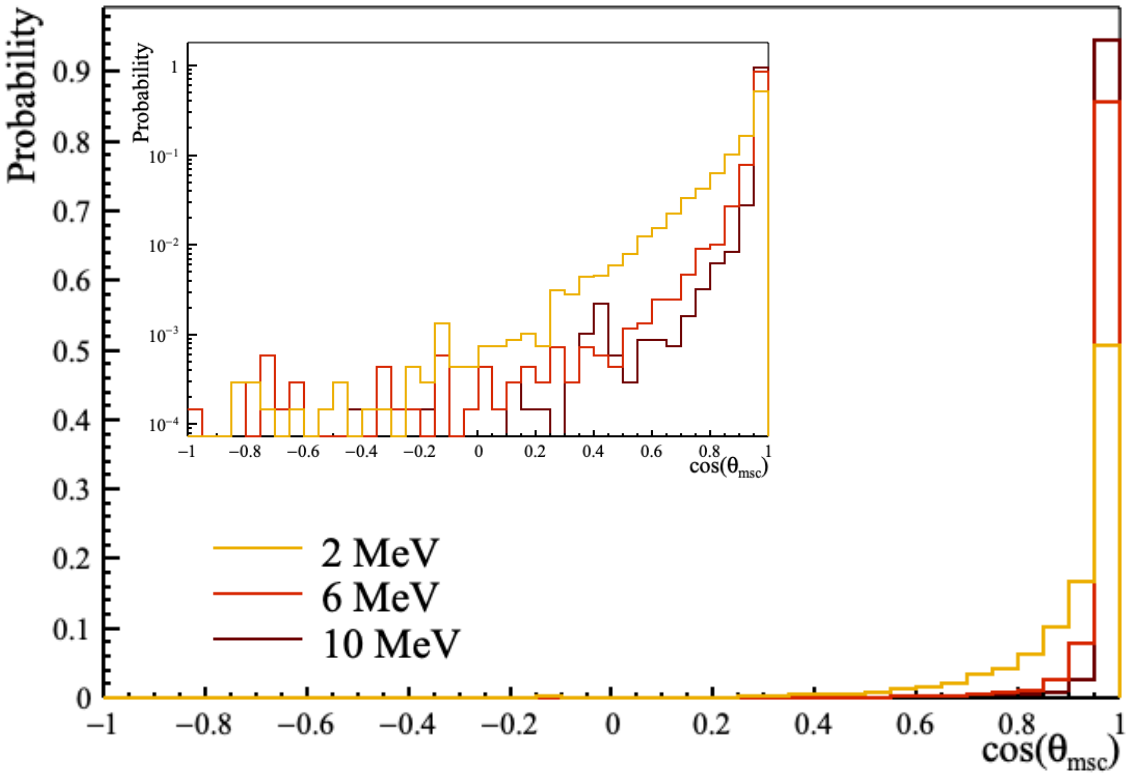


Figure 4.16: Distributions of $\cos(\theta_{msc})$ for simulated electrons of different energies travelling through LABPPO. It can be seen that there is a strong dependance on energy, with higher energy electrons scattering less.

As expected, this multiple scattering angle is dependent on energy, with higher energy electrons scattering less than lower energy electrons. In order to examine the effect this has on the ability to reconstruct direction, Table 4.2 contains the percentages of events with $\cos(\theta_{msc}) > 0.8$. Events that move in an average direction substantially away from the initial direction of movement will be difficult to reconstruct.

Even at low energies, a high proportion of events have an average direction that is close to the true direction. This is promising for the prospect of using direction reconstruction in lower energy studies such as $0\nu\beta\beta$. If perfect direction

Energy (MeV)	%
2	84 ± 1
6	97 ± 1
10	99 ± 1

Table 4.2: Comparison of the magnitude of multiple scattering in LS at different energies in simulation. This is presented using the percentage of events with $\cos(\theta_{msc}) > 0.8$.

reconstruction was possible of the average direction travelled by an electron, significant background rejection would still be possible at these energies.

However, the average direction is not the only effect of multiple scattering that can degrade the effectiveness of direction reconstruction. Each scatter changes the direction by small angles, creating a Cherenkov cone that is ill defined, even if it is centred around an "average" direction that is close to the true direction. This leads to a decreased effectiveness of direction reconstruction as the Cherenkov cone is not "clean". While this is also the case in water Cherenkov detectors (and often used as a method of particle identification between electrons and muons due to their differing magnitudes of MSC), SNO+ suffers from the additional background from isotropic scintillation photons.

In order to estimate the magnitude of the effect of multiple electron scatters on directional reconstruction, MC simulations were run without multiple scattering. This means all simulated electrons only travelled in the direction of their initial momentum. The results can be seen in Figure 4.17, once again using the simulations of 6 MeV electrons in the run conditions described in Section 4.1.2.

It can be seen that electron multiple scattering in the scintillator clearly has a large effect on the ability to reconstruct initial direction. Without multiple scattering, the peaks in the distribution are much sharper. Notably, the peaks in the tail due to the drive effects are still present, as the drive effects discussed in Section 4.2.1 are not changed.

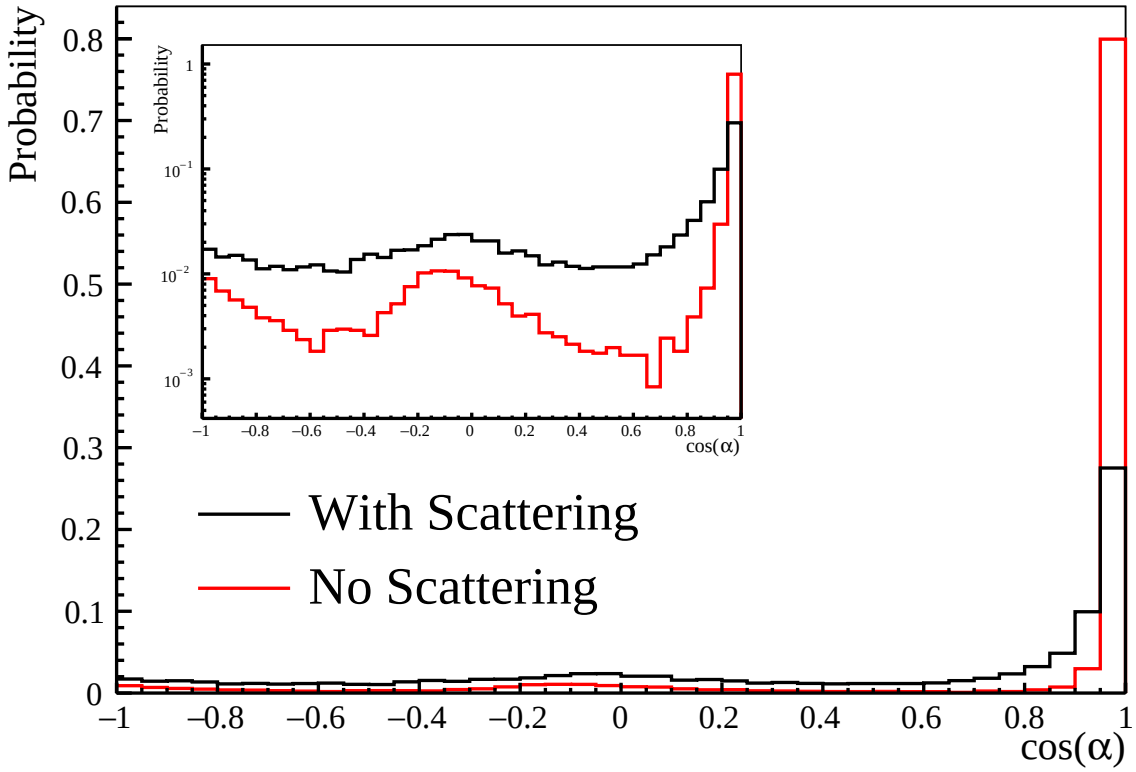


Figure 4.17: Results comparing the effectiveness of direction reconstruction with and without multiple scattering of simulated 6 MeV electrons in 0.6 g/L PPO. It can be seen that multiple scattering has a large effect on the ability to reconstruct the original direction of the electron, as the direction is changed along the electron's path. Despite significant sharpening of the peak, the tail effects caused by drive are still present.

Unfortunately, it is not possible to reduce the effect of electron multiple scattering within the SNO+ detector. However, it is important to know the limits placed on the ability to reconstruct direction. These studies show that the reconstruction of direction based on the likelihood of the PDF is systematically limited by the loss in definition of the Cherenkov cone due to multiple scatters of the electron as it travels. There is also an effect due to the average direction of the electron — and thus the average position of the Cherenkov cone — deviating from the initial direction. For use in physics analyses, the initial direction of the electron is the desired reconstructed parameter as it has the greatest correlation with the direction of an incoming neutrino (examined further in Section 4.4.1). The loss of definition of the Cherenkov cone is reduced at higher ener-

gies, allowing more accurate directionality, as the electron scatters less and has a longer track along which to emit a cone. The impact of multiple scattering on the ability to reconstruct direction could be reduced in future detector designs by prioritising higher effective photocathode coverage. This would allow a more thorough sampling of photon angles. However, there will still be an energy-dependent practical limit imposed by scattering.

4.2.3 Summary of Limiting Effects

Figure 4.18 shows the effect of both electron multiple scattering and position reconstruction on directionality, using the runs described above and 6 MeV electrons. A comparison is included where there is no multiple scattering and the true position vertex is used. Table 4.3 shows the percentage of events with $\cos(\alpha) > 0.8$ for each of these scenarios.

Scenario	%
No Scattering, True Vertex	98.2 ± 0.8
With Scattering, True Vertex	77.4 ± 0.7
No Scattering, Fit Vertex	84.0 ± 0.8
With Scattering, Fit Vertex	45.6 ± 0.6

Table 4.3: Comparison of the directional reconstruction of simulated 6 MeV electrons considering the effects of multiple scattering of electrons and biases in position reconstruction, looking at the percentage of events that reconstruct with $\cos(\alpha) > 0.8$.

It is clear that both multiple scattering and position reconstruction have large effects on the ability to effectively reconstruct direction. While multiple scattering is an unavoidable effect, there are is potential to improve position reconstruction by including a directional component, leading to the improved reconstruction of direction. However, for the purposes of direction reconstruction, these effects can be used to set limits on the achievable directionality in SNO+, as the

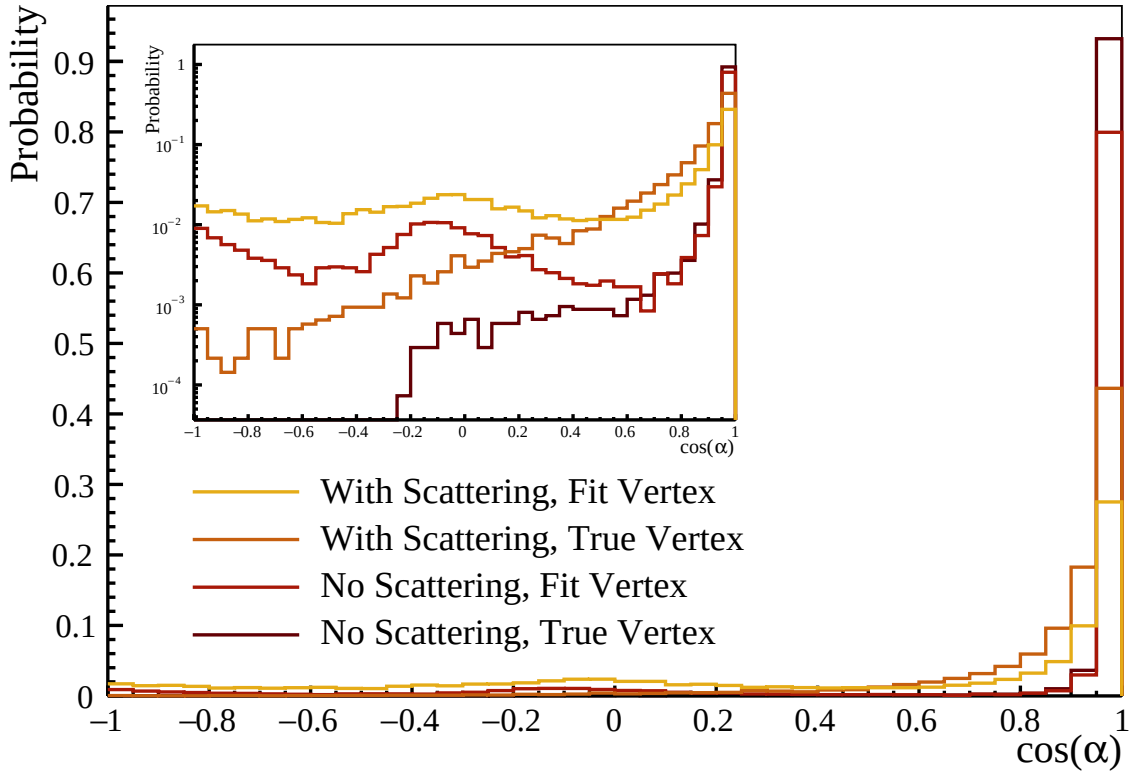


Figure 4.18: Direction reconstruction of simulated 6 MeV electrons for cases of 1) no multiple scattering and using the true vertex position (brown); 2) no multiple scattering and using the fit vertex position (red); 3) with multiple scattering and using the true vertex position (orange) 4) with multiple scattering and using the fit vertex position (yellow). It can be seen that using the MC truth vertex removes the peaks in the tail, whereas removing electron multiple scattering makes peaks in the distribution sharper.

two effects combined reduce the percentage of events with $\cos(\alpha) > 0.8$ from 98.2% to 40.6%. Other systematic effects, such as NHit, are sub-dominant.

4.3 Dataset

In Section 3.2, the multiple data acquisition phases SNO+ underwent throughout commissioning were outlined. Two of these phases were used for the purpose of this analysis: the Partial-Fill Phase (Period 1) and the Full-Fill 0.6 g/L Phase (Period 2). While the final scintillator cocktail achieved in the SNO+ experiment contained 2.2 g/L PPO, these two stable phases contained liquid scintillator with a concentration of 0.6 g/L PPO. As described in Section 1.3, primary fluors are

used to shift the wavelength of emitted light away from the absorption length of the solvent. The timing of the non-radiative transmission and de-excitation of the fluor depends on its concentration in the solvent, meaning timing constants for the emission of scintillation light can be tuned by varying concentration. The lower concentration of the fluor PPO leads to a slower timing profile than in a higher concentration, as seen in Figure 3.6. As this analysis utilises the timing separation of Cherenkov light, this slower timing was used as an opportunity to investigate direction reconstruction.

As described in Section 3.1.2, data in SNO+ is collected in runs. Period 1 spanned the run-range 257693-264716, and Period 2 spanned 270168-271709. When running under normal conditions, these runs are an hour long. Before data analysis can be conducted, runs must be selected for data quality.

A run will not be denoted as a "Physics Run" if there are maintenance tasks being performed or if there is active calibration (using sources such as LED or laser light input, or nuclear decay sources internal or external to the AV). Physics runs may then be rejected for several reasons, with requirements varying between specific analyses. Examples of rejection criteria include:

- Not all crates are at high power - This criteria is particularly important for directionality studies, where detector isotropy should be maximised for the best results.
- Abnormal trigger rates caused by faults in the electronics.
- Abnormal rates in individual channels, including OWL PMTs.
- High number of errors in the data readout.
- Runs too short - Exact run length varies between analyses, for this data set this was selected to be 15 min.
- Breakdowns in the detector electronics.

- External factors such as rock blasting within the mine, storms interfering with electrical supplies, or earthquakes.

For Period 1, data processing and simulation were completed using RAT-6.18.9. For Period 2, data processing used RAT-6.18.11, and simulation used RAT-6.18.15. Once "good physics" runs were selected for the purpose of this analysis, individual events were then selected.

4.3.1 Event Selection

It is expected that higher energy events will reconstruct more accurately in direction due to both higher photon yield and reduced electron scattering (discussed in Section 4.2.2). This makes the method well suited for study of ^{8}B solar neutrinos, which have energies ranging up to 15 MeV as shown in Section 1.2. Cuts were chosen to obtain a near-clean data set of ^{8}B solar neutrinos at high energies.

The first event cut aims to remove high NHit backgrounds and their followers, primarily removing muons and detector breakdowns. This was done by cutting any event with a cleaned NHit $>$ 5000, and then implementing a 20 s dead time afterwards.

The next cut removed events that didn't pass the basic Data Cleaning analysis mask. This mask was used for all data sets, and includes the following, as defined by the RAT User Manual [132] and documentation from the Water Phase [133]:

- zerozerocut - Tags every event where the last two hex digits of the GTID are zero. This cut is required because of a rollover issue with the Global Trigger that creates orphan hits with bad GTIDs that end in 00 [132].
- owlcut - Tags events with three or more hits on the outward looking tubes [133].

- junkcut - Tags any event where a channel has more than one triggered hit, which should not be physically possible [132].

- pollingcut - The DAQ system has a few different measurements that are done on a run by run basis. During those measurements the hardware can have an increased amount of noise. This cut will tag all events during those time periods [132].

- missingcaendata - The shape of the some trigger signals are stored over an event [133]. This cut tags events with this data missing. This occurs when the CAEN buffer fills before the data can be read out.

The next cut selects only events that are successfully reconstructed using partialFitter (as described in Section 3.4) and contain valid position and time values.

Next, events with a clean NHit cut of < 1500 are removed — approximately equivalent to a 5 MeV cut based on the scaling of $\sim$300 NHit/MeV. This cut is the main background rejection method in this analysis, as there are negligible backgrounds expected above 5 MeV in the detector, leaving a very clean sample of ^{8}B ν_e and ν_μ events. Possible backgrounds at this energy include atmospheric neutrinos and ^{208}Tl decays. By using rates determined for the solar flux analysis in Period 1 [134], these backgrounds are expected to contribute $\sim$1 event in the total data set.

A radius cut of $r < 5.5$ m from the centre of the AV was enforced to reduce the effect of the optical mis-modelling near the AV while maintaining a large fiducial volume. In Period 1, an additional position cut of $z > 1$ m was also applied to remove events that mis-reconstruct near the water-scintillator interface, where the reconstruction performance is reduced.

After these cuts were enforced, 20 events were selected from Period 1 and 17 events were selected from Period 2.

4.4 Application to Data, Analysis, and Results

In this section, the reconstruction of direction will be applied to the events selected in Section 4.3. The reconstruction algorithm can only be used on electrons, rather than the ^{8}B solar neutrinos themselves. The angular dependance of neutrino-electron scattering is investigated and the impact on the ability to reconstruct neutrino direction is determined. The results of direction reconstruction in Periods 1 and 2 are then presented and analysed for significance.

4.4.1 Neutrino-Electron Scattering

While discussing the effectiveness of direction reconstruction in previous sections, results have been shown by comparing the reconstructed direction against true electron direction. However, in a neutrino physics analysis, the desired information is the incoming direction of the neutrino. In the ^{8}B solar neutrino data set, it will only be possible to compare a reconstructed direction to the solar direction. As such, the parameters $\theta_{\nu\text{-}e}$ and θ_{sun} are defined as in Figure 4.19.

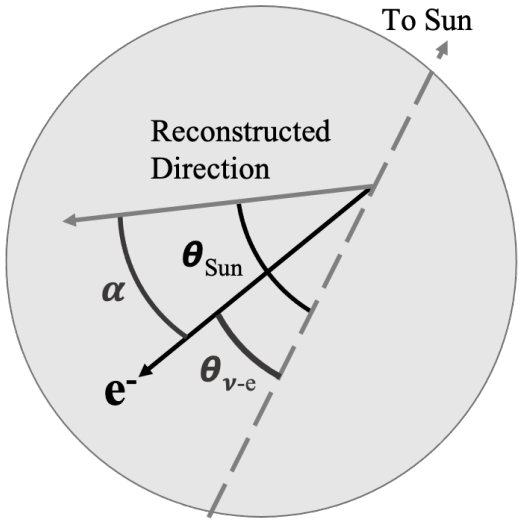


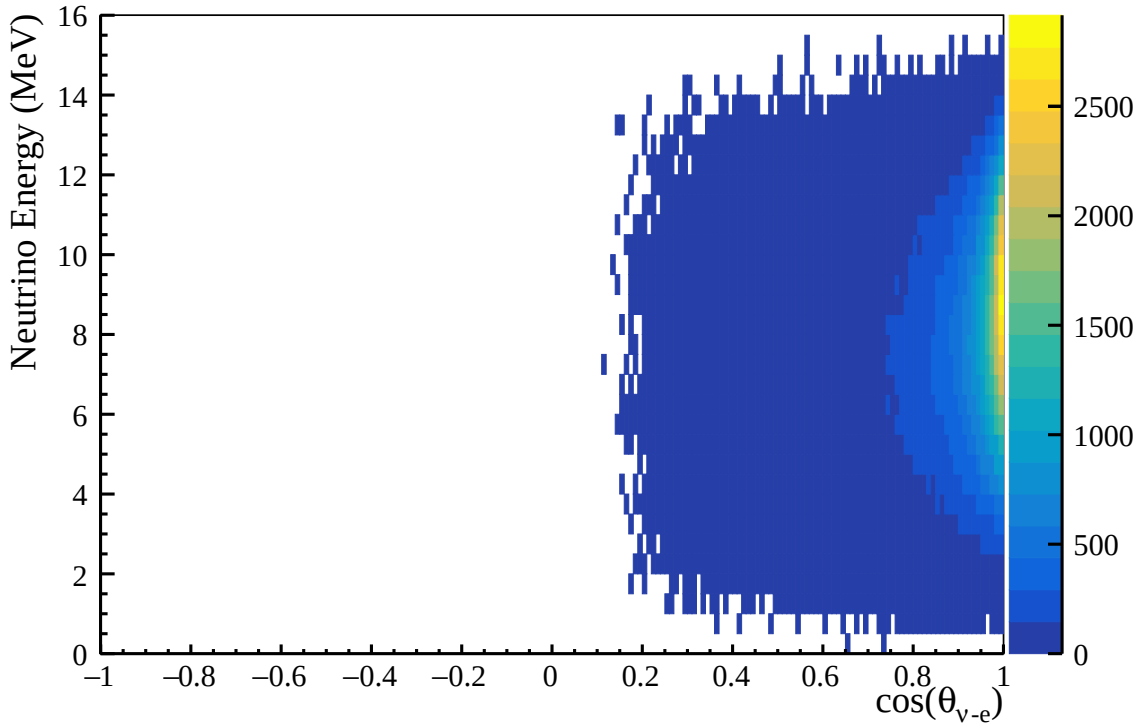
Figure 4.19: Diagram showing the relationship between the angles α, $\theta_{\nu\text{-}e}$ and θ_{sun}. α is the angle between the true and reconstructed electron direction. $\theta_{\nu\text{-}e}$ is the scattering angle between the neutrino and the electron. θ_{sun} is the angle between the reconstructed electron direction and the solar direction.

The measurable parameter is θ_{sun}, where the reconstructed direction is compared to the solar direction, which is calculated based on the reconstructed event time. In order to determine whether neutrino-electron scattering will be a significant effect on the ability to reconstruct direction, the parameter $\theta_{\nu\text{-}e}$ must be investigated. Neutrino-electron elastic scattering is discussed in Section 1.1.4, where it is shown that outgoing electron direction is kinematically determined by the incoming energy of the neutrino and the outgoing energy of the electron (Equation 1.1.11). This can be rearranged as in Equation 4.4.1.

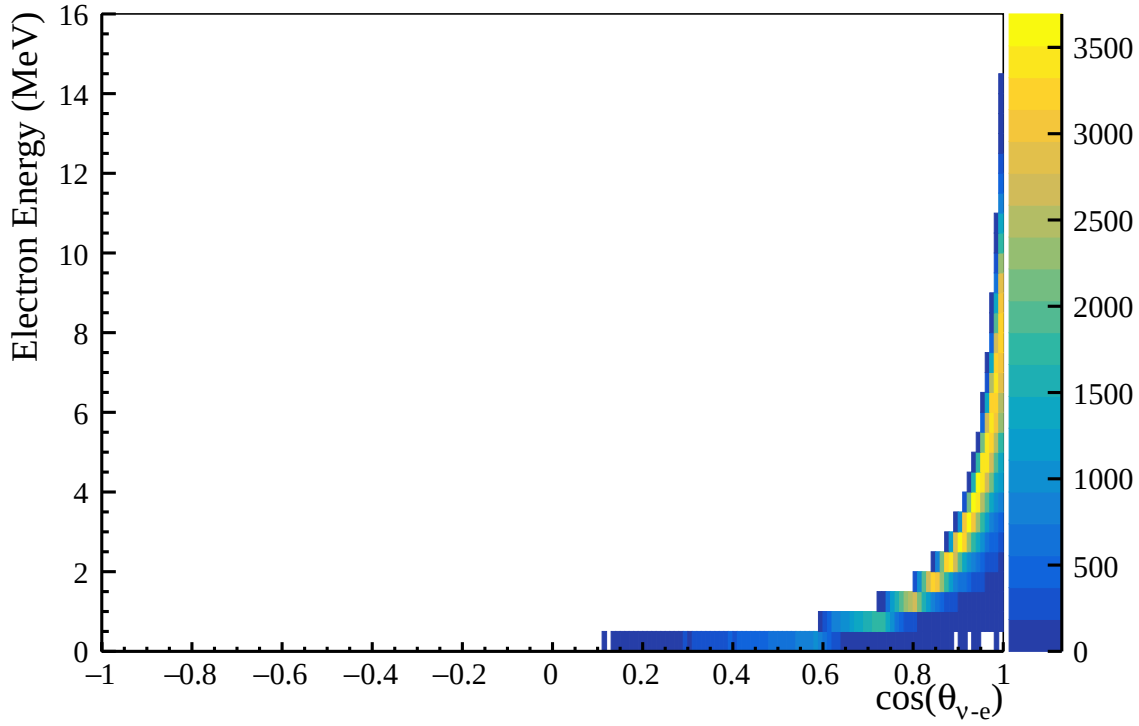
$$\cos(\theta_{\nu-e}) = \sqrt{\frac{T_e(m_e + E_\nu)^2}{2m_e E_\nu^2 + T_e E_\nu^2}} \tag{4.4.1}$$

Where T_e is the outgoing kinetic energy of the electron, E_v is the incoming energy of the neutrino, and m_e is the mass of the electron. By combining this with the differential cross section, it is possible to generate a distribution in $\cos(\theta_{\nu\text{-}e})$ against both the energy of the incoming neutrino and the outgoing energy of the scattered elecron. These distributions were created using MC simulations of ^{8}B ν_e interactions in the SNO+ detector, using the MC truth values for particle energies and directions. This can be seen in Figure 4.20.

It can be see that there is little relation between the neutrino incoming energy and the scattering angle. However, there is a significant dependance on outgoing electron energy for the scattering angle. Kinematically, electron recoils with an energy close to the incoming energy of the neutrino will be more forward scattered. This means that when selecting events with a high NHit — and as such, only selecting high energy electrons — only events with a small scattering angle are selected. To demonstrate this, $\cos(\theta_{\nu\text{-}e})$ is plotted for all events in the Period 1 MC simulation that pass the event selection criteria detailed in Section 4.3.1, including an NHit cut removing events with NHit$<$1500. The results of this can be seen in Figure 4.21.



(a) Incoming Neutrino Energy



(b) Outgoing Electron Energy

Figure 4.20: Demonstration of the neutrino-electron scattering angle for simulated ^{8}B neutrinos. While neutrinos across the ^{8}B energy spectrum can have wide scattering angles, reaching beyond $\cos(\theta_{\nu\text{-}e}) = 0.2$ as shown in (a), this angle is dependent on the energy of the scattered particle. This leads to the shape seen in (b), where only electrons below 2 MeV have $\cos(\theta_{\nu\text{-}e}) < 0.8$.

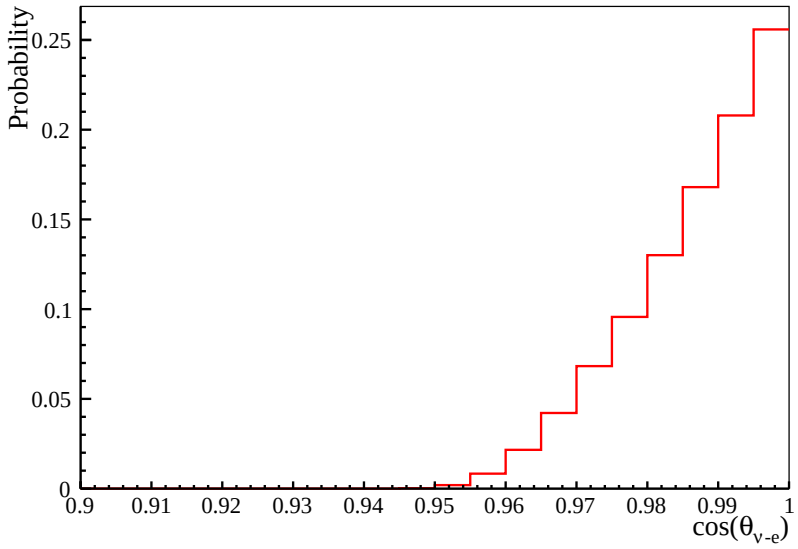


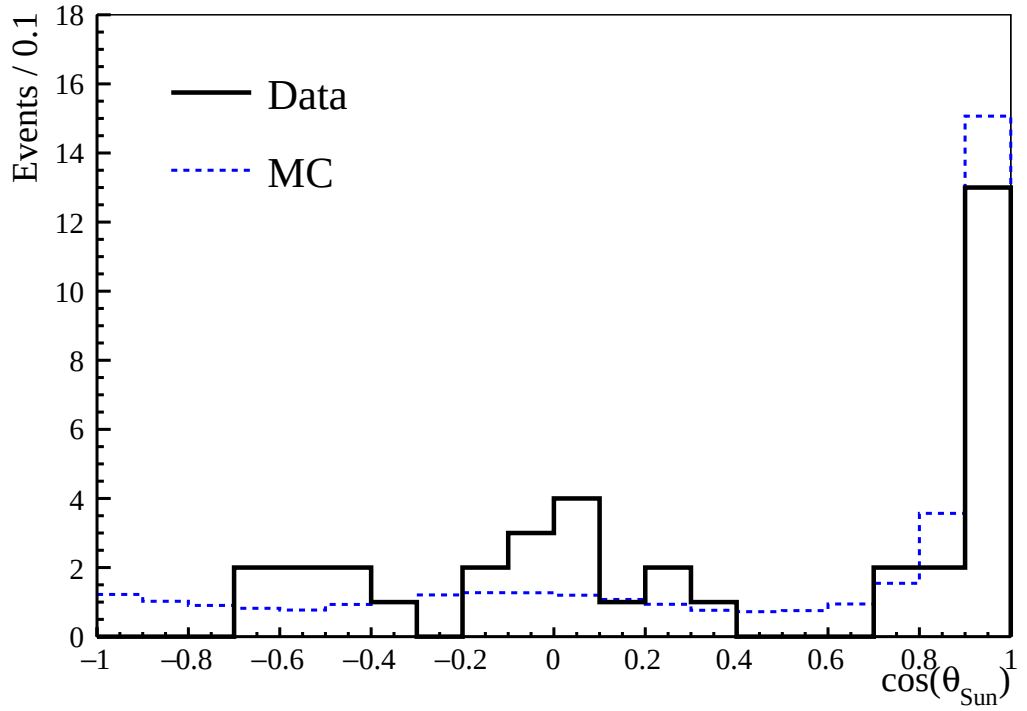
Figure 4.21: Neutrino-electron scattering angle $\cos(\theta_{\nu\text{-}e})$, plotted for simulated ^{8}B solar ν_e events that pass event selection criteria. Due to the removal of low energy electron events, all events scatter with $\cos(\theta_{\nu\text{-}e}) > 0.95$.

For the selected events, all are scattered with $\cos(\theta_{\nu\text{-}e}) > 0.95$. To ensure this is a subdominant effect, $\cos(\theta_{sun})$ bins of width 0.1 will be used in data.

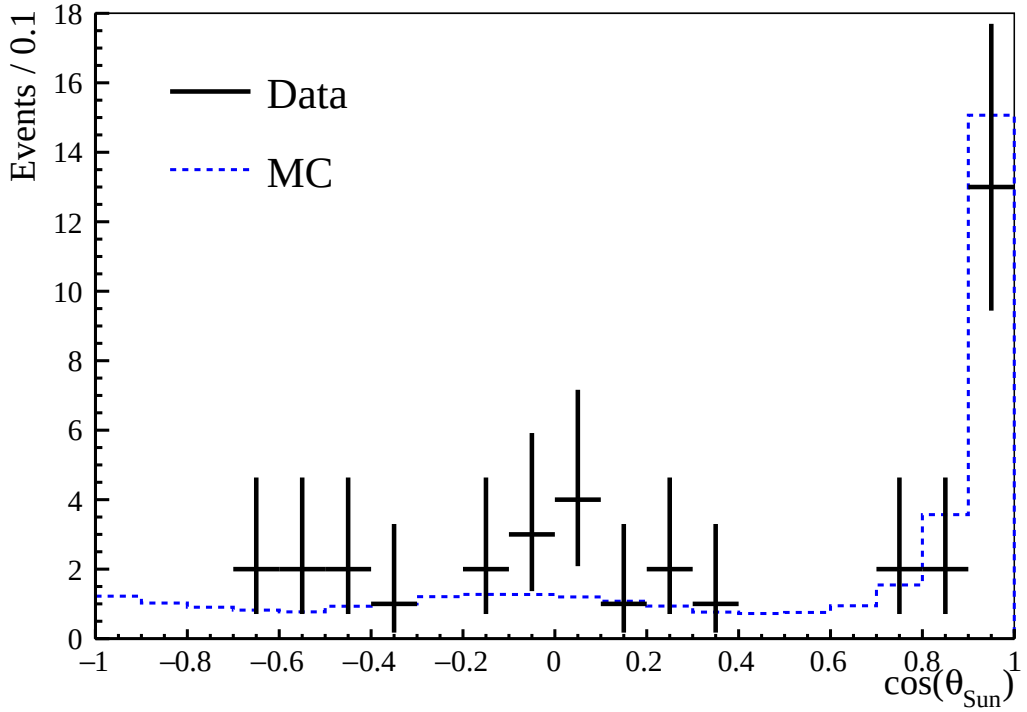
4.4.2 Results in Data

The direction reconstruction described in Section 4.1 was applied to the events selected in Section 4.3. The results for Period 1 and 2 are combined into a single dataset, as the same scintillator cocktail was present for both. The results of this can be seen in Figure 4.22. The MC expectation was generated from simulated ^{8}B interactions across the run-lists of Periods 1 and 2. It has been normalised to 37 — the number of events in the data set.

A clear forward peak is observable, with 15 out of 37 (40.5%) events reconstructing with $\cos(\theta_{sun}) > 0.8$. Results are presented both with and without errors bars for ease of viewing. This data set is highly statistics limited, and therefore uncertainties can be assumed to be entirely Poissonian. Within these Poissonian uncertainties, the data matches the MC prediction well and provides a significant motivation to further study into directionality in scintillators.



(a)



(b)

Figure 4.22: Results for directional reconstruction in SNO+ data, with a simulated MC expectation for comparison. Dataset includes Periods 1 and 2. A clear forward peak is seen, corresponding to the solar direction. Results are presented with (b) and without (a) Poissonian uncertainties.

4.4.3 Analysis

In order to quantify the significance of these results, a binned log likelihood ratio was computed. The null hypothesis (H_0) assumed a flat distribution (i.e. each bin contained N/B events, where $N = 37$ is the number of events in the histogram, and $B = 20$ is the number of bins). This was compared to the alternative hypothesis (H_1) of the directional MC simulation seen in Figure 4.22.

Although there are only a small number of events, the significance can be approximated using Wilk's theorem. Defining the binned likelihoods as:

$$\log(\mathcal{L}_i) = \sum_{b=1}^{20} n_b \log\left(p_{H_i,b}\right) \tag{4.4.2}$$

where n_b is the number of data points in bin b, and $p_{H_i,b}$ is the probability of the given hypothesis in that bin. Wilk's theorem [135] states that, for a large sample:

$$-2\log\left(\frac{\mathcal{L}_0}{\mathcal{L}_1}\right) \approx \chi^2 \tag{4.4.3}$$

It can be further shown that for a Poisson distribution, this relationship holds well even for small sample sets [136]. As a χ^2 distribution with 1 degree of freedom is distributed as a normal distribution squared, the number of standard deviations away from H_0 can be represented as:

$$\sqrt{-2\log(\frac{\mathcal{L}_0}{\mathcal{L}_1})} \tag{4.4.4}$$

This quantifies the significance of the data set against an isotropic H_0. By applying these equations, the data set shown in Figure 4.22 has:

$$-2\log\left(\frac{\mathcal{L}_0}{\mathcal{L}_1}\right) = 32.9113 \tag{4.4.5}$$

which leads to a significance of 5.73σ away from H_0. This can be verified by gen-

erating samples of 37 randomly distributed values in $\cos(\theta_{sun})$ and calculating the likelihood ratio for each set. The distribution of $-2\log\left(\frac{\mathcal{L}_0}{\mathcal{L}_1}\right)$ will show the significance of the value obtained for this data set. This distribution, generated for 10^{12} samples, can be seen in Figure 4.23.

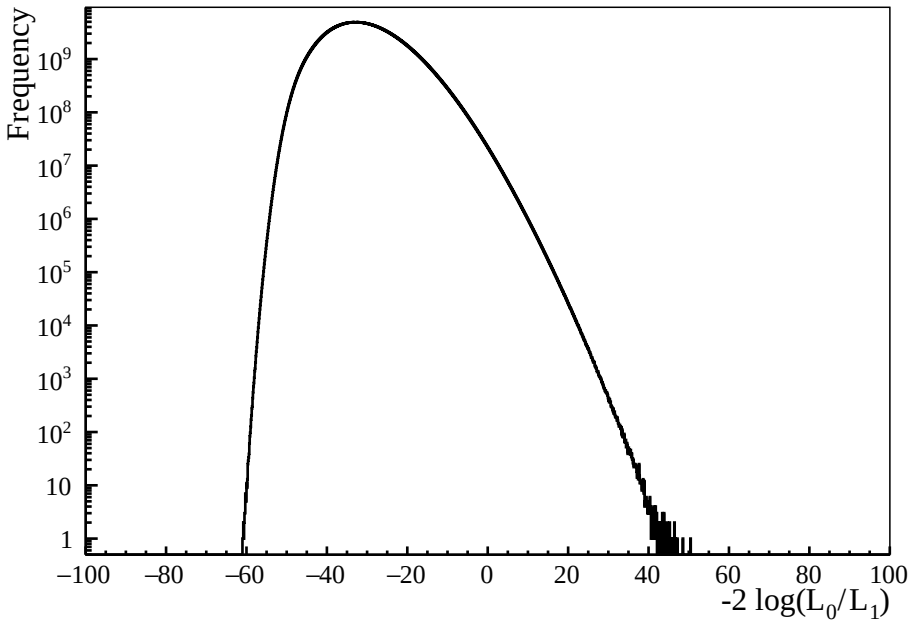


Figure 4.23: Distribution of $-2\log\left(\frac{\mathcal{L}_0}{\mathcal{L}_1}\right)$ for randomly generated samples of 37 events. It can be seen that the distribution is not a perfect Gaussian.

It can be seen that the distribution is not a perfect Gaussian, due to the small size of the samples. Out of the 10^{12} samples, 2769 had a calculated $-2\log\left(\frac{\mathcal{L}_0}{\mathcal{L}_1}\right) \geq 32.9113$. This indicates that the probability of the result shown here being a fluctuation from a uniform distribution is 2.769×10^{-9}, the equivalent of a significance of 5.83σ. This is slightly higher than the estimated significance from Wilk's theorem due to the non-Gaussian nature of the small sample.

This significance shows that there is a definite demonstration of event-by-event directionality in this dataset. This is the first such demonstration in a large-scale high-yield LS detector.

4.5 Conclusions

A method of direction reconstruction in large-scale LS neutrino detectors has been demonstrated to be effective using data from the SNO+ detector. The method relies on the time separation of Cherenkov and scintillation light. As a lower concentration of PPO in LAB creates a slower scintillation profile, data was selected from the experimental phases of SNO+ that contained 0.6 g/L PPO, with corresponding MC simulation used for the creation and testing of a direction reconstruction algorithm.

By examining detected photons in simulation using the time residual and angular information, it is possible to see clear anisotropy on the rising edge of the scintillation profile. It is then possible to use this information to reconstruct direction using a maximal likelihood method. This method was tested using several electron energies, showing that higher energies (>6 MeV) display good directionality with $> 45\%$ of events reconstructing with $\cos(\alpha) > 0.8$, where α is the difference in angle of the reconstructed and true electron direction.

A bias in position reconstruction, known as drive, is found along the direction of motion of the moving electron. The effect of drive causes a double peak structure in the PDF used for direction reconstruction, leading to a small degeneracy in the likelihood space. This appears as a tail structure of the reconstructed direction with peaks around $\cos(\alpha) \approx 0$ and $\cos(\alpha) = -1$. It is shown that this structure disappears if direction reconstruction is done using the true MC vertex position and time. Using 6 MeV electrons, the percentage of events that reconstruct with $\cos(\alpha) > 0.8$ is increased from 45.6% to 77.4% when the true position is used. This motivates further study into improvements of the position-time reconstruction with the inclusion of the directional component.

The effect of electron multiple scattering causes a smearing effect in directional reconstruction. This is caused by two effects: the average direction of

travel for the electron differing from the initial direction, and the smearing of the Cherenkov ring as the travel direction changes with each scatter. This effect is more significant at lower energies. It can be shown that removing the process of multiple scattering from simulations increases the percentage of 6 MeV events that reconstruct with $\cos(\alpha) > 0.8$ from 45.6% to 84.0%. This effect is irreducible in SNO+, but motivates the use of higher energy events. Lower energy events may require different techniques and/or higher light collection to extract usable directionality.

The use of direction reconstruction in data requires the transformation from the electron direction to the neutrino direction, assumed to be the Solar direction. While there is a distribution of angles in neutrino-electron elastic scattering that ranges down beyond $\cos(\theta_{\nu\text{-}e}) = 0.2$, where $\theta_{\nu\text{-}e}$ is the angle of scatter between the electron and the neutrino, the angle of scattering is dependent on the energy of the scattered particle. For electrons with energies above 5 MeV the angle of scatter is small, with $\cos(\theta_{\nu\text{-}e}) > 0.95$ for all events selected for the high energy dataset used in this analysis. This constrains the precision used when investigating data, and $\cos(\theta_{sun})$ bins of size 0.1 were chosen for this reason.

Application of direction reconstruction to data shows directional detection of neutrinos with a significance of 5.83σ. This demonstrates the possibility of reconstructing direction on an event-by-event basis in a large-scale high-yield LS neutrino detector, and opens up significant possibilities in the field of neutrino physics. The ability to combine high-precision energy reconstruction with directionality could lead to improved background rejection for studies such as $0\nu\beta\beta$ searches. However, there are multiple avenues for further study that must be explored before this will be possible, as these searches occur at low energies, where direction reconstruction using this method becomes less effective.

Chapter 5

Future Directions

"Let's think the unthinkable, let's do the undoable. Let us prepare to grapple with the ineffable itself, and see if we may not eff it after all."

- Dirk Gently's Holistic Detective Agency, Douglas Adams

The results presented in Chapter 4 demonstrate the first event-by-event directional reconstruction in a high-yield liquid scintillator detector. However, the investigation also highlighted areas of potential improvement for directionality, most notably the accuracy of position reconstruction and the capabilities of photon sampling. Potential methods for improving these two areas will be explored in this chapter.

As seen in Figure 4.11, there is a significant bias in position reconstruction along the direction of motion of an electron within the SNO+ detector. Subsection 4.2.1 explored the potential improvements to direction reconstruction that would be possible with perfect position-time reconstruction. This leads to the observation that direction reconstruction could reduce the bias of position reconstruction, and that improved position reconstruction could in turn lead to a more effective direction reconstruction. A combined direction-position reconstruction algorithm would have the potential of improving both of these reconstructed parameters. A method for this is presented in Section 5.1, and the limitations in the SNO+ experiment are explored.

The impact of electron multiple scattering was shown in Section 4.2.2. The ability to reconstruct direction is reduced due to the blurring of the Cherenkov

ring as the electron changes direction through scattering. This effect could be reduced by improving the photon sampling. Using modern PMTs would achieve this, as upgrades to PMT technology have led to both faster timing and high quantum efficiencies. To show the impact of improved PMTs in directionality, the SNO+ experiment is simulated with Hamamatsu R5912 PMTs, and the direction reconstruction methods described in Chapter 4 are used. The results of this investigation are shown in Section 5.2.

5.1 Combined Direction-Position Reconstruction

Direction and position reconstruction are highly interdependent, as shown by the investigations in Section 4.2.1. The drive bias found in position reconstruction occurs along the direction of motion of the electron due to the early timing of the directional Cherenkov light. The inaccuracies in position reconstruction have a negative effect on the ability to reconstruct direction, causing an unusual tail structure. In this section, a potential method of simultaneous direction-position reconstruction is described and the limitations within SNO+ are discussed. Additionally, a method of drive correction is suggested for the improvement of position reconstruction using directional information.

5.1.1 Simultaneous Direction-Position Reconstruction

As position and direction reconstruction are inherently connected, a simultaneous reconstruction of both parameters was attempted using a maximum likelihood method. For this reconstruction, the 2D PDF calculated using the true vertex parameters (Figure 4.5) was used. However, unlike in direction-only reconstruction, the entire t_{res} range of -100–300 ns was kept in order to maintain good performance in the position reconstruction. To remove the possibility of a bin with a probability of 0 in the PDF (which would cause the log-likelihood sum in Equation 4.1.1 to become invalid), the PDF was extrapolated as flat in

the ranges $t_{res} < -20\,\text{ns}$ and $t_{res} > 234\,\text{ns}$. The time residual projection of the resulting PDF can be seen in Figure 5.1.

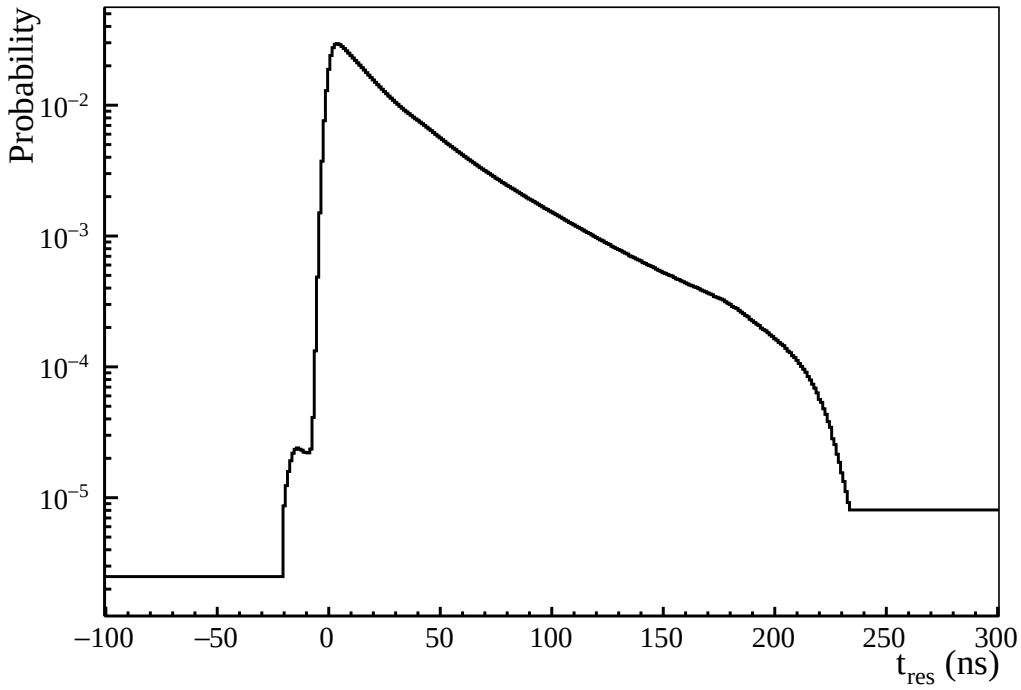


Figure 5.1: A projection along the t_{res} axis of the 2D PDF used for simultaneous direction-position reconstruction. The plot is shown logarithmically in order to demonstrate the flat-probability extrapolations performed for the ranges $t_{res} < -20\,\text{ns}$ and $t_{res} > 234\,\text{ns}$, which removed the possibility of bins with a 0 probability in the PDF.

Given the size of the detector and the fact that there are six parameters to reconstruct (time, position(x,y,z), direction(θ,γ)), the run time of a simple grid optimisation algorithm over the entire phase space would be unusable. Therefore, adjustments were made that would reduce the number of points tested in the maximum likelihood search and as such reduce the time taken to reconstruct an event.

Position reconstruction is desired to have a granularity on the order of cm. As the AV has a diameter of 12 m, it would not be reasonable to examine the entire volume at this granularity. Instead, the range of the position parameters required for the optimisation was reduced by using the originally reconstructed position-time vertex (using the multiPDF algorithm described in Section 3.4) as

a seed. The optimiser was then set to search in a range around that position and time. A range of ± 600 mm for each position parameter and ± 10 ns for time was chosen.

The grid optimisation algorithm used in direction-only reconstruction provided a desirable robustness against local minima, which is even more vital with more parameters added to optimise over. In order to retain some of the robustness of the grid fitting while reducing the time taken, an optimiser known as "adaptive grid" was used. In this optimiser, a coarse grid search was done over all directions and the position-time range described above. When the maximum likelihood point was found (using Equation 4.1.1 and the PDF), this new vertex was then taken as a seed for a smaller, finer grid search, with a step size equal to the desired reconstruction granularity. The parameters of both grids can be tuned. This method means a finer granularity can be achieved while still searching a large area, without running into constraints on the run time. A simplified visualisation of this process is provided in Figure 5.2. The parameters of the adaptive grid used for testing are shown in Table 5.1.

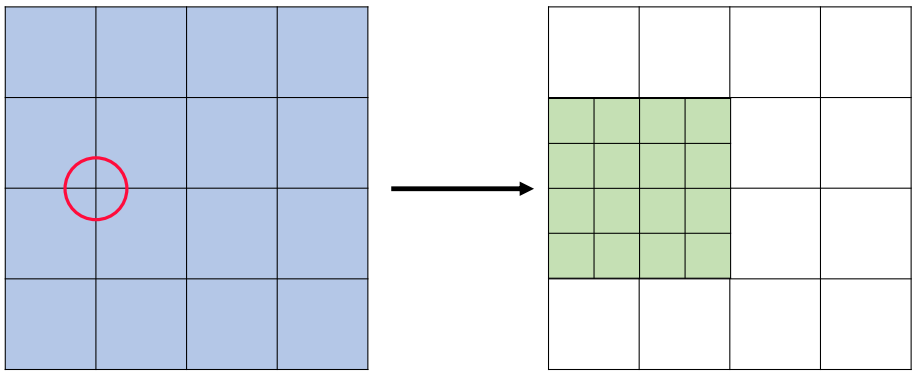


Figure 5.2: A simplified demonstration of the adaptive grid. First, a coarse grid (blue) is searched to find an optimum point (red circle). This point is then taken as the centre of a finer grid (green) to find a new optimum vertex.

The adaptive grid direction-position reconstruction was tested using 6 MeV electrons simulated in the SNO+ detector, assuming perfect conditions. The detector was filled with 0.6 g/L PPO in LAB. The events were simulated at the

Grid 1			
Parameter	Min	Max	Step Size
Position	-600 mm	600 mm	100 mm
Time	-10 ns	10 ns	5 ns
$\cos(\theta)$	-1	1	0.1
ϕ	$-\pi$ rad	π rad	$\frac{\pi}{10}$ rad

Grid 2			
Parameter	Min	Max	Step Size
Position	-100 mm	100 mm	17 mm
Time	-5 ns	5 ns	2.5 ns
$\cos(\theta)$	-0.1	0.1	0.01
ϕ	$-\frac{\pi}{10}$ rad	$\frac{\pi}{10}$ rad	$\frac{\pi}{100}$ rad

Table 5.1: Parameters used in the adaptive grid fitting optimisation algorithm.

centre of the detector with isotropic directions. The centre of the detector was chosen to improve the position reconstruction and create the most isotropic case. For the purposes of initial testing, detector conditions (such as Partial-Fill level or channels being off) were not considered. These results therefore constitute the maximum performance achievable from the algorithm in SNO+.

In order to quantify the performance of the the direction-position reconstruction, three test cases of direction-only reconstruction were created. These test cases each represent direction reconstruction performance for different levels of drive correction. Each test case is defined by a PDF (made using either the reconstructed or MC truth position-time vertex) and a position-time vertex used in the direction reconstruction calculation (required to calculate both $\cos(\theta_\gamma)$ and t_{res}). These are then compared to the accuracy of the direction reconstruction achieved by a simultaneous direction-position reconstruction algorithm. This provides a

quantifiable result for the improvement made in direction reconstruction. The improvement made in position reconstruction can be quantified by investigation of the drive parameter.

The first test case (Test 1) used the PDF created with the reconstructed position-time vertex (Figure 4.6) and used the reconstructed position-time vertex for direction reconstruction calculations. This combination is equivalent to the direction-only reconstruction performed in Chapter 4. The same simulated events were used in this test case as for the direction-position reconstruction described above, leading to a different performance of the algorithm than in the previous chapter. The detector is in a perfect state and so maximum coverage is achieved and all events are simulated at the centre of the AV, leading to the reduction of optical effects near material interfaces for the most isotropic case. This test case represents the direction reconstruction performance achievable without attempting to correct drive. A good direction-position reconstruction should outperform this test case.

The second test case (Test 2) used the PDF created with the MC truth position-time vertex, but used the reconstructed position when performing the direction reconstruction calculations. This represents a "worst case scenario" for direction-position reconstruction, where there is no correction to the drive achieved.

The third test (Test 3) case used the PDF created with the MC truth position-time vertex, and used the MC truth position-time vertex for the direction reconstruction calculations. This is included as a "best case scenario", where the drive has been perfectly corrected (and with no resolution effects on the position). This is the equivalent of the investigation performed in Section 4.2.1, with altered performance as explained for Test 1 due to detector conditions and event placement in the detector. The details of the three test cases are summarised in Table 5.2.

Test Case	Vertex used in PDF	Vertex used in Direction Reconstruction
1	Reconstructed	Reconstructed
2	MC Truth	Reconstructed
3	MC Truth	MC Truth

Test Case	Purpose of Test
1	Equivalent to direction-only reconstruction
2	Equivalent to no drive correction, "worst case"
3	Equivalent to perfect drive correction, "best case"

Table 5.2: A summary of the test cases used for the comparison of direction-position reconstruction. Details include the position-time vertex used for both the creation of the PDF and the direction reconstruction calculations, alongside the purpose of the inclusion of the test.

It is expected that a good drive correction should lead to a direction reconstruction performance between those of Test 1 and Test 3. This would mean an improvement to directionality as compared to a direction-only reconstruction (where the drive is effectively "averaged" over by its inclusion in the PDF). The results of the direction-position reconstruction, alongside the three test cases, can be seen in Figure 5.3, using the α parameter introduced in Chapter 4 (demonstrated in Figure 4.19). As a way to numerically compare the effectiveness of the directionality, the percentage of events that reconstructed with $\cos(\alpha) > 0.8$ for each of the test cases and the direction-position fit are presented in Table 5.3.

It can be seen that the direction-position reconstruction is performing less accurately than the direction-only reconstruction. In order to investigate this, the drive of the direction-position reconstruction is shown in Figure 5.4. The drive is also presented as a function of $\cos(\alpha)$.

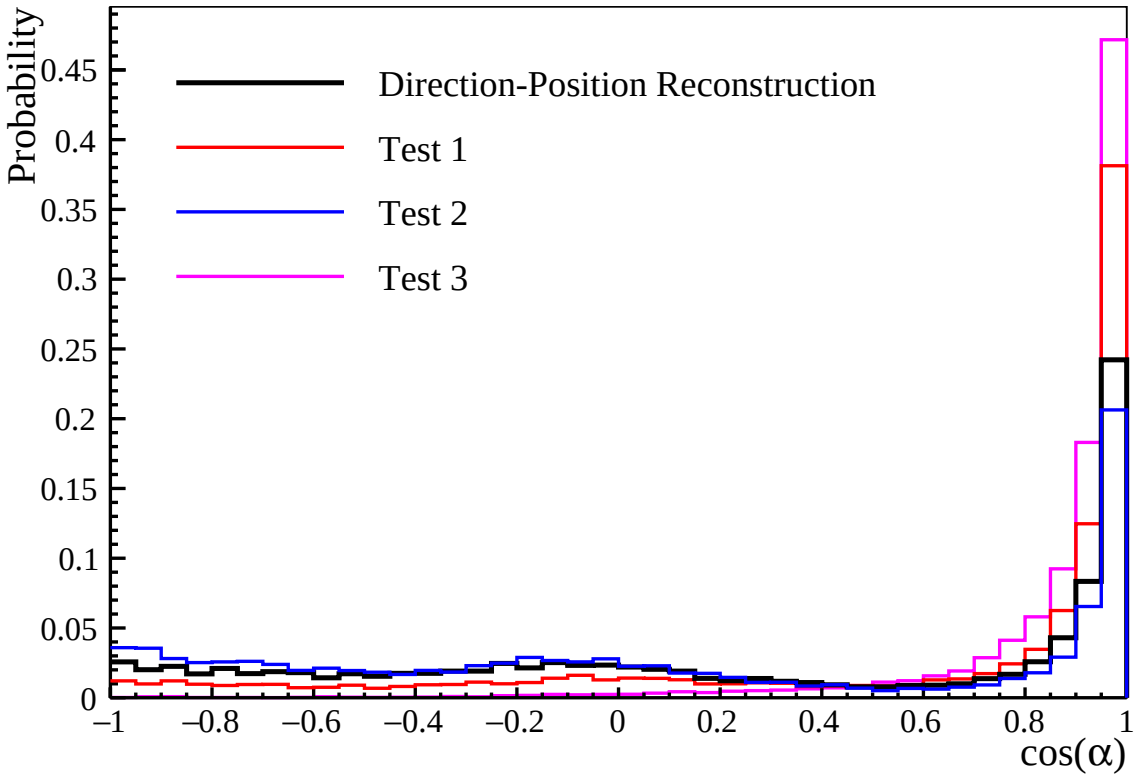
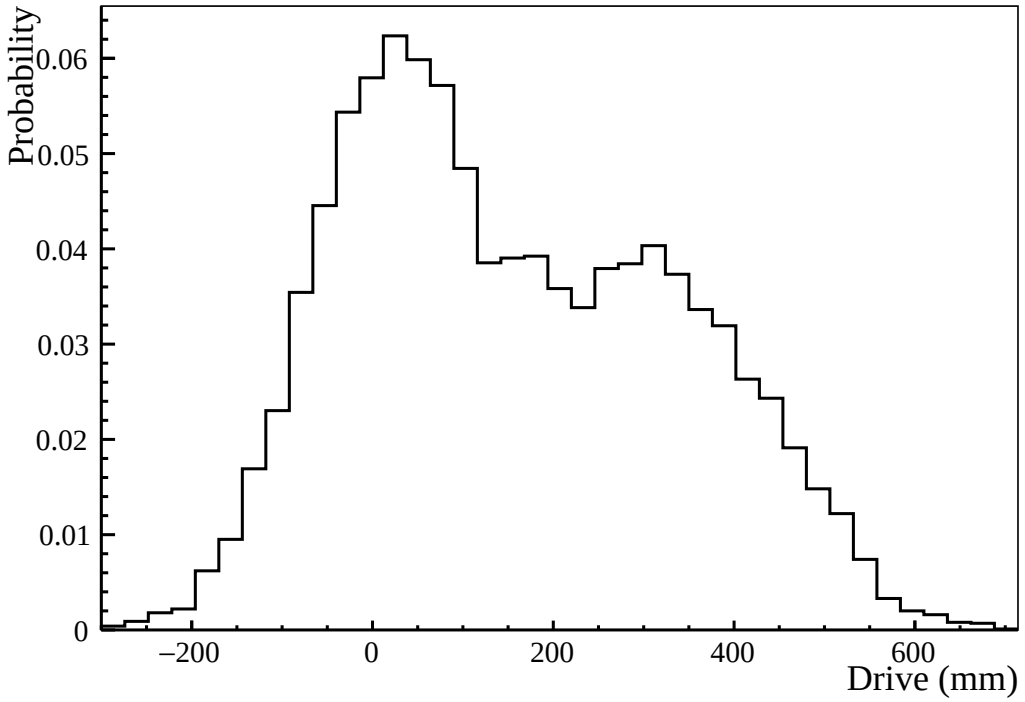


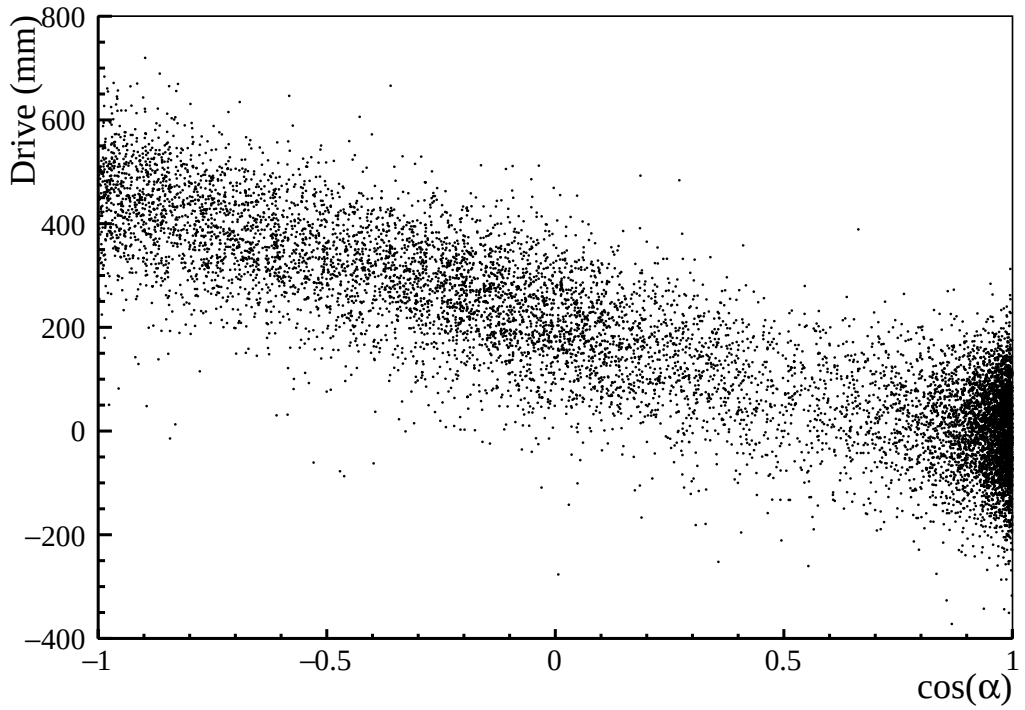
Figure 5.3: The results of the adaptive grid direction-position reconstruction compared to three test cases for 6 MeV electrons. It can be seen that the direction-position reconstruction underperforms when compared to Test 1.

	% with $\cos(\alpha) > 0.8$
Direction-Position	39.4 ± 0.6
Test 1	60.3 ± 0.8
Test 2	31.9 ± 0.6
Test 3	80.5 ± 0.9

Table 5.3: Results of direction-position reconstruction compared to three test cases for 6 MeV electrons. The results are presented as the percentage of events that reconstruct with a $\cos(\alpha) > 0.8$. It can be seen that the direction-position fit performs only slightly better than the "worst case" Test 2 scenario.



(a)



(b)

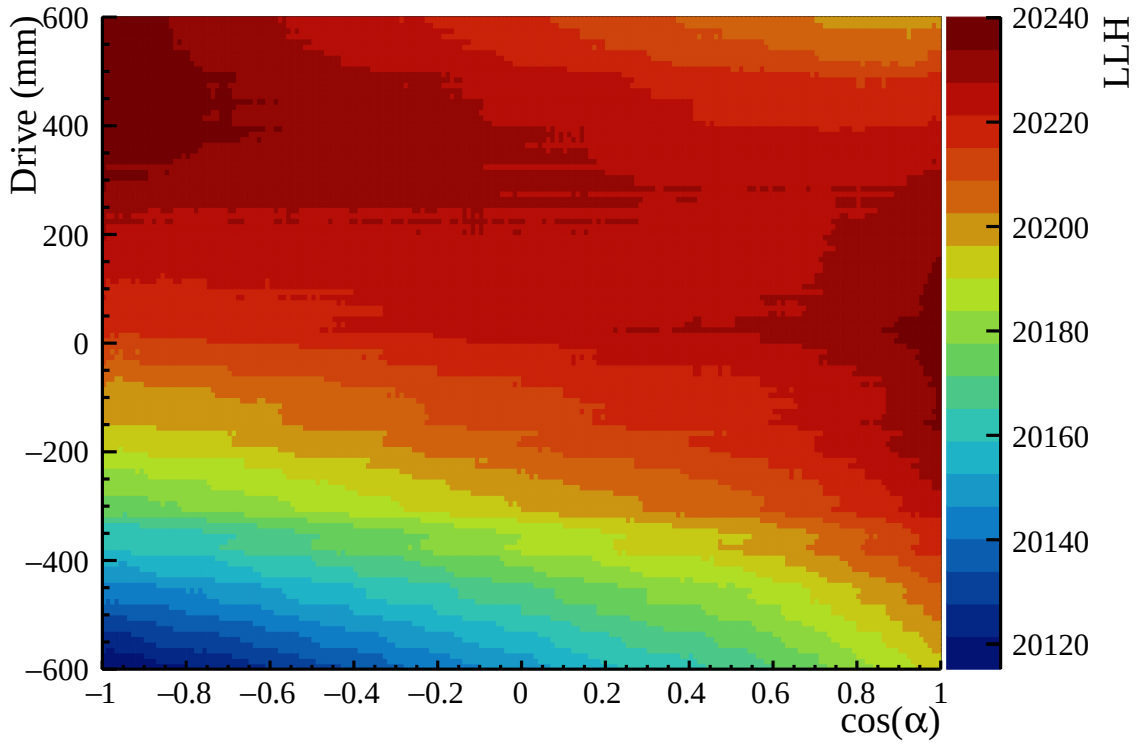
Figure 5.4: The drive of 6 MeV electrons reconstructed with the adaptive grid direction-position fitter. In (a) two peaks can clearly be seen in the drive, one close to 0 mm and one close to 300 mm. In (b), the drive is plotted against the $\cos(\alpha)$ of the reconstructed direction. This plot shows a clear correlation, where events with $\cos(\alpha) \approx 1$ have a drive close to 0 mm, and the drive increases as the reconstructed angle gets further from the truth.

There are two clear peaks in the drive of these events, with one peak $\sim$0 mm and the other $\sim$300 mm. The average drive for 6 MeV electrons using the multiPDF reconstruction algorithm (as described in Section 3.4) is 225.9 ± 0.8 mm. This implies that by using a combined position-direction reconstruction, a significant portion of events are increasing in drive.

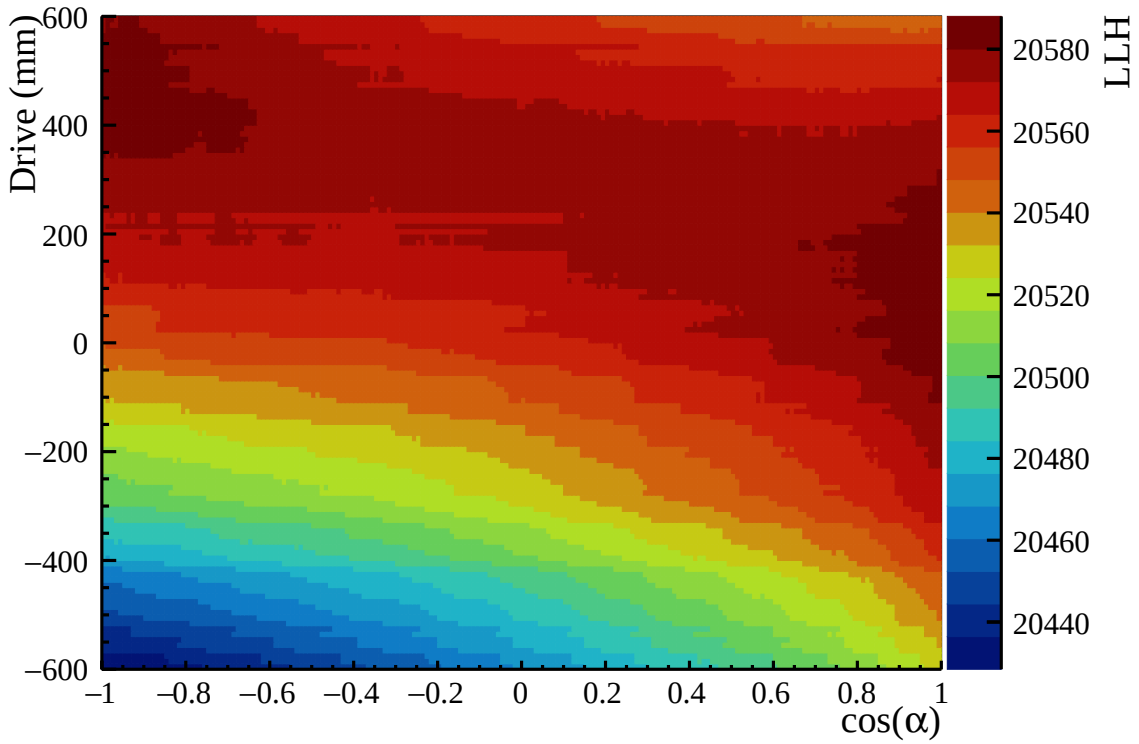
The reason for this can be seen in Figure 5.4b. The drive is heavily correlated with mis-reconstruction of direction, as expected by the interdependence of the parameters. This is explained by the shape of the likelihood space, demonstrated in Figure 5.5 for two events, where the value of the log-likelihood is plotted against $\cos(\alpha)$ and drive. The space has a saddle shape with two maxima. At one maximum, the drive is close to 0, and $\cos(\alpha)$ is close to 1. At the other, the drive is $\sim$500 mm and $\cos(\alpha)$ is close to -1. The values at these maxima are very close, meaning there is an almost equivalent likelihood of the two positions.

The shape of the likelihood space leads to two categories of events. The first are "good-fit", with an average drive close to 0 mm and a reconstructed direction close to $\cos(\alpha) = 1$. The second are "bad-fit" events, for which the average drive increases as $\cos(\alpha)$ gets further from one. For the "bad-fit" events, the reconstruction performance is on average worse than the original position-only and direction-only reconstructions separately. This can be demonstrated by plotting the reconstructed direction separately for events in the "good-fit" and "bad-fit" categories. A cut is placed at 200 mm, as the minimum between the two peaks in Figure 5.4a. A comparison of these two categories of events to the three test cases is shown in Figure 5.6.

It can be seen that the "good-fit" events outperform Test 1 — the equivalent of direction-only reconstruction — with $64.6 \pm 1.0\%$ of events reconstructing with $\cos(\alpha) > 0.8$. However, the "bad-fit" events reconstruct against the true direction, performing worse than isotropically (and with only $0.8 \pm 0.1\%$ of events reconstructing with $\cos(\alpha) > 0.8$).



(a) "Good-Fit" Event



(b) "Bad-Fit" Event

Figure 5.5: The LLH space of two events, showing the correlation between drive and $\cos(\alpha)$. The event mapped in (a) is classified as a "good-fit" event, with a $\cos(\alpha) \approx 1$ and a drive close to 0 mm. The event mapped in (b) is classified as a "bad-fit" event, with a $\cos(\alpha) \approx -1$ and a drive close to 500 mm.

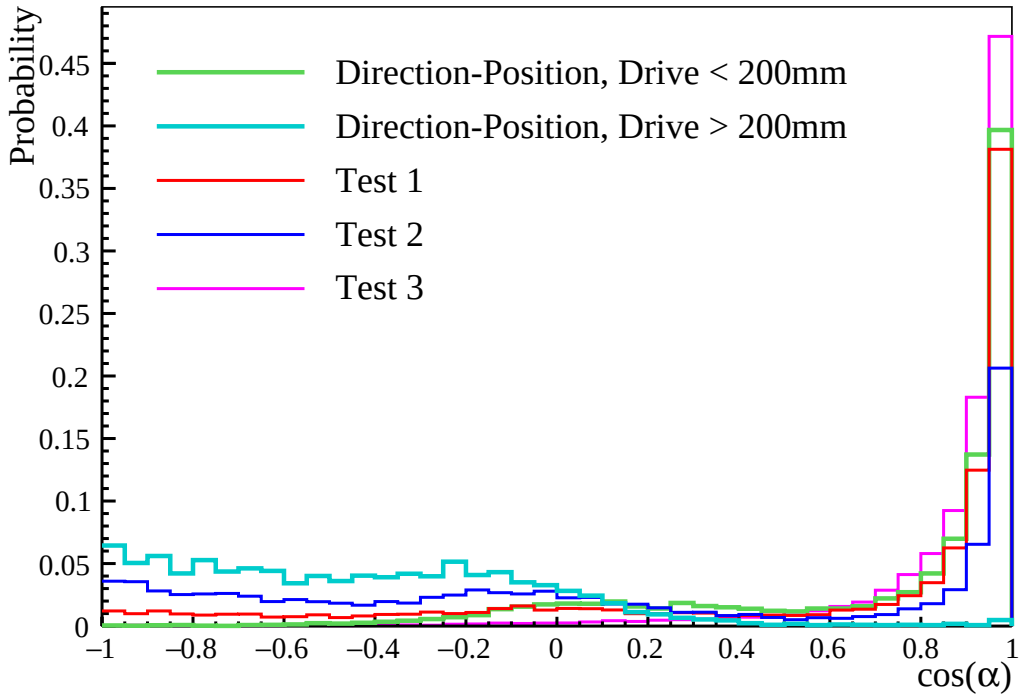


Figure 5.6: The results of the adaptive grid direction-position reconstruction for 6 MeV electrons, with events plotted separately with a drive cut, creating categories for "good-fit" (drive $<$ 200 mm) and "bad-fit" (drive $>$ 200 mm) events. The results are again compared to three test cases. It can be seen that the "good-fit" events reconstruct with a performance better than that of Test 1. However the "bad-fit" events reconstruct with a preference for the backwards direction.

The existence of these two categories implies there are insufficient Cherenkov photons and too sparse photon sampling for this likelihood maximisation to be consistently effective. There are similar numbers of events present in each category for 6 MeV electrons, with 55% of events in the "good-fit" category. However, at higher energies where there are more Cherenkov photons available, this proportion changes. Results for simultaneous direction-position reconstruction for electrons of energy 10 MeV can be seen in Figure 5.7. The three test cases are also included for comparison of direction reconstruction, and the percentages of events reconstructing with $\cos(\alpha) > 0.8$ can be seen in Table 5.4. The direction-position reconstruction still underperforms compared to direction-only (Test 1), but in this case, 70% of events reconstructed with a drive $<$200 mm. This shows that more Cherenkov photons allows for a more reliable correction of drive.

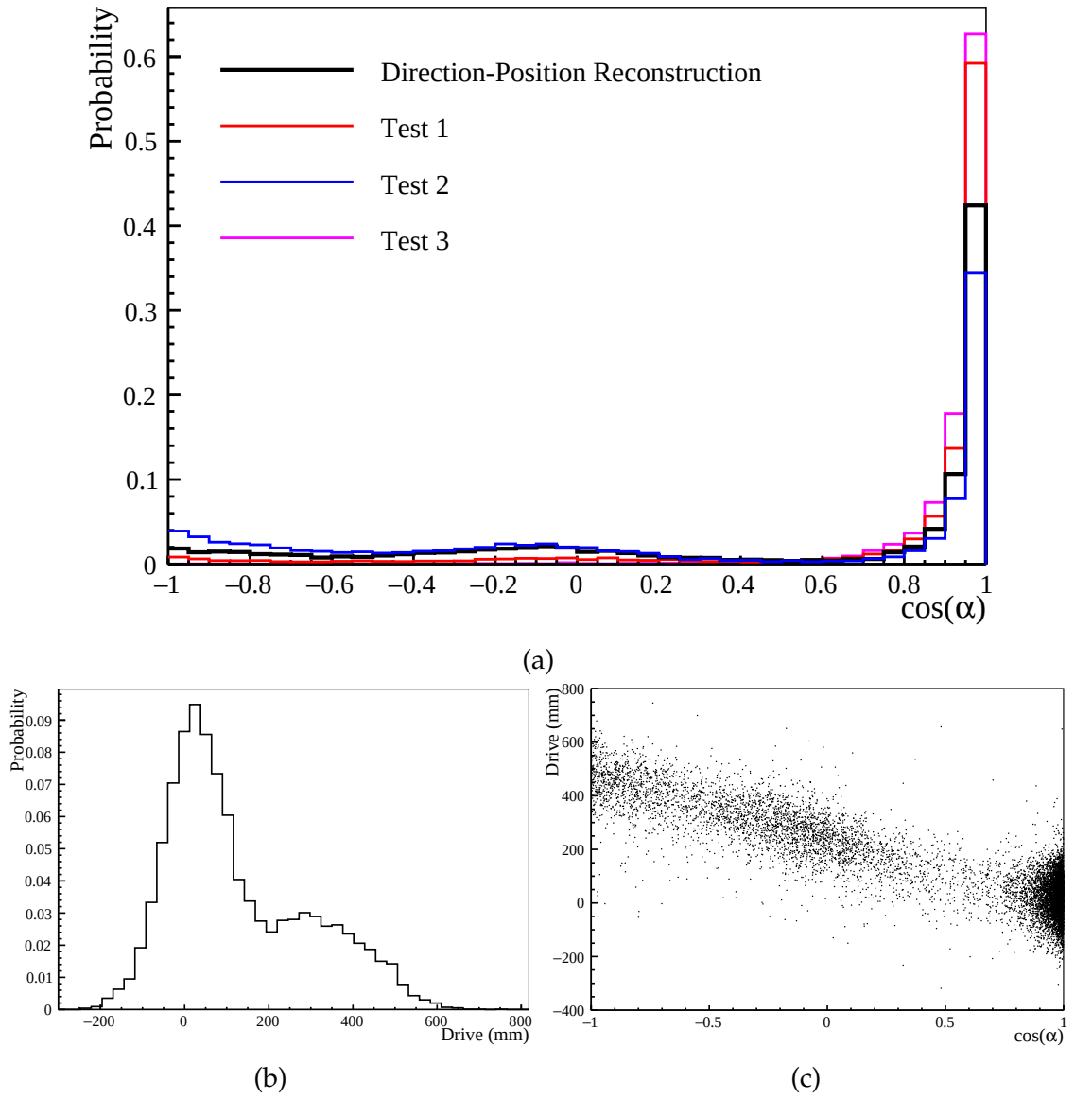


Figure 5.7: Results of simultaneous direction-position reconstruction for 10 MeV electrons. The direction-position reconstruction underperforms when compared to direction-only (Test 1). However, it can be seen that more events are reconstructing with the correct position than at 6 MeV.

The inclusion of a position parameter in the reconstruction has created a case where an inaccurate reconstruction of either the position or direction parameter negatively impacts the reconstruction of the other parameter. Further investigation is ongoing on this reconstruction method, and improved photon sampling may allow for a more reliable result. This method is showing potential, as good-fit events have a significant decrease in drive. However, it is clear improvements

	% with $\cos(\alpha) > 0.8$
Direction-Position	59.3 ± 0.8
Test 1	81.5 ± 0.9
Test 2	46.7 ± 0.7
Test 3	91.4 ± 1.0

Table 5.4: Results of direction-position reconstruction compared to three test cases for 10 MeV electrons. The results are presented as the percentage of events that reconstruct with a $\cos(\alpha) > 0.8$.

need to be made for the direction reconstruction performance to become comparable to a direction-only method.

5.1.2 Flat Drive Correction

While a simultaneous reconstruction does not consistently improve the direction-position vertex, it is still possible that directional information could be used to improve the biases in position. This is attempted using the "flat correction" method.

First, an initial position-time vertex is reconstructed using the multiPDF method described in Section 3.4. Next, an initial direction is reconstructed using the method described in Chapter 4, where the PDF is created using a reconstructed position vertex. Next, the reconstructed position is corrected using the "flat correction" described in Equation 5.1.1.

$$\vec{r}_{new} = \vec{r}_{old} - D_{ave}.\hat{v}_{recon} \tag{5.1.1}$$

where $\vec{r}_{old}$ is the original reconstructed position, D_{ave} is the average drive at the given energy, and $\hat{v}_{recon}$ is the unit vector of the reconstructed direction of the event. For the purposes of this thesis, electrons with energies of 2 MeV, 6 MeV and 10 MeV are considered. Using the multiPDF position reconstruction al-

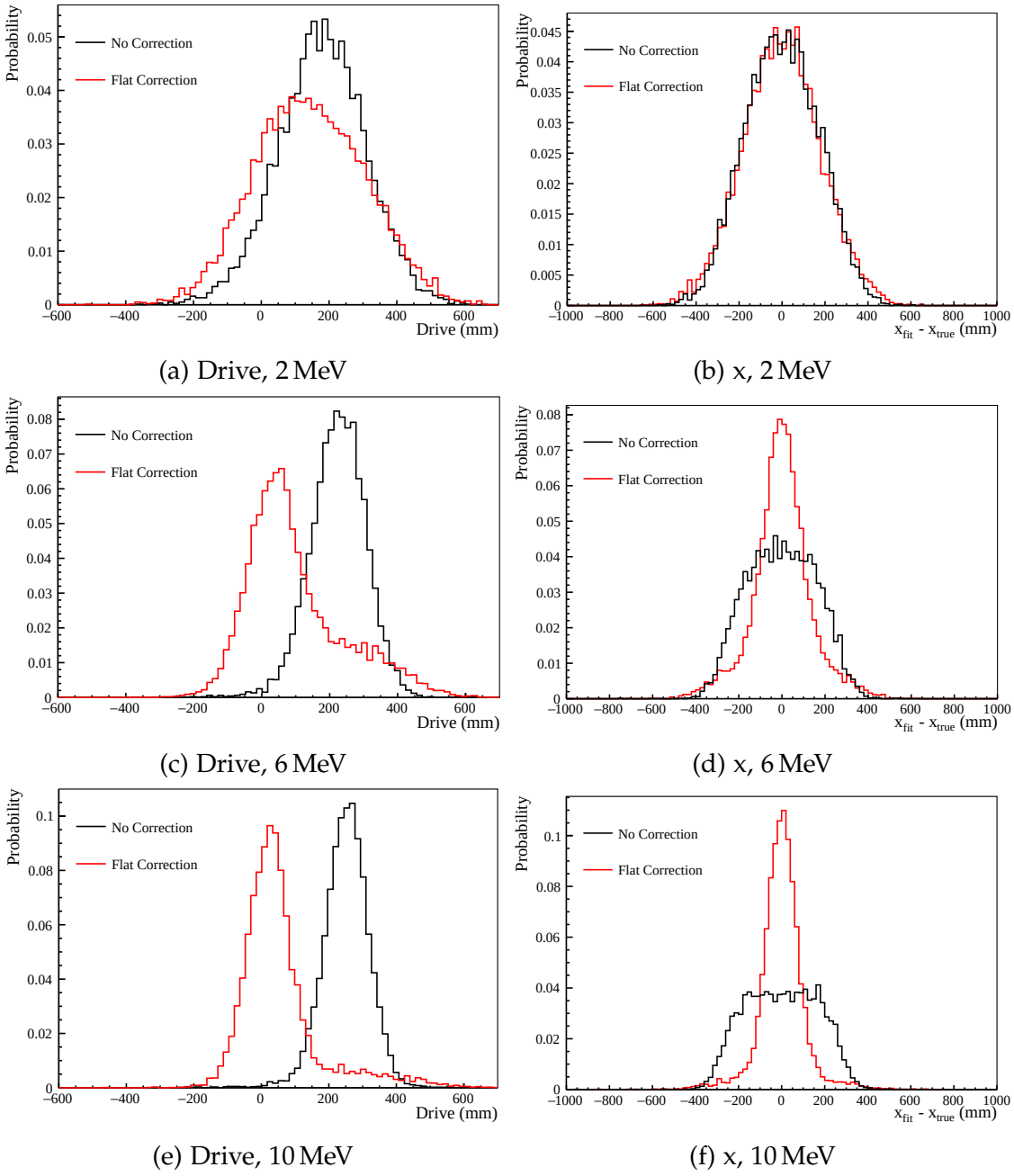
gorithm, the drive was found to be 179 ± 1 mm at 2 MeV, 225.9 ± 0.8 mm at 6 MeV and 252.3 ± 0.6 mm at 10 MeV. Approximate average drives of D_{ave} =180 mm, 200 mm and 250 mm were used respectively. For general use of this method, a translation between reconstructed energy and average drive would be required. Flat drive correction was tested using electrons with isotropic directions in the centre of a perfect-state detector. The results of this reconstruction method can be seen in Figure 5.8, including both the drive and the performance of reconstruction along the x-axis. A summary of the performance of position reconstruction before and after flat correction can be found in Table 5.5.

Absolute Mean Drive		
Energy (Mev)	Before Correction (mm)	After Correction (mm)
2	178	145
6	224.2	97.86
10	250.5	53.47

X Resolution		
Energy (MeV)	Before Correction (mm)	After Correction (mm)
2	167.3±1.0	179.1±1.2
6	150.9±0.8	113.2±1.4
10	152.3±0.8	73.4±0.7

Table 5.5: Results of flat drive correction on mean drive and x-axis resolution. The absolute mean is used to account for the non-Gaussian shoulder after drive correction. The x-axis resolution is found from a fit Gaussian.

It can be seen that, while at 2 MeV there is very little change, at the higher energies the position improves in both drive and resolution along the x-axis. The drive correction is more effective at the higher energy as the initial direction reconstruction is more likely to be correct. A small number of events increase in drive, creating a shoulder in the distribution that extends beyond the original



(a) Drive, 2 MeV

(b) x, 2 MeV

(c) Drive, 6 MeV

(d) x, 6 MeV

(e) Drive, 10 MeV

(f) x, 10 MeV

Figure 5.8: Results of the flat drive correction method on electrons with energies 2 MeV, 6 MeV and 10 MeV. At 2 MeV very little change is seen. However, at the higher energies, it can be seen the the peak in drive (left) significantly reduces, and the x-axis resolution (right) improves.

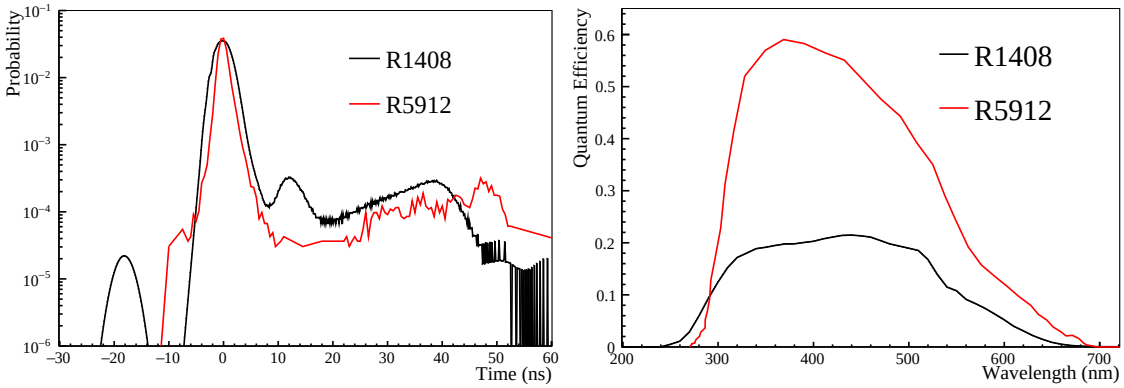
distribution. These are events that reconstructed poorly in direction initially, causing their drive "correction" to be in the wrong direction. For this reason, results are quoted as the absolute mean instead of the mean of a fit Gaussian of the peak.

Flat drive correction offers a method to improve the position reconstruction using directional data, but will only be effective if the direction is reconstructed accurately. Therefore, further methods of improving direction reconstruction are desirable.

5.2 Directionality using Improved Photodetection

The SNO detector originally began commissioning in 1990. While many upgrades were made to the detector for the transition to the SNO+ experiment, including the background suppression and the data acquisition, the original PMTs were left in place. However, four additional PMTs were installed of a more modern model: the Hamamatsu R5912 [137]. This was for the purpose of testing capabilities of future neutrino detectors that would use more modern photodetection technology.

The transit time distribution [95] and quantum efficiency [137] of the R5912 PMT are shown in Figure 5.9, alongside those of the R1408. Pre-pulsing has not been accounted for in the R5912. The time distribution is much narrower, and a Gaussian fit to the peak returns a standard deviation of 0.82 ns.



(a) (b)

Figure 5.9: Comparison of the transit time and quantum efficiency efficiency of the R5912 and R1408 PMTs. The timing distribution of the R5912 is much narrower, and the quantum efficiency is higher. Figures were made using the values used to simulate both PMT types in the SNO+ experiment.

In order to investigate the directionality capabilities of future neutrino detectors, the simulation of the SNO+ experiment was altered to use the transit times and quantum efficiency of the R5912 PMT. The remainder of the simulation was left the same, including PMT placements and concentrators, and the detector was simulated assuming perfect detector conditions.

The position reconstruction is expected to improve with the use of faster PMTs. The multiPDF reconstruction algorithm PDF was updated by simulating 10^5 electrons of energy 3 MeV and calculating a new t_{res} distribution for use as a PDF. The new position-time reconstruction performance can be seen in Figure 5.10.

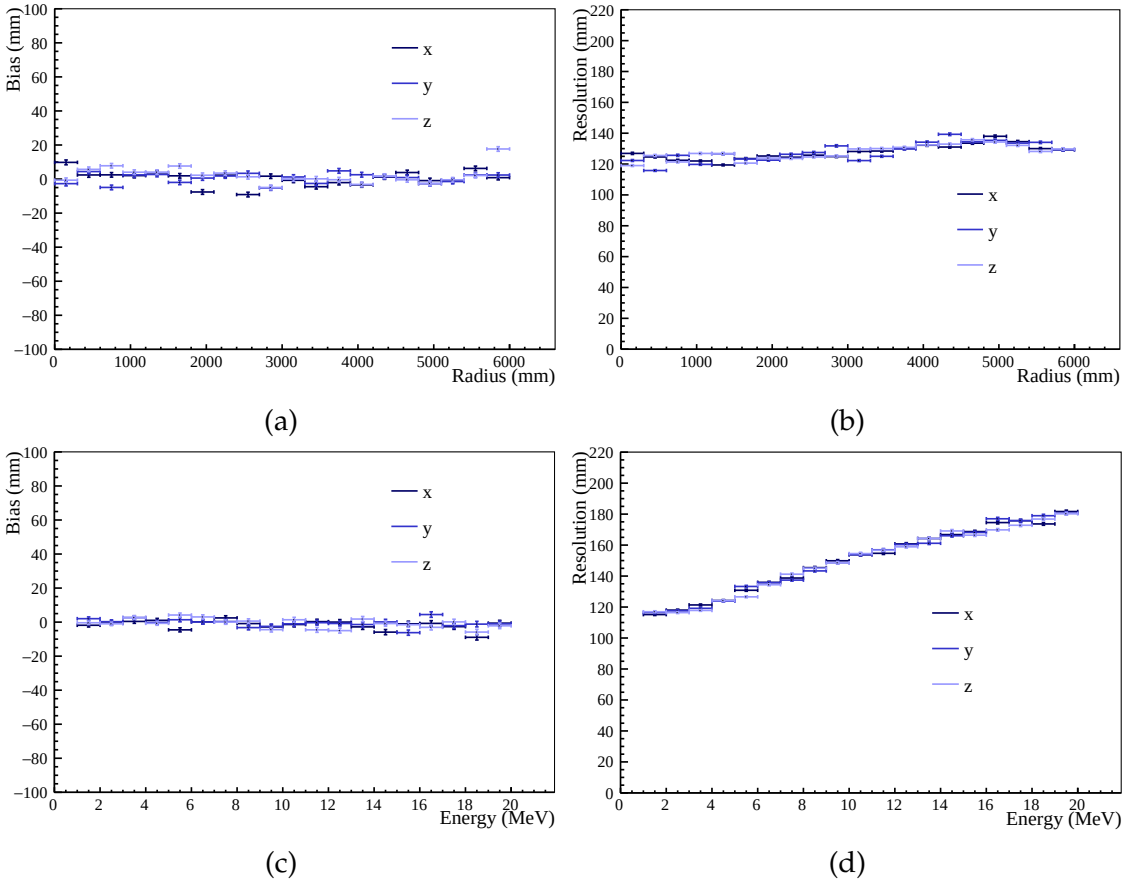


Figure 5.10: Performance of position reconstruction in using the R5912 PMT, using the MultiPDF method. Results are displayed for simulations of a 0.6 g/L PPO scintillator cocktail. Each point represents a Gaussian fit to $x_{i,recon} - x_{i,true}$ distributions, where x_i is the relevant position parameter.

The resolution of position reconstruction has slightly improved compared to that seen in Figure 3.7, reducing to ∼130 mm in each direction for 6 MeV electrons, leading to a total spatial resolution of ∼23 cm. This can be improved further by tuning the effective group velocity parameters in simulation, but this is beyond the scope of this thesis. The drive as a function of energy can be seen in Figure 5.11, and does not significantly change with the use of improved PMTs as compared to Figure 4.11.

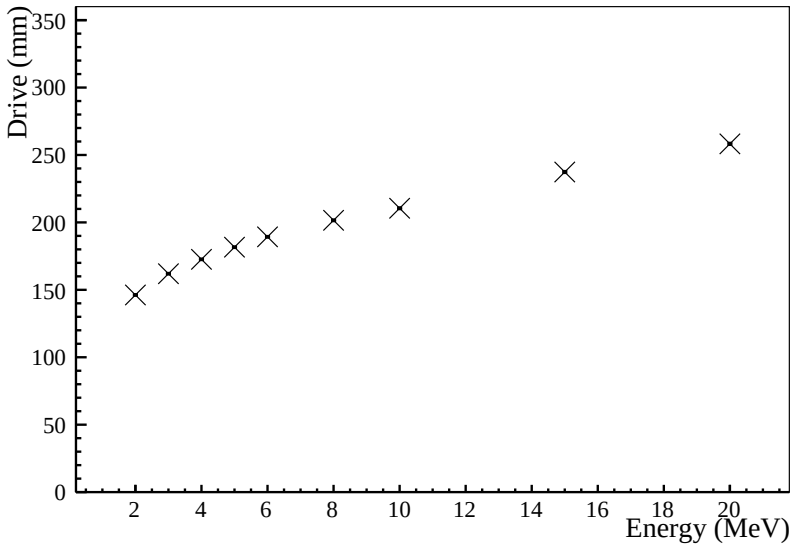
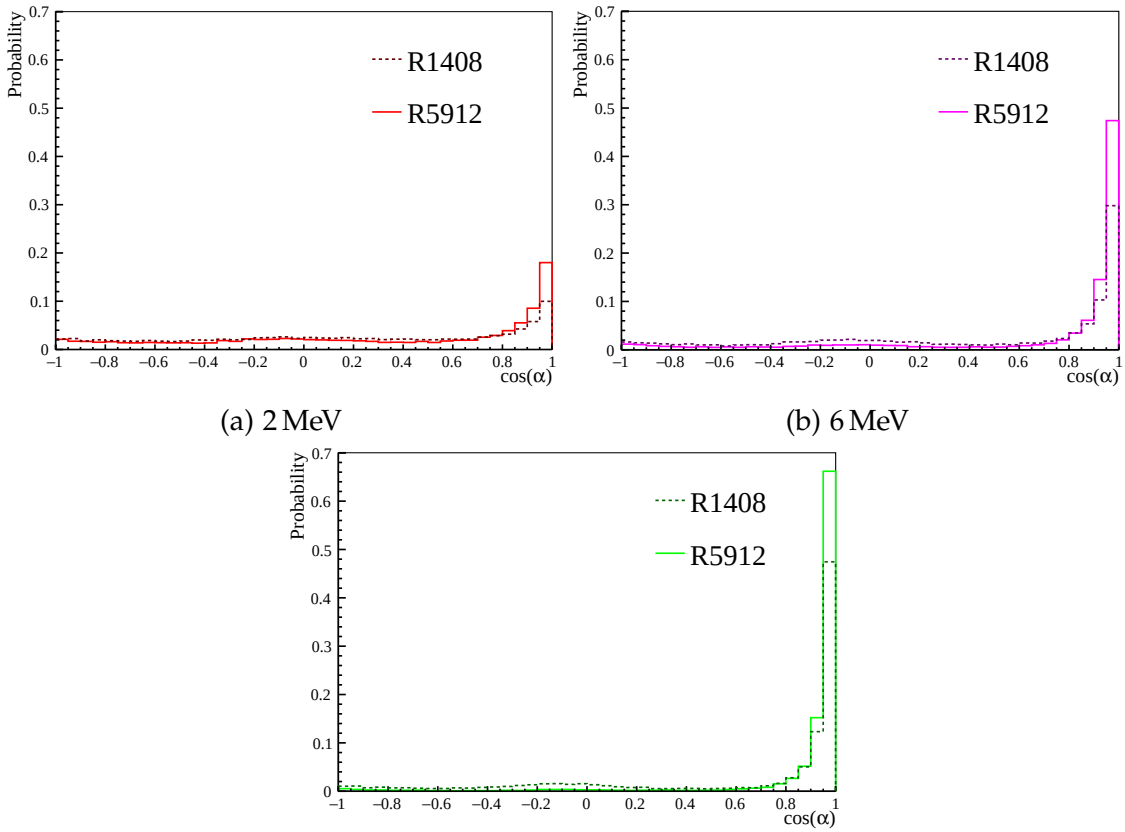


Figure 5.11: Drive as a function of energy using the R5912. Drive is not significantly changed by the use of improved PMTs.

The recoordinated position reconstruction was then used to create a new PDF for direction reconstruction, created in the same way as described in Chapter 4 using 6 MeV electrons. Direction reconstruction was then performed using the maximum likelihood grid search described in Chapter 4, using the same grid parameters. Reconstruction performance was tested in simulation using electrons of energies from 1 MeV to 10 MeV. Only events with a valid position-time vertex were considered, and a radius cut of r <5.5 m was applied. The results can be seen in Figures 5.12 and 5.13, with the percentage of events reconstructing with $\cos(\alpha) > 0.8$ shown in Table 5.6 and Figure 5.14. For comparisons to the R1408 PMT, simulations were run with equivalent detector and event conditions.



(a) 2 MeV

(b) 6 MeV

(c) 10 MeV

Figure 5.12: Results for direction reconstruction at different electron energies using the R5912 PMT. Direction reconstruction is stronger as compared to using the R1408 PMT.

It can be seen that the performance of direction reconstruction is significantly improved by using PMTs with faster timing and higher quantum efficiency. The energy range 1 MeV to 3 MeV covers the areas of interest for multiple important neutrino studies, including CNO solar neutrinos and anti-neutrinos from reactors. This study shows that future neutrino detectors undertaking these studies can achieve improved directional reconstruction from only the use of modern PMT capabilities.

Notably, $41.6 \pm 0.5\%$ of 2.5 MeV electrons reconstruct with $\cos(\alpha) > 0.8$. The Q-value of double beta decay for ^{130}Te is 2.5 MeV [138]. This means that the use of R5912 PMTs could allow a directional solar background reduction of $\sim$40% for a 10% loss of signal in a $0\nu\beta\beta$ study. For the case of event rejection for

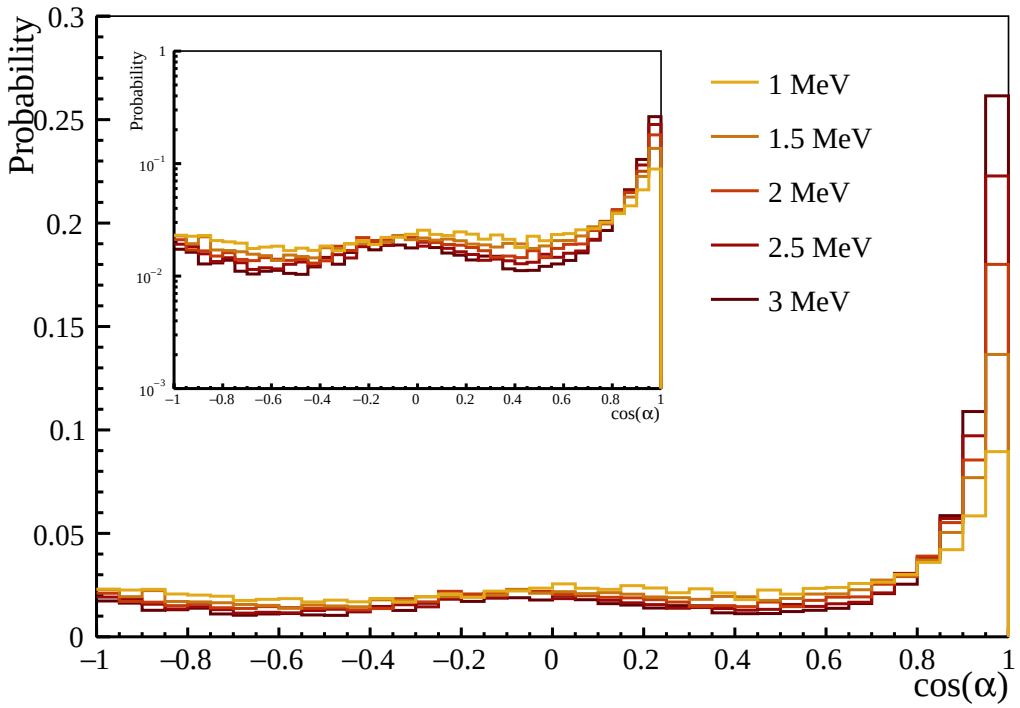


Figure 5.13: A more detailed look at direction reconstruction in the range 1 MeV to 3 MeV using R5912 PMTs.

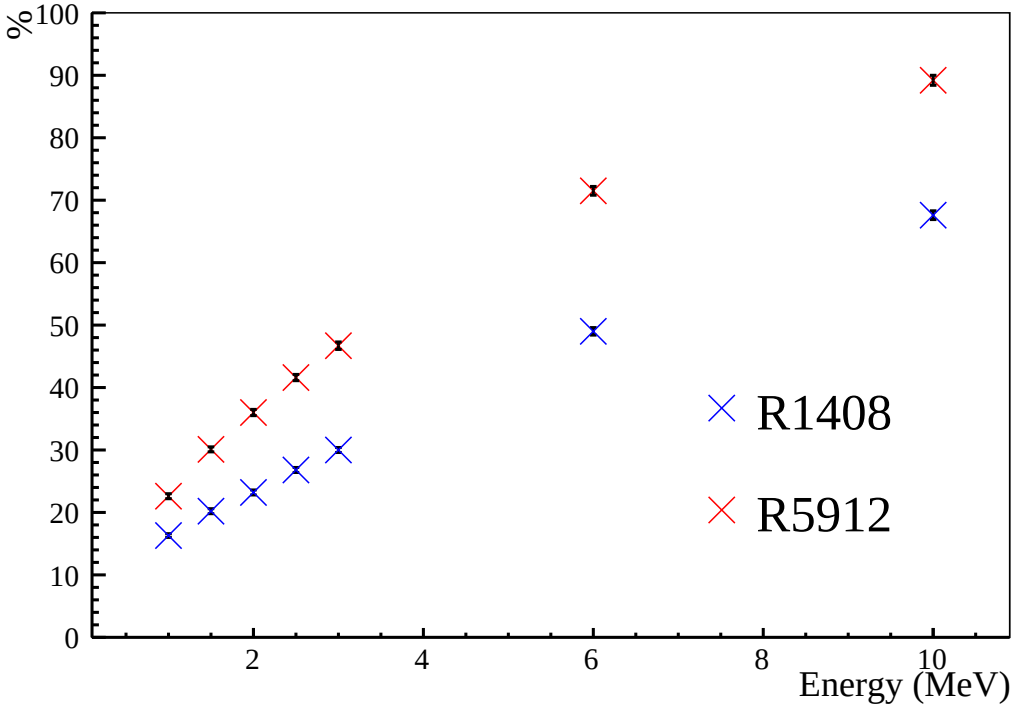


Figure 5.14: A comparison of the percentage of events with $\cos(\alpha) > 0.8$ for different electron energies, using both the R5912 and R1408 PMTs.

Energy (MeV)	% (R5912)	% (R1408)
1	22.6 ± 0.4	16.3 ± 0.3
1.5	30.1 ± 0.4	20.2 ± 0.4
2	36.0 ± 0.5	23.2 ± 0.4
2.5	41.6 ± 0.5	26.8 ± 0.4
3	46.7 ± 0.6	30.0 ± 0.4
6	71.5 ± 0.7	49.0 ± 0.6
10	89.2 ± 0.8	67.6 ± 0.7

Table 5.6: Comparison of direction reconstruction for simulated electrons at different energies based on the percentage of events that reconstruct with $\cos(\alpha) > 0.8$, using both the R1408 and R5912 PMTs.

$\cos(\alpha) > 0.9$, $\sim$30% of solar events can be rejected for a signal loss of 5%. In SNO+, ^{8}B solar neutrinos are expected to constitute 50% of the background for the $0\nu\beta\beta$ search [139], so directional discrimination could allow for a significant reduction of backgrounds.

5.3 Comparison to Slow Scintillators

Simulated studies of a large-scale detector filled with the slow fluor acenaphthene (characterised in Chapter 2 and [20]) were carried out by Dunger, Leming and Biller [101] for the purpose of examining the potential for direction reconstruction in a future slow-scintillator detector. The scintillator mixture simulated used 4 g/L acenaphthene in LAB. A simultaneous reconstruction of position-time-direction was conducted. This investigation used a larger detector than SNO+ — with an 8.8 m radius AV — and 21873 inward facing Hamamatsu R5912 PMTs for 77% effective photocathode coverage.

Several variations on this configuration were also studied. The effect of photon sampling was tested with a lowered effective coverage of 30%. Light

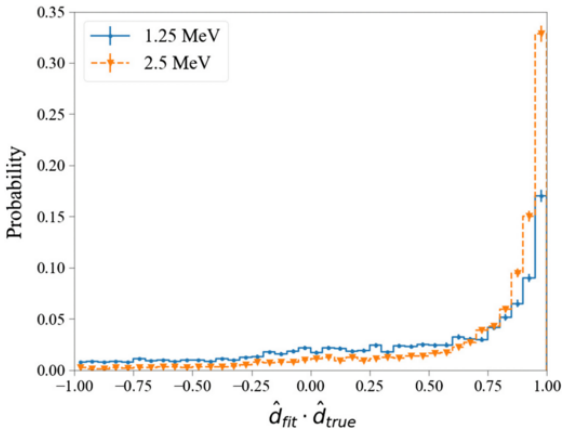
yield dependance was investigated by simulating both with and without the addition of the secondary fluor bis-MSB, which would reduce reabsorption and increase light yield. A further variation using slower PMTs was also tested, indicated as the "SLOW" configuration, although the quantum efficiency of the PMTs was not varied. A summary of the configurations used for comparison to studies in PPO can be found in Table 5.7.

Configuration	Coverage (%)	PMT FWHM (ns)	Bis-MSB Conc. (g/L)
77_FAST_1	77	1	1
30_FAST_1	30	1	1
77_SLOW_0	77	3.7	0
30_FAST_0	30	1	0
30_SLOW_0	30	3.7	0

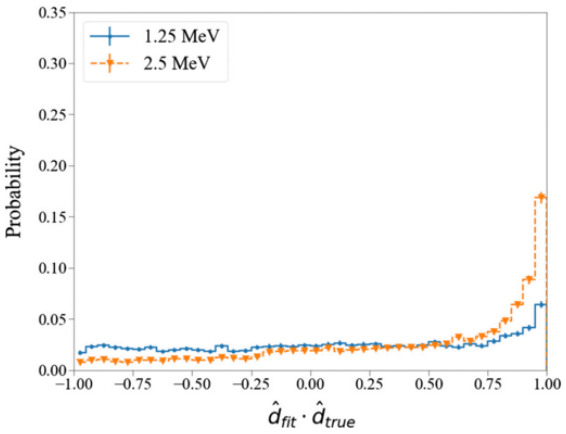
Table 5.7: Summary of the simulated configurations of slow scintillator studies, used in comparison to PPO directionality. Variations were used in the photocathode coverage, the full width half maximum (FWHM) of the transit time distribution of the PMTs, and the concentration of the secondary fluor bis-MSB. Values taken from [101].

An approximate comparison is possible with the investigation described in the previous section, using the effective photocathode coverage of SNO+ of $\sim$50%. The results of the slow scintillator configurations are compared to the results achievable in 0.6 g/L PPO in LAB in Figures 5.15 and 5.16.

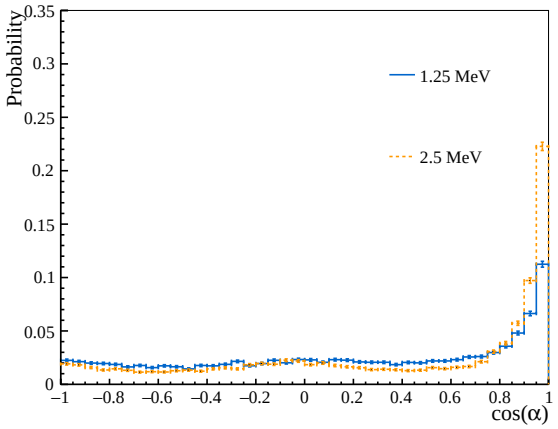
It can be seen that direction reconstruction is dependent on photocathode coverage due to the requirement for good photon sampling. The results of reconstruction using PPO are between those of the two acenaphthene examples that contain bis-MSB, consistent with the relative coverages. This implies that the faster timing of the scintillator does not have a significant impact on directionality in this detector configuration. However, PPO underperforms when compared to slow scintillator studies that contained no bis-MSB. This is because



(a) Acenaphthene
77_FAST_1



(b) Acenaphthene
30_FAST_1

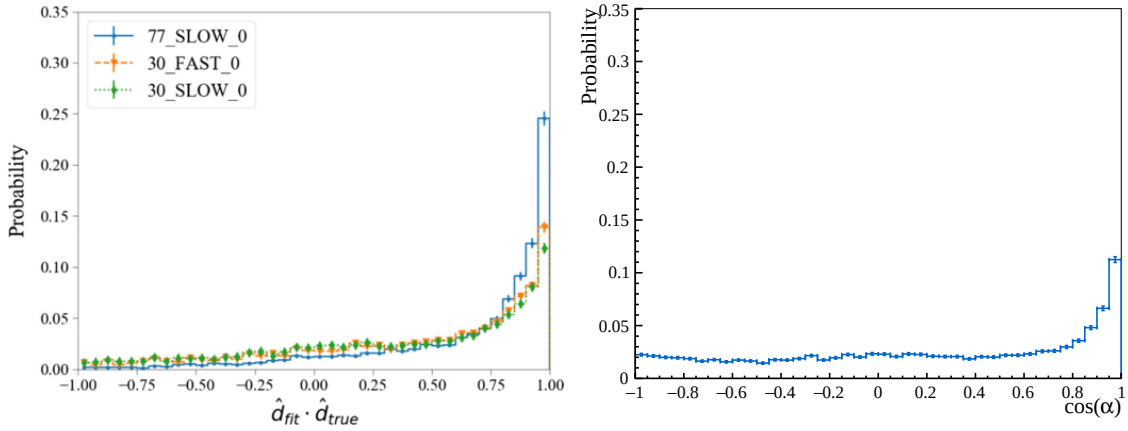


(c) 0.6 g/L PPO in LAB
∼50% Effective Coverage

Figure 5.15: Comparison of direction reconstruction in 0.6 g/L PPO in LAB to 4 g/L acenaphthene in LAB with the addition of the secondary fluor bis-MSB. All simulations used R5912 PMTs and electrons at 1.25 MeV and 2.5 MeV. It can be seen that the reconstruction capabilities are dependent on coverage, and the performance in PPO with 50% coverage lies between the two slow scintillator examples. Figures (a) and (b) taken from [101].

the light yield of the acenaphthene is lower, allowing for a more prominent Cherenkov peak and easier direction reconstruction.

In the slow scintillator study, it was found that there was not a large dependence on PMT timing. The ability to reconstruct direction relies on good separation of Cherenkov light, and in slow scintillator even the slower PMTs are able to distinguish between the early Cherenkov photons and the later scintillation



(a) Acenaphthene
No bis-MSB

(b) 0.6 g/L PPO in LAB
∼50% Effective Coverage

Figure 5.16: Comparison of direction reconstruction in 0.6 g/L PPO in LAB to 4 g/L acenaphthene in LAB without bis-MSB. All simulations used electrons at 1.25 MeV. Configurations are marked "SLOW" and "FAST" dependent on PMT types simulated, and the percentage coverage is given. It can be seen that reconstruction in PPO underperforms compared to acenaphthene. Figure (a) taken from [101].

ones. This was not the case for PPO, where a significant increase in directionality was seen when fast PMTs were used due to the faster timing of the scintillator.

The relative light yields of the scintillator mixtures should also be accounted for, as a higher light yield allows for more precise energy reconstruction, which is highly desirable for searches such as $0\nu\beta\beta$. The number of detected hits per MeV of electron energy for each configuration can be seen in Table 5.8.

The detected hits/MeV is approximately proportional to the photocathode coverage of the detector (without saturation effects). This means a comparison can be made by dividing the hits/MeV by the percentage coverage of the detector, as seen in the final column of Table 5.8. The addition of bis-MSB increases the light yield of acenaphthene — reducing the ability to reconstruct direction — but the absolute yield is still lower than that of PPO, even at the low concentration of 0.6 g/L. While direction reconstruction is a desirable method of background rejection, high light yield is vital to many low energy neutrino studies, meaning that PPO may be the better candidate.

Fluor	Coverage (%)	Hits/MeV	Hits/Coverage
Acenaphthene	77	500	6.5
Acenaphthene	30	200	6.5
Acenaphthene + bis-MSB	77	1000	13
Acenaphthene + bis-MSB	30	400	13
PPO	50	750	15

Table 5.8: Detected hits per MeV for slow scintillators compared to PPO, for simulations of PMTs with the same quantum efficiency. The detected light yield is dependent on the scintillator cocktail and the coverage of the detector. An approximate value for the hits per coverage is also provided, as a measure of relative absolute yield. Values for acenaphthene taken from [101].

Slow scintillators have great potential for directionality in large scale scintillator experiments. However, these studies show that if fast photon detection technology is prioritised, the use of common scintillator cocktails such as LABPPO should still allow for comparable direction reconstruction while prioritising high light yield.

5.4 Conclusions

Direction reconstruction on an event-by-event basis has been achieved in a large-scale high-yield liquid scintillator for the first time using the methods described in Chapter 4. However, there are improvements to direction reconstruction that could be achieved with continued work in the area. In this chapter, position reconstruction and photon sampling were investigated.

The improvement of position reconstruction through the reduction of direction-dependent drive could be an avenue to improving direction reconstruction, as shown in Section 4.2.1. Simultaneous direction-position reconstruction was implemented using an adaptive-grid optimiser to decrease the computing time required for a six-dimensional optimisation. However, when testing performance

using 6 MeV electrons, the simultaneous reconstruction underperformed compared to direction-only reconstruction. It was found that there was insufficient photon sampling to consistently distinguish between two equivalent points in the likelihood space. At higher energies this effect was reduced, leading to an improved average position reconstruction at 10 MeV, but direction reconstruction still underperformed compared to direction-only reconstruction. Simultaneous reconstruction of position and direction has been shown to be effective in a simulated study of a detector with higher photon sampling and a slower scintillator [101], so efforts to use this method in future neutrino detectors should yield more effective results.

A method of drive reduction using reconstructed direction was also attempted, known as "flat drive correction". This involved correcting the reconstructed position by a set length — dependent on energy — opposite to the reconstructed direction. When tested using electrons at energies 6 MeV and 10 MeV, this method successfully reduced the average drive and improved position resolution. However, at 2 MeV very little effect was seen, due to the inability to effectively reconstruct direction. Continued work on the improvement of position reconstruction using directional information is ongoing.

The use of modern PMTs would improve photon sampling in a large scale detector due to faster timing and higher quantum efficiencies. By simulating the SNO+ detector with Hamamatsu R5912 PMTs, future capabilities of similar neutrino detectors can be investigated. Direction reconstruction was found to significantly improve, with the percentage of events with $\cos(\alpha) > 0.8$ increasing from $49.0 \pm 0.6\%$ to $71.5 \pm 0.7\%$ for 6 MeV electrons. Low energy performances also improve, leading to potential improvements to studies into CNO solar neutrinos, reactor antineutrinos, and even $0\nu\beta\beta$ studies. By using a simple cut on directional reconstruction compared to the direction of the sun, the ^{8}B solar neutrino background could be reduced by 30-40% in a $0\nu\beta\beta$ search with a signal

loss of 5-10%. For a SNO+-like detector, this would lead to a 15-20% reduction in total background. By comparing these simulations of SNO+ with improved PMTs to simulations of the slow fluor acenaphthene, a comparable direction reconstruction performance was demonstrated with a higher absolute light yield.

There are numerous methods being explored for extracting directional information from liquid scintillator detectors, many of which were discussed in Section 1.3.3. The field of hybrid Cherenkov-scintillation detectors is continuing to progress with significant interest from the neutrino physics community. In this thesis it has been shown that directionality in a liquid scintillator detector is achievable without the inclusion of additional detector hardware or specialised detector cocktails. If direction reconstruction is desired down to energies useful for studies such as $0\nu\beta\beta$, significant improvement can be gained just from the use of modern photon detection technology. However, it is expected that the combination of multiple hybridisation technologies will allow for even more powerful directional rejection of background events, allowing for improved sensitivities in neutrino physics searches that may be able to answer some of the most prominent and fundamental questions in modern particle physics.

Chapter 6

Conclusions

"I may not have gone where I intended to go, but I think I have ended up where I needed to be."

- The Long Dark Tea-Time of The Soul, Douglas Adams

Direction reconstruction offers strong background rejection in large-scale neutrino experiments. While scintillator detectors benefit from high light-yield — leading to good energy resolution and no minimum energy threshold — the light emission is isotropic with no directional information. However, if Cherenkov light could be isolated from the dominant scintillation signal, it could be possible to combine the strengths of the two detection techniques. In this thesis, a method for reconstructing direction through time separation of Cherenkov light was presented, and its effective use was demonstrated using ^{8}B solar neutrinos in the SNO+ detector.

Slow fluors for use in future neutrino detectors were investigated. Four candidate fluors were selected, and their time profiles were characterised. In each of the measurements, a clear directional Cherenkov peak was seen separated from the late scintillation light. Time constants of the scintillator mixtures were found to be on the order of tens of nanoseconds, which would be easily separable for standard large PMTs used in neutrino experiments. While additional properties of the scintillators should also be considered, such as emission wavelength and light yield, each of these fluors could be potentially used in a hybrid Cherenkov-scintillation detector.

The method presented for direction reconstruction in liquid scintillator involved a maximum likelihood search. A 2D PDF was used, containing a distribution in time and angle of individual detected photons in an event. In a simulation of the SNO+ detector, it was shown that the direction of 6 MeV electrons could be reconstructed within $\cos(\alpha) > 0.8$ 45.6% of the time. This method was tested using ^{8}B solar neutrinos with energies >5 MeV in the SNO+ detector while it contained a low concentration scintillator. A clear peak in the solar direction was seen. The resulting distribution was found to have a significance of $> 5.7\sigma$, making it the first demonstration of event-by-event direction reconstruction in a large-scale high-yield liquid scintillator detector.

Finally, future prospects for directionality in scintillator detectors were explored. Two major limiting factors on the ability to reconstruct direction were investigated: biases in position reconstruction and insufficient photon sampling. As position reconstruction is known to have a directional bias, a method for reconstructing position and direction simultaneously was presented. However, this method was only found to be effective in simulations of the SNO+ detector at high energies, requiring further improvements to be used in physics analyses. Improved photon detection was investigated by simulating PMTs with higher quantum efficiencies and faster timing. These simulations demonstrated significantly better directionality. When compared with equivalent studies of slow scintillators, it was shown that the performance of the relatively fast PPO had a comparable effectiveness, while maintaining a higher detected photon yield. This shows incredible potential for future neutrino detectors, as direction reconstruction can be made possible with only minimal changes to detector infrastructure and with no loss to energy resolution.

Appendix A

Glossary

$0\nu\beta\beta$ Neutrinoless double beta decay

$2\nu\beta\beta$ Two neutrino double beta decay

AV Acrylic vessel

bisMSB 1,4-Bis(2-methylstyryl)benzene

BiPo β decay of Bismuth followed by the α decay of the daughter Polonium

BSM Beyond the Standard Model

CID Correlated and Integrated Directionality

CNO Carbon-Nitrogen-Oxygen

DAQ Data Acquisition

DDA N,N-Dimethyldodecylamine

ES Elastic Scattering

FEC Front End Card

FWHM Full width half maximum

GT Global Trigger

IBD Inverse Beta Decay

IRF Impulse Response Function

LAB Linear alkylbenzene. Main component (solvent) of the SNO+ scintillator

LABPPO Linear alkylbenzene solvent with 2,5-Diphenyloxazole primary fluor

LAPPD Large Area Picosecond Photodetector

LArTPC Liquid Argon Time Projection Chamber

LLH Log-likelihood

LS Liquid scintillator

MC Monte Carlo simulation

MSC Multiple Scattering

MSW effect Mikheyev–Smirnov–Wolfenstein effect

MTC Master Trigger Card

NHits Number of triggered (hit) PMTs in an event

$\nu - e$ Neutrino-electron

$\nu - e$ **ES** Neutrino-electron elastic scattering

OWL Outward Looking (PMTs)

PDF Probability distribution function

PMNS matrix Pontecorvo-Maki-Nakagawa-Sakata matrix

PMT Photomultiplier tube

PP Proton-Proton chain

PPO 2,5-Diphenyloxazole. Primary fluor of the SNO+ scintillator

PSUP PMT support structure

RAT Reactor Analysis Tool. Software used on the SNO+ experiment.

SM Standard Model of Particle Physics

SNU Solar Neutrino Units ($1\,\text{SNU} = 10^{-36}\,\text{events/atom/sec}$)

TPC Time projection chamber

t_{res} Time Residual. An estimation of emission time. Defined in equation 3.4.1.

TTS Transit time spread

UPW Ultra pure water

WbLS Water-based liquid scintillator

References

[1] W. Pauli, *Dear radioactive ladies and gentlemen*, Phys. Today **31N9** (1978) 27.

[2] F. Reines, *The neutrino: from poltergeist to particle*, Rev. Mod. Phys. **68** (1996) no. 2, 317–327.

[3] C. L. Cowan Jr., F. Reines, F. B. Harrison, H. W. Kruse, and A. D. McGuire, *Detection of the Free Neutrino: a Confirmation*, Science **124** (1956) no. 3212, .

[4] C. L. Cowan Jr. and F. Reines, *The Neutrino*, Nature **178** (1956) 446–449.

[5] G. Danby, J.-M. Gaillard, K. Goulianos, L. M. Lederman, N. Mistry, M. Schwartz, and J. Steinberger, *Observation of High-Energy Neutrino Reactions and the Existence of Two Kinds of Neutrinos*, Phys. Rev. Lett. **9** (1962) 36–44.

[6] R. Davis, D. S. Harmer, and K. C. Hoffman, *Search for Neutrinos from the Sun*, Phys. Rev. Lett. **20** (1968) no. 21, 1205–1209.

[7] B. T. Cleveland, T. Daily, J. Raymond Davis, J. R. Distel, K. Lande, C. K. Lee, P. S. Wildenhain, and J. Ullman, *Measurement of the Solar Electron Neutrino Flux with the Homestake Chlorine Detector*, The Astrophysical Journal **496** (1998) no. 1, 505–526.

[8] J. N. Bahcall and R. Davis, *Solar Neutrinos: A Scientific Puzzle*, Science **191** (1976) no. 4224, 264–267.

[9] SNO Collaboration, Q. R. Ahmad et al., *Direct Evidence for Neutrino Flavor Transformation from Neutral-Current Interactions in the Sudbury Neutrino Observatory*, Phys. Rev. Lett. **89** (2002) no. 1, 011301.

[10] SNO Collaboration, B. Aharmim et al., *Combined analysis of all three phases of solar neutrino data from the Sudbury Neutrino Observatory*, Phys. Rev. C **88** (2013) no. 2, 025501.

[11] Super-Kamiokande Collaboration, Y. Ashie et al., *Evidence for an Oscillatory Signature in Atmospheric Neutrino Oscillations*, Phys. Rev. Lett. **93** (2004) no. 10, 101801.

[12] J. R. Klein et al., *Future Advances in Photon-Based Neutrino Detectors: A SNOWMASS White Paper*, `arXiv:2203.07479 [physics.ins-det]`.

[13] C. Aberle, A. Elagin, H. J. Frisch, M. Wetstein, and L. Winslow, *Measuring directionality in double-beta decay and neutrino interactions with kiloton-scale scintillation detectors*, JINST **9** (2014) no. 06, P06012.

[14] B. J. Land, Z. Bagdasarian, J. Caravaca, M. Smiley, M. Yeh, and G. D. Orebi Gann, *MeV-scale performance of water-based and pure liquid scintillator detectors*, Phys. Rev. D **103** (2021) no. 5, 052004.

[15] Mohan Li and Ziyi Guo and Minfang Yeh and Zhe Wang and Shaomin Chen, *Separation of scintillation and Cherenkov lights in linear alkyl benzene*, Nucl. Instrum. Meth. A **830** (2016) 303–308.

[16] J. Caravaca, F. B. Descamps, B. J. Land, M. Yeh, and G. D. Orebi Gann, *Cherenkov and scintillation light separation in organic liquid scintillators*, Eur. Phys. J. C **77** (2017) no. 12, 811.

[17] Z. Guo, M. Yeh, R. Zhang, D.-W. Cao, M. Qi, Z. Wang, and S. Chen, *Slow liquid scintillator candidates for MeV-scale neutrino experiments*, Astroparticle Physics **109** (2019) 33–40.

[18] J. Caravaca, B. J. Land, M. Yeh, and G. D. Orebi Gann, *Characterization of water-based liquid scintillator for Cherenkov and scintillation separation*, Eur. Phys. J. C **80** (2020) no. 9, 867.

[19] J. Gruszko, B. Naranjo, B. Daniel, A. Elagin, D. Gooding, C. Grant, J. Ouellet, and L. Winslow, *Detecting Cherenkov light from 1–2 MeV electrons in linear alkylbenzene*, JINST **14** (2019) no. 02, P02005.

[20] S. D. Biller, E. J. Leming, and J. L. Paton, *Slow fluors for effective separation of Cherenkov light in liquid scintillators*, Nucl. Instrum. Meth. A **972** (2020) no. 164106, .

[21] T. Kaptanoglu, M. Luo, B. Land, A. Bacon, and J. R. Klein, *Spectral photon sorting for large-scale Cherenkov and scintillation detectors*, Phys. Rev. D **101** (2020) no. 7, 072002.

[22] Borexino Collaboration, M. Agostini et al., *Correlated and Integrated Directionality for sub-MeV solar neutrinos in Borexino*, Phys. Rev. D **105** (2021) 052002.

[23] LSND Collaboration, C. Athanassopoulos et al., *The liquid scintillator neutrino detector and LAMPF neutrino source*, Nucl. Instrum. Meth. A **388** (1997) no. 1, 149–172.

[24] R.B. Patterson and E.M. Laird and Y. Liu and P.D. Meyers and I. Stancu and H.A. Tanaka, *The extended-track event reconstruction for MiniBooNE*, Nucl. Instrum. Meth. A **608** (2009) no. 1, 206–224.

[25] T. Anderson et al., *Eos: conceptual design for a demonstrator of hybrid optical detector technology*, JINST **18** (2023) no. 02, P02009.

[26] Theia Collaboration, M. Askins, Z. Bagdasarian, N. Barros, E. Beier, E. Blucher, R. Bonventre, E. Bourret, E. Callaghan, J. Caravaca, M. Diwan, S. Dye, J. Eisch, A. Elagin, T. Enqvist, V. Fischer, K. Frankiewicz, C. Grant, D. Guffanti, C. Hagner, and K. Zuber, *Theia: an advanced optical neutrino detector*, The European Physical Journal C **80** (2020) .

[27] B. Pontecorvo, *Mesonium and Anti-Mesonium*, Sov. Phys. JETP **6** (1957) 429.

[28] B. Pontecorvo, *Inverse beta processes and nonconservation of lepton charge*, Zh. Eksp. Teor. Fiz. **34** (1957) 247.

[29] S. Bilenky, *Bruno Pontecorvo and Neutrino Oscillations*, Advances in High Energy Physics **2013** (2013) 9.

[30] R. Devenish, T. Weidberg, G. Barr, and R. Walczak, *Particle Physics in the LHC Era*. Oxford University Press, Oxford, UK, 2016.

[31] S. Adrián-Martínez et al., *Letter of intent for KM3NeT 2.0*, Journal of Physics G: Nuclear and Particle Physics **43** (2016) no. 8, 084001.

[32] KATRIN Collaboration, M. Aker et al., *The design, construction, and commissioning of the KATRIN experiment*, JINST **16** (2021) no. 08, T08015.

[33] K. Zuber, *Neutrino Physics*. Series in high energy physics, cosmology, and gravitation. Taylor & Francis, Boca Raton, FL, third ed., 2020.

[34] E. Majorana, *Teoria simmetrica dell'elettrone e del positrone*, Nuovo Cim. **14** (1937) 171–184. Translated from Italian by Luciano Maiani.

[35] F. F. Deppisch, *A Modern Introduction to Neutrino Physics*. Morgan & Claypool Publishers, San Rafael, CA, 2019.

[36] C. Giunti and C. W. Kim, *Fundamentals of Neutrino Physics and Astrophysics*. Oxford University Press, Oxford, UK, 2007.

[37] M. Goeppert-Mayer, *Double Beta-Disintegration*, Phys. Rev. **48** (1935) no. 6, 512–516.

[38] J. S. Lilley, *Nuclear Physics: Principles and Applications*. Wiley, Chichester, UK, 2001.

[39] Particle Data Group Collaboration, R. L. Workman et al., *Review of Particle Physics*, Prog. Theor. Exp. Phys. **2022** (2022) 083C01.

[40] W. H. Furry, *On Transition Probabilities in Double Beta-Disintegration*, Phys. Rev. **56** (1939) no. 12, 1184–1193.

[41] C. Adams et al., *Neutrinoless Double Beta Decay*, Arxiv:2212.11099, 2022. Prepared for the Fundamental Symmetries, Neutrons, and Neutrinos Town Meeting.

[42] S. Dell'Oro, S. Marcocci, M. Viel, and F. Vissani, *Neutrinoless Double Beta Decay: 2015 Review*, Advances in High Energy Physics **2016** (2016) 1–37.

[43] J. N. Bahcall, M. Kamionkowski, and A. Sirlin, *Solar neutrinos: Radiative corrections in neutrino-electron scattering experiments*, Phys. Rev. D **51** (1995) no. 11, 6146–6158.

[44] O. Tomalak and R. J. Hill, *Theory of elastic neutrino-electron scattering*, Phys. Rev. D **101** (2020) no. 3, 033006.

[45] S. Turck-Chièze and I. Lopes, *Toward a Unified Classical Model of the Sun: On the Sensitivity of Neutrinos and Helioseismology to the Microscopic Physics*, Astrophysical Journal **408** (1993) 347.

[46] J. N. Bahcall, M. H. Pinsonneault, and G. J. Wasserburg, *Solar models with helium and heavy-element diffusion*, Rev. Mod. Phys. **67** (1995) no. 4, 781–808.

[47] GALLEX Collaboration, W. Hampel et al., *GALLEX solar neutrino observations: Results for GALLEX IV*, Phys. Lett. B **447** (1999) 127–133.

[48] SAGE Collaboration, J. N. Abdurashitov et al., *Solar neutrino flux measurements by the Soviet-American Gallium Experiment (SAGE) for half the 22 year solar cycle*, J. Exp. Theor. Phys. **95** (2002) 181–193.

[49] K. S. Hirata et al., *Observation of* ^{8}B *solar neutrinos in the Kamiokande-II detector*, Phys. Rev. Lett. **63** (1989) 16–19.

[50] K. Hirata et al., *Experimental study of the atmospheric neutrino flux*, Physics Letters B **205** (1988) no. 2, 416–420.

[51] Borexino Collaboration, M. Agostini et al., *Comprehensive measurement of pp-chain solar neutrinos*, Nature **562** (2018) 505–510.

[52] J. N. Bahcall, *Neutrino Astrophysics*. Cambirdge University Press, Cambridge, 1989.

[53] C. Iliadis, *Nuclear physics of stars*. Wiley-VCH, Weinheim, second, revised and enlarged edition. ed., 2015.

[54] Borexino Collaboration, M. Pallavicini et al., *First real–time detection of solar pp neutrinos by Borexino*, EPJ Web of Conferences **121** (2016) 01001.

[55] Borexino Collaboration, G. Bellini et al., *First Evidence of pep Solar Neutrinos by Direct Detection in Borexino*, Phys. Rev. Lett. **108** (2012) 051302.

[56] Borexino Collaboration, C. Arpesella et al., *First real time detection of* ^{7}*Be solar neutrinos by Borexino*, Physics Letters B **658** (2008) no. 4, 101–108.

[57] Borexino Collaboration, M. Agostini et al., *Experimental evidence of neutrinos produced in the CNO fusion cycle in the Sun*, Nature **587** (2020) 577–582.

[58] J. Bahcall, *Software and data for solar neutrino research*, Http://www.sns.ias.edu/ jnb/, 2005.

[59] N. Vinyoles et al., *A New Generation of Standard Solar Models*, The Astrophysical Journal **835** (2017) no. 2, 202.

[60] ANTARES Collaboration, M. Ageron et al., *ANTARES: the first undersea neutrino telescope*, Nucl. Instrum. Meth. A **656** (2011) 11–38.

[61] KM3NeT Collaboration, A. Margiotta, *The KM3NeT deep-sea neutrino telescope*, Nucl. Instrum. Meth. A **766** (2014) 83–87. RICH2013 Proceedings of the Eighth International Workshop on Ring Imaging Cherenkov Detectors Shonan, Kanagawa, Japan, December 2-6, 2013.

[62] IceCube Collaboration, M. Aartsen et al., *The IceCube Neutrino Observatory: instrumentation and online systems*, JINST **12** (2017) no. 03, P03012.

[63] H. Kolanoski and N. Wermes, *Particle Detectors: Fundamentals and Applications*. Oxford University Press, 2020.

[64] P. A. Cherenkov, *Visible luminescence of pure liquids under the influence of γ-radiation [In Russian]*, Dokl. Akad. Nauk SSSR **2** (1934) no. 8, 451–454.

[65] P. A. Cherenkov, *Visible Radiation Produced by Electrons Moving in a Medium with Velocities Exceeding that of Light*, Phys. Rev. **52** (1937) no. 4, 378–379.

[66] I. M. Frank and I. E. Tamm, *Coherent visible radiation of fast electrons passing through matter [In Russian]*, Compt. Rend. Acad. Sci. URSS **14** (1937) no. 3, 109–114.

[67] I. Frank and I. Tamm, *Coherent Visible Radiation of Fast Electrons Passing Through Matter*, in *Selected Papers*, B. M. Bolotovskii, V. Y. Frenkel, and R. Peierls, eds., pp. 29–35. Springer Berlin Heidelberg, Berlin, Heidelberg, 1991. Translation of [66].

[68] J. D. Jackson, *Classical Electrodynamics*. Wiley, New York ; Chichester, third ed., 1999.

[69] A. Nath and N. K. Francis, *Detection techniques and investigation of different neutrino experiments*, International Journal of Modern Physics A **36** (2021) no. 13, 2130008.

[70] Borexino Collaboration, G. Alimonti et al., *The Borexino detector at the Laboratori Nazionali del Gran Sasso*, Nucl. Instrum. Meth. A **600** (2009) no. 3, 568–593.

[71] KamLAND Collaboration, A. Gando et al., *Reactor on-off antineutrino measurement with KamLAND*, Phys. Rev. D **88** (2013) no. 3, 033001.

[72] Daya Bay Collaboration, F. An et al., *The detector system of the Daya Bay reactor neutrino experiment*, Nucl. Instrum. Meth. A **811** (2016) 133–161.

[73] KamLAND-Zen Collaboration, S. Abe et al., *Search for the Majorana Nature of Neutrinos in the Inverted Mass Ordering Region with KamLAND-Zen*, Phys. Rev. Lett. **130** (2023) no. 5, 051801.

[74] J. B. Birks, *The theory and practice of scintillation counting*. International series of monographs on electronics and instrumentation ; v. 2. Pergamon Press, Oxford, UK, 1967.

[75] R. P. Wayne, *Principles and Applications of Photochemistry*. Oxford University Press, Oxford, UK, 1988.

[76] *Fluorescence and Phosphorescence*, Https://chem.libretexts.org/@go/page/1765, 2023. [Online; accessed 2023-06-16].

[77] T. Itoh, *Fluorescence and Phosphorescence from Higher Excited States of Organic Molecules*, Chemical Reviews **112** (2012) no. 8, 4541–4568.

[78] M. Koshimizu, *Recent progress of organic scintillators*, Japanese Journal of Applied Physics **62** (2022) no. 1, 010503.

[79] T. Kroupová, *Improving the Sensitivity to Neutrinoless Double Beta Decay in SNO+*. PhD thesis, University of Oxford, 2020.

[80] J. B. Birks, *Organic Molecular Photophysics*. Wiley, London, UK, 1973.

[81] J. B. Birks, *Scintillations from Organic Crystals: Specific Fluorescence and Relative Response to Different Radiations*, Proc. Phys. Soc. A **64** (1951) no. 10, 874.

[82] SNO+ Collaboration, M. Anderson et al., *Development, characterisation, and deployment of the SNO+ liquid scintillator*, JINST **16** (2021) no. 05, P05009.

[83] Borexino Collaboration, M. Agostini et al., *First Directional Measurement of Sub-MeV Solar Neutrinos with Borexino*, Phys. Rev. Lett. **128** (2022) 091803.

[84] F. Kulcsar, D. Teherani, and H. Altmann, *Study of the Spectrum of Cherenkov Light*, J. Radioanal. Chem. **68** (1982) 161–168.

[85] T. Kaptanoglu, *The Dichroicon: Spectral Photon Sorting For Large-Scale Cherenkov and Scintillation Detectors*, Presented at the international workshop on next generation nucleon decay and neutrino detectors (nnn19), 2019.

[86] P. G. B. Roland Winston, Juan C. Minano, *Nonimaging Optics*. Elsevier, San Diego, CA, 2005. With contributions by Narkis Shatz and John C. Bortz.

[87] MiniBooNE Collaboration, A. A. Aguilar-Arevalo et al., *The MiniBooNE Detector*, Nucl. Instrum. Meth. A **599** (2009) 28–46.

[88] M. Yeh, S. Hans, W. Beriguete, R. Rosero, L. Hu, R. Hahn, M. Diwan, D. Jaffe, S. Kettell, and L. Littenberg, *A new water-based liquid scintillator and potential applications*, Nucl. Instrum. Meth. A **660** (2011) no. 1, 51–56.

[89] L. Bignell, D. Beznosko, M. Diwan, S. Hans, D. Jaffe, S. Kettell, R. Rosero, H. Themann, B. Viren, E. Worcester, M. Yeh, and C. Zhang, *Characterization and modeling of a Water-based Liquid Scintillator*, JINST **10** (2015) no. 12, P12009.

[90] D. R. Onken, F. Moretti, J. Caravaca, M. Yeh, G. D. Orebi Gann, and E. D. Bourret, *Time response of water-based liquid scintillator from X-ray excitation*, Mater. Adv. **1** (2020) no. 1, 71–76.

[91] T. Kaptanoglu, E. J. Callaghan, M. Yeh, and G. D. O. Gann, *Cherenkov and scintillation separation in water-based liquid scintillator using an LAPPD^{TM}*, The European Physical Journal C **82** (2022) no. 2, .

[92] L. Kneale, *BUTTON: a technology testbed for future (anti)neutrino detection*, Presented at the 2023 iop joint app and hepp annual conference, 2023.

[93] J. Sawatzki, M. Wurm, and D. Kresse, *Detecting the diffuse supernova neutrino background in the future water-based liquid scintillator detector Theia*, Phys. Rev. D **103** (2021) no. 2, 023021.

[94] KamLAND Collaboration, F. Suekane, T. Iwamoto, H. Ogawa, O. Tajima, and H. Watanabe, *An overview of the kamland 1-kiloton liquid scintillator*, in *KEK - RCNP International School and Miniworkshop for Scintillating Crystals and their Applications in Particle and Nuclear Physics*, pp. 279–290. 2004.

[95] T. Kaptanoglu, *Characterization of the Hamamatsu 8" R5912-MOD Photomultiplier tube*, Nucl. Instrum. Meth. A **889** (2018) 69–77.

[96] J. Caravaca, F. B. Descamps, B. J. Land, J. Wallig, M. Yeh, and G. D. Orebi Gann, *Experiment to demonstrate separation of Cherenkov and scintillation signals*, Phys. Rev. C **95** (2017) no. 5, 055801.

[97] *Photomultiplier Tubes and Photomultiplier Tube Assemblies: R11265U Series / H11934 Series*, Https://www.hamamatsu.com/content/dam/hamamatsu-photonics/sites/documents/99_sales_library/etd/r11265u_h11934_tpmh1336e.pdf.

[98] *LAPPD^{TM}: Large Area Picosecond Photodetector*, Https://incomusa.com/wp-content/uploads/lappd-product-sheet-08-19.pdf.

[99] J. Ladislas Wiza, *Microchannel plate detectors*, Nuclear Instruments and Methods **162** (1979) no. 1, 587–691.

[100] A. Lyashenko et al., *Performance of Large Area Picosecond Photo-Detectors (LAPPD^{TM})*, Nucl. Instrum. Meth. A **958** (2020) 162834. Proceedings of the Vienna Conference on Instrumentation 2019.

[101] J. Dunger, E. J. Leming, and S. D. Biller, *Slow-fluor scintillator for low energy solar neutrinos and neutrinoless double beta decay*, Phys. Rev. D **105** (2022) no. 9, 092006.

[102] W. Luo, Q. Liu, Y. Zheng, Z. Wang, and S. Chen, *Reconstruction algorithm for a novel Cherenkov scintillation detector*, JINST **18** (2023) no. 02, P02004.

[103] L. M. Bollinger and G. E. Thomas, *Measurement of the Time Dependence of Scintillation Intensity by a Delayed-Coincidence Method*, Review of Scientific Instruments **32** (1961) no. 9, 1044–1050.

[104] S. Basu and E. Mccutchan, *Nuclear Data Sheets for A = 90*, Nuclear Data Sheets **165** (2020) 1–329.

[105] M. Berger, J. Coursey, M. Zucker, and J. Chang, *ESTAR, PSTAR, and ASTAR: Computer Programs for Calculating Stopping-Power and Range Tables for Electrons, Protons, and Helium Ions [Version 2.0.1]*, URL: http://physics.nist.gov/Star [May 8 2023], 2017.

[106] Förster, Th., *Excimers*, Angewandte Chemie International Edition in English **8** (1969) no. 5, 333–343.

[107] I. B. Berlman, *Handbook of fluorescence spectra of aromatic molecules*. Academic Press, New York ; London, 1965.

[108] J. B. Birks, D. J. Dyson, I. H. Munro, and B. H. Flowers, *'Excimer' fluorescence II. Lifetime studies of pyrene solutions*, Proceedings of the Royal Society of London. Series A. Mathematical and Physical Sciences **275** (1963) no. 1363, 575–588.

[109] SNO+ Collaboration, V. Albanese et al., *The SNO+ experiment*, JINST **16** (2021) no. 08, P08059.

[110] SNO+ Collaboration, S. Andringa et al., *Current Status and Future Prospects of the SNO+ Experiment*, Advances in High Energy Physics **2016** (2016) 6194250.

[111] F. Duncan, A. Noble, and D. Sinclair, *The Construction and Anticipated Science of SNOLAB*, Annual Review of Nuclear and Particle Science **60** (2010) no. 1, 163–180.

[112] M. Moorhead, *Reflectors in Cherenkov Detectors*. PhD thesis, University of Oxford, 1992.

[113] J. Boger et al., *The Sudbury Neutrino Observatory*, Nucl. Instrum. Meth. A **449** (2000) no. 1, 172–207.

[114] S. Biller, N. Jelley, M. Thorman, N. Fox, and T. Ward, *Measurements of photomultiplier single photon counting efficiency for the Sudbury Neutrino Observatory*, Nucl. Instrum. Meth. A **432** (1999) no. 2, 364–373.

[115] SNO+ Collaboration, M. Anderson et al., *Measurement of the* ^{8}B *solar neutrino flux in* SNO+ *with very low backgrounds*, Phys. Rev. D **99** (2019) no. 1, 012012.

[116] SNO+ Collaboration, A. Allega et al., *Improved search for invisible modes of nucleon decay in water with the* SNO + *detector*, Phys. Rev. D **105** (2022) no. 11, 112012.

[117] SNO+ Collaboration, M. R. Anderson et al., *Measurement of neutron-proton capture in the* SNO+ *water phase*, Phys. Rev. C **102** (2020) no. 1, 014002.

[118] SNO+ Collaboration, A. Allega et al., *Evidence of Antineutrinos from Distant Reactors Using Pure Water at* SNO+, Phys. Rev. Lett. **130** (2023) no. 9, 091801.

[119] SNO+ Collaboration, M. Anderson et al., *Optical calibration of the SNO+ detector in the water phase with deployed sources*, JINST **16** (2021) no. 10, P10021.

[120] I. Morton-Blake, *First Measurement of Reactor Antineutrinos in Scintillator at SNO+ and Study of Alternative Designs for Large-Scale Liquid Scintillator Detectors*. PhD thesis, University of Oxford, 2021.

[121] D. Auty et al., *A method to load tellurium in liquid scintillator for the study of neutrinoless double beta decay*, Nucl. Instrum. Meth. A **1051** (2023) 168204.

[122] S. Seibert et al., *RAT User's Guide*, https://rat.readthedocs.io/en/latest/index.html.

[123] T. Bolton, *The Braidwood Reactor Anitneutrino Experiment*, Nuclear Physics B - Proceedings Supplements **149** (2005) 166–169.

[124] R. Brun and F. Rademakers, *ROOT: An object oriented data analysis framework*, Nucl. Instrum. Meth. A **389** (1997) 81–86.

[125] S. Agostinelli et al., *Geant4—a simulation toolkit*, Nucl. Instrum. Meth. A **506** (2003) no. 3, 250–303.

[126] J. Allison et al., *Geant4 developments and applications*, IEEE Transactions on Nuclear Science **53** (2006) no. 1, 270–278.

[127] G. Horton-Smith, *An introduction to GLG4sim features*, Https://www.phys.ksu.edu/personal/gahs/glg4sim/glg4sim-intro-2006-05-19.pdf, 2006.

[128] J. Dunger and S. D. Biller, *Multi-site event discrimination in large liquid scintillation detectors*, Nucl. Instrum. Meth. A **943** (2019) 162420.

[129] T. Kaptanoglu, *Measurements of 0.5 g/L LAB+PPO*, SNO+ DocDB 5075, 2019.

[130] J. Dunger, *Topological and Time Based Event Classification for Neutrinoless Double Beta Decay in Liquid Scintillator*. PhD thesis, University of Oxford, 2018.

[131] H. A. Bethe, *Molière's Theory of Multiple Scattering*, Phys. Rev. **89** (1953) 1256–1266.

[132] *The RAT User's Manual - Data Cleaning*, SNO+ Internal Document.

[133] D. Gooding, M. Askins, C. Grant, A. Li, and T. Pershing, *Status of Data Cleaning for New SNO+ Water Data*, SNO+ DocDB 6593, September, 2020.

[134] Ana Sofia Carpinteiro Inácio, *Data Analysis of the Water and Scintillator Phases of SNO+: from Solar Neutrino Measurements to Double Beta Decay Sensitivity Studies*. PhD thesis, Universidade de Lisboa, 2022.

[135] S. S. Wilks, *The Large-Sample Distribution of the Likelihood Ratio for Testing Composite Hypotheses*, The Annals of Mathematical Statistics **9** (1938) no. 1, 60 – 62.

[136] G. M. Cordeiro, F. Cribari-Neto, E. C. Q. Aubin, and S. L. P. Ferrari, *Bartlett corrections for one-parameter exponential family models*, Journal of Statistical Computation and Simulation **53** (1995) no. 3-4, 211–231.

[137] *Large Photocathode Area Photomultiplier Tubes*, Https://www.hamamatsu.com/content/dam/hamamatsu-photonics/sites/documents/99_sales_library/etd/large_area_pmt_tpmh1376e.pdf.

[138] V. I. Tretyak and Y. G. Zdesenko, *Tables of Double Beta Decay Data – An Update*, Atomic Data and Nuclear Data Tables **80** (2002) no. 1, 83–116.

[139] T. Kroupová, *Neutrinoless Double Beta Decay and the SNO+ Experiment*, Presented at the conference on science at the sanford underground research facility (cossurf 2022), 2022.